Spring 2020

Frequency selective surface-based sensing: Theory and applications

Mahboobeh Mahmoodi

Department: Electrical and Computer Engineering

FREQUENCY SELECTIVE SURFACE-BASED SENSING: THEORY AND APPLICATIONS

by

MAHBOOBEH MAHMOODI

A DISSERTATION

Presented to the Graduate Faculty of the

MISSOURI UNIVERSITY OF SCIENCE AND TECHNOLOGY

In Partial Fulfillment of the Requirements for the Degree

DOCTOR OF PHILOSOPHY

in

ELECTRICAL ENGINEERING

2020

Approved by:

Kristen M. Donnell, Advisor
Jun Fan
Jie Huang
Victor Khilkevich
Edward Kinzel

PUBLICATION DISSERTATION OPTION

This dissertation consists of the following four articles, formatted in the style used by the Missouri University of Science and Technology:

Paper I, found on pages 10–46, to be submitted to *IEEE Transaction on Antenna and Propagation*.

Paper II, found on pages 47-59, has been published in the *IEEE Sensor Letters,* Vol. 1, No. 6, pp. 1-4, 2017.

Paper III, found on pages 60–85, has been submitted to *IEEE Transaction on Instrumentation and Measurement*.

Paper IV, found on pages 86–109, is under revision for resubmission to *IEEE Transaction on Instrumentation and Measurement*.

.

ABSTRACT

Frequency selective surfaces (FSS) are periodic arrays of resonant elements with a specific (resonant) reflection/transmission response when illuminated by electromagnetic energy. FSSs have been utilized for different applications such as spatial filters, reflectors, lenses, radomes, and more recently, as sensors. FSS-based sensors have shown potential for numerous applications in structural health monitoring such as crack detection, concurrent strain and temperature sensing, normal and shear strain sensing, inspection of layered structures, etc. As FSS-based sensing is largely undeveloped, there are many critical aspects that must be fully understood before this sensing approach can be fully utilized. Therefore, the goal of this research is to advance the science behind FSS-based sensing in order to create a platform of knowledge upon which future engineers may utilize when designing FSS-based sensors. To this end, the theoretical (assuming infinite dimensions and a uniform excitation) FSS response is modeled using a cavity-based coupled-mode theory and subsequent quality factor analysis for patch and loop unit cells in order to study the effect of unit cell dimension, element geometry and substrate properties on the FSS frequency response. In addition, the differences between theoretical and practical FSSs are studied in order to obtain design rules and metrics to achieve a reliable (localized) sensing measurement by an FSS sensor, thereby improving the sensing resolution (from the dimensions of the sensor to smaller “cells” within the sensor). Then, to achieve the maximum resolution of the FSS sensor, an approach is presented to determine the optimal sensor cell size. Additionally, a method using synthetic beamforming is presented to obtain an adaptive resolution for FSS sensing.

ACKNOWLEDGMENTS

I would like to thank my advisor, Dr. Kristen M. Donnell, for all her support during my PhD program, which was not possible for me without her. I also would like to thank my mentors and former colleagues, Dr. Reza Zoughi and Dr. Mohammad Tayeb Al-Qasser, who taught me a lot. Further, thanks to all my committee members, Dr. Jie Huang, Dr. Edward Kinzel, Dr. Victor Khilkevich, and Dr. Jun Fan.

I am also grateful to work with excellent colleagues in my former group of *Applied Microwave Nondestructive Lab* and current group of *Microwave Sensing Lab* for making me enthusiastic and motivated in this journey.

Last but not the least, I am thankful for having a great, lovely, and supportive family. Special thanks to my father, Shams-Ali Mahmoodi, and my mother, Tooba Abbasi.

TABLE OF CONTENTS

Page

LIST OF ILLUSTRATIONS

SECTION Page

PAPER II

PAPER III

PAPER IV

NOMENCLATURE

Symbol	Description
Q-factor	Quality factor
Q_{rad}	Radiation Quality factor
Q_d	Dielectric quality factor
Q_c	Conductor quality factor
Q_0	Parallel combination of dielectric and conductor quality factors
$Q_{rad,TE}$	Radiation quality factor for transverse electric mode
$Q_{rad,TM}$	Radiation quality factor for transverse magnetic mode
$P_{rad,TE}$	Radiated power into transverse electric excitation mode
$P_{rad,TM}$	Radiated power into transverse magnetic excitation mode
Γ	Reflection coefficient
$\Gamma_{co,TE}$	Co-coupled reflection coefficient for transverse electric mode
$\Gamma_{co,TM}$	Co-coupled reflection coefficient for transverse magnetic mode
Γ_{cross}	Cross-coupled reflection coefficient
W_S	Stored energy
$\mathcal{E}_r$	Permittivity
$\mathcal{E}_{r,eff}$	Effective permittivity
$tan\delta$	loss tangent
η_{sw}	Surface wave efficiency
f	Frequency
f_r	Resonant frequency

Δf_r	Frequency shift
η_{ill}	Illumination efficiency
η_s	Spill-over efficiency
η_{sc}	Sensor cell efficiency
θ_e	Half of the subtend angle of the illumination pattern
S_{11}	Reflection coefficient
$\|S_{11}\|$	Magnitude of the reflection coefficient
λ	Wavelength
λ_0	Wavelength at the resonant frequency
K	Wave number
K_x	Wave number in x direction
K_y	Wave number in y direction
K_z	Wave number in z direction
PSF	Point spread function

1. INTRODUCTION

1.1. FREQUENCY SELECTIVE SURFACES

Frequency selective surfaces (FSSs) are periodic arrays of conductive elements that cause a particular resonant reflection or transmission response when illuminated with high frequency electromagnetic energy. A few example elements are shown in Figure 1.1. The FSS frequency response is dependent upon element geometry, inter-element spacing, substrate properties (permittivity, loss tangent, and thickness) and the local environment [1]. FSSs have historically been used as high frequency filters [2]-[3], reflectors [1], lenses [4], radomes [5]-[6], and absorbers [7]-[10]. More recently, they have also found application as sensors [3-12], often for structural health monitoring (SHM) needs.

FSSs are uniquely well-suited as a wireless sensing solution due to their remote interrogation, as illustrated in Figure 1.2. As mentioned above and shown in Figure 1.1, FSSs can be designed to operate in reflection or transmission mode. However, from a practical point-of-view for sensing applications, FSS sensors designed in reflection mode are desirable, as they require a one-sided interrogation (as opposed to needing access to both sides of a structure for inspection). This is also beneficial from a signal detection point-of-view, since the structure under test does not interact with a signal reflected by the FSS but will affect (and may attenuate) that signal if it must travel through the structure prior to detection.

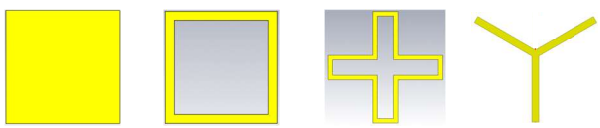

Figure 1.1. Example FSS elements.

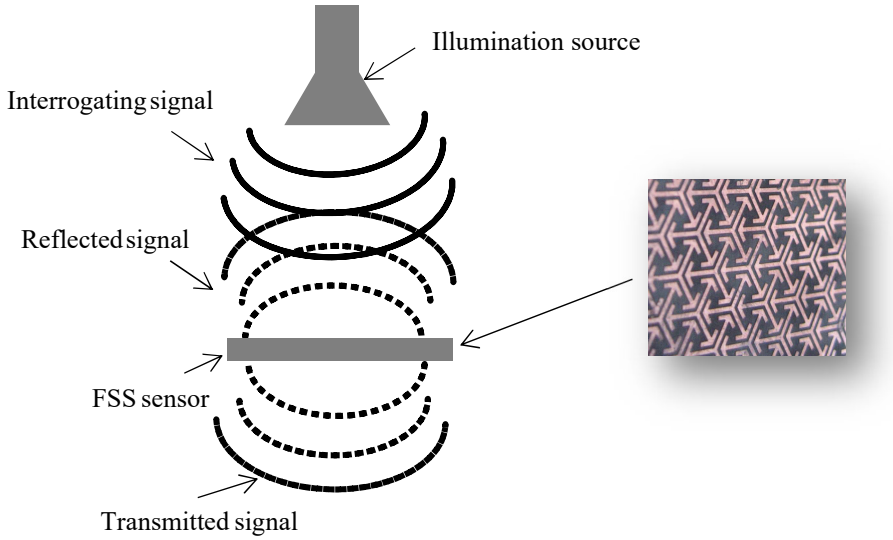

Figure 1.2. FSS sensor with an external illumination.

1.2. FSS-BASED SENSING APPLICATIONS

As a sensor, changes in the frequency response of an FSS are monitored and related to parameters such as strain, temperature, etc. Therefore, geometrical or physical changes may affect the frequency response of FSS in different ways including: 1) causing a shift in the resonant frequency of the FSS sensor; 2) varying the amplitude of the reflection/transmission coefficient at the resonance (i.e., affecting resonant depth); and 3) varying the quality factor (Q-factor) in terms of the width and depth of the frequency response at resonance [11].

Recent examples of FSS sensing include crack detection [12]-[13], strain sensing [11], [14]-[17], inspection of layered structures [18], material characterization [19], paper thickness and humidity detection [20], concurrent temperature and strain sensing [17], etc. More specifically, in [12], a cross dipole FSS is used for crack detection by monitoring the frequency shift of the transmission response the sensor. It is shown that when the crack occurs on the cross dipole in a direction perpendicular to the interrogating polarization, it

causes a frequency shift. However, when the crack direction is parallel to the interrogation polarization, the frequency response does not change. Another example of crack detection using frequency selective surface on a paper substrate is shown in [13] for the assessment of concrete structures.

FSS-based sensors have also been applied as strain sensors for normal and shear strain [14]. In this work, a loaded tripole-based FSS is used. Normal strain sensing is achieved using the reflection response of the FSS when the interrogating polarization is perpendicular to the direction of strain. In addition, it is shown that as the shear strain increases, the cross-polarization level (i.e., the polarization of the received and incident electric fields are perpendicular) increases. Another example of strain sensing is found in [15], which features a loop-based FSS and is embedded in a multi-layer bridge column.

FSS sensors can also be useful for inspection of changes in layered structures such as detection of disbond or delamination. For example, in [18] an FSS sensor is located behind the layer, which may be delaminated. Then, the effect of delamination thickness is studied as an additional air layer. It is shown that delamination changes the resonant frequency and depth of the FSS sensor response. Multiple sensing parameters can also be concurrently sensed via FSS sensing technology through proper sensor design and interrogation. For example, in [17], a dual band FSS sensor is presented using two cross loops that provide two distinct resonances in reflection mode. This sensor is capable of concurrent temperature and unidirectional strain measurement when the interrogating polarization is parallel to the strain direction.

FSS-based sensors have also found applications in terahertz (THz) regime. As an example, in [21] a symmetric split ring resonator is used for sensing small amounts of

chemical and biochemical materials. Specifically, the effect of a small film at the gap of the split ring element (making the split ring asymmetric) is studied and is shown to provide a high sensitivity to the presence of chemical materials. Another example of a THz FSS sensor is an integrated sensor using a THz FSS and an optical fiber [20]. Here, the FSS is interrogated by a THz subwavelength optical fiber for monitoring the optical properties of non-transparent films when the film is in contact with the sensor. Hence, this sensor is capable of monitoring multiple parameters such as paper thickness and humidity content.

As mentioned, FSS-based sensors have shown application as a wireless and passive sensor. However, adding active components such as diodes to the FSS can be advantageous. As such, in [16], an active FSS for strain sensing is introduced. This FSS sensor is a two-layer FSS (with two resonant frequencies) featuring cross dipoles (lower resonance) and loop elements (higher resonance). The loop elements are electrically connected by PIN diodes. The upper resonance is used for strain sensing and is modulated between a visible (detectable) and invisible (i.e. does not exist) state. This modulated capability has two practical ramifications: 1) the ability to clearly delineate the sensing resonant frequency from any other (static) resonant frequencies or noise; and 2) the ability to make differential measurements in order to remove other reflections that may be present in both states of the measured signal. In this way, any static reflections that are common to both states will be effectively removed from the sensing data. The lower resonance can be used for energy harvesting to power the active element.

Another similar area of study is metamaterial-based sensors. Metamaterials are synthetic composite materials that are similar to FSSs when used within an array of elements and externally illuminated. An example of metamaterial-based sensors is the

double split ring resonator-based metamaterial for strain sensing [22], and a multi-functional metamaterial sensor for sensing of moisture, density and temperature [23]. In addition, a metamaterial-based sensor for dual axis strain sensing in the terahertz regime is presented in [24].

1.3. RESEARCH OBJECTIVE

As explained, FSS-based sensors have shown the potential for sensing applications. Usually, FSSs are analyzed assuming an infinite number of unit cells and a uniform plane wave excitation. However, in practice, an FSS has a finite number of unit cells and is illuminated with a spatially varying electric field pattern from an antenna such as a horn [25]. In this case, there are three factors that affect the deviation of the finite FSS's response from the ideal (infinite array with plane wave excitation) case: 1) the non-uniform excitation, 2) the effect of edges (truncation from an infinite array), and 3) the number of FSS unit cells. Hence, it is very important to understand these factors as they relate to differences between the infinite FSS response and finite FSS response. Most of the literature that has been published (and discussed above [12]-[19]) uses the theoretical FSS response to show the FSS sensor performance. However, the practical FSS response will deviate from the theoretical FSS response with and without the presence of a change on the sensor. Another issue of using theoretical FSS analysis for sensing applications is that, often, a localized measurement is desired. For example, the presence of a crack will not occur on all FSS elements at the same time, as is assumed in [12]-[13] for crack detection. Another practical concern is the resolution of the sensor. FSSs are traditionally used as a large array of elements and illuminated in their entirety. However, this results in a low

sensing resolution (i.e., the dimensions of the sensor itself). Hence, in this work, the resolution of FSS-based sensors is studied based on a localized illumination pattern. In this way, a large FSS sensor can be considered as consisting of many sensor cells, which can be illuminated individually to distinguish smaller changes on the sensor and hence improve the resolution.

To address these challenges, this dissertation focuses on several aspects of FSS-based sensing. First, the theoretical FSS response is studied through reflection coefficient modeling of two unit cells (i.e. patch and loop-based elements) using a cavity-based coupled resonator approach and quality factor analysis. In this way, the effect of design parameters such as element dimensions, inter-element spacing and substrate properties (permittivity, loss tangent, and thickness) on the frequency response of the FSS are studied, including the effect of fringing fields. The analytical model of [26] is modified for the patch unit cell, while a new model for the rectangular loop unit cell is proposed. Both models are in good agreement with full wave simulation for a wide range of substrate properties. Second, to evaluate the frequency response of an FSS sensor, three performance metrics (resonant frequency, resonant depth and quality factor) are introduced for the patch- and loop-based unit cells. In this study, the effect of different substrate properties on the FSS response is quantified in order to achieve a desired sensor response by a proper selection of the substrate and element shape. Third, the concept of resolution for an FSS-based sensor, which is introduced in [27] and based on the footprint of the illumination pattern on the sensor, is improved by an optimization approach to determine the optimum resolution of FSS-based sensor for a given illumination pattern. This optimization approach is based on the aperture efficiency approach in reflect-array antennas [28], and is applied

to FSS-based sensing for the first time. It discusses how to determine an illumination footprint for localized sensing that is optimized for minimal non-uniformity (similar to theoretical FSS excitation) and spill-over energy (energy diverted outside of the sensor cell) in order to isolate the sensor cells' response from that of other cells. Finally, a synthetic beamforming approach based on synthetic aperture radar, introduced in [29], is extended in order to achieve a high and adaptable resolution for FSS sensors.

1.4. ORGANIZATION OF THE DISSERTATION

In this dissertation, the fundamentals of FSS-based sensing are studied in order to create a platform for FSS-based sensing development. This investigation is achieved through various simulations, measurements, modeling, and analyses, as is delineated below in 4 publications.

In Paper I, in order to find the reflection response of FSS unit cell with periodic boundary conditions and Floquet excitation analytically, the coupled resonator approach is used with a subseuenty quality factor analysis. This method is used to understand the effect of the element geometry, and substrate properties (permittivity, loss tangent, and thickness) on the response of infinite FSS with uniform illumination. To this end, the response of the infinite FSS is defined in terms of the radiation, conductor and dielectric quality-factors. The FSS element is modeled as a cavity resonator at the end of a waveguide transmission line and excited with Floquet modes. The effect of fringing fields and the frequency dependent behavior of the effective permittivity of the substrate are considered to improve the accuracy of the frequency response. A rectangular loop and patch unit cell are considered for this study. The fringing fields effect for the loop unit cell is more

complicated than that of the patch due to three factors. The first is the existence of the electric field null in the middle of the loop. The other two factors are the ratio of the inter-element spacing to substrate thickness and the ratio of the loop length to the substrate thickness, as both are related to fringing field outside or inside the loop, respectively. The effect of these factors is discussed on the resonant frequency of the loop. Then, to develop a model for the radiation Q-factor of the loop with fringing fields effect, the loop is designed for when the coupling inside and outside of the loop is minimal. Finally, the reflection coefficient of the unit cells is calculated using the Q-factors, which are in good agreement with the full-wave simulation results for a wide range of substrate properties.

In Paper II, three performance metrics (resonant frequency, resonant depth, and quality factor) are proposed to quantify the effect of substrate properties on the sensor performance. These metrics are applied to a patch- and loop-based FSS sensor. The results show that the patch-based sensor has improved performance when designed using a thinner and higher loss substrate, while the loop-based sensor has better performance when a substrate with less loss but increased thickness is used. Additionally, measurements are also provided for sensors utilizing the low loss substrate. Lastly, the performance of the two sensors is shown for strain sensing. The results indicate that the resonant frequency shift (when under mechanical loading) of both sensors is largely independent of the substrate permittivity.

In Paper III, the resolution of FSS-based sensors is discussed. When an FSS sensor is illuminated in full, the response of the sensor is related to the entire FSS landscape. In this way, the resolution of the sensor is equal to the FSS dimensions. However, this limits the localized sensing. As such, to improve the achievable resolution, the sensor must be

illuminated locally in order for the response to be related to a specific region of the sensor. Under this approach, an FSS sensor is considered to consist of many sensor cells. Therefore, to quantify the sensor cell efficiency in terms of the illuminating footprint in order to obtain the optimum sensor cell size, an analysis approach based on reflectarray aperture efficiency is used. As such, by maximizing the sensor cell efficiency, an optimum sensor cell size can be determined for a given illuminating footprint. This approach is applied to a grounded square loop-based FSS sensor, with simulation and measurement results provided. The results indicate that optimal sensor cell dimensions can be determined where the total efficiency of a given footprint is maximized. To support this, three different sensor cells are considered with the same maximum total efficiency, of which the smallest sensor cell gives the highest resolution of ~3 cm × 3 cm.

In Paper IV, the application of synthetic beamforming is used to achieve an adaptable resolution for localized sensing using FSS sensor. To this end, this approach is proposed to generate an arbitrary beam shape with a desired footprint. Moreover, the illumination and spill-over efficiencies of the synthetic beam are defined, simulated, and discussed. The results show that a minimum focal area of $1\lambda_0 \times 1\lambda_0$ (3×3 unit cells for the FSS sensors considered here) is essential to achieve a spill-over efficiency of greater than 80%, thereby reducing the contribution of other neighboring unit cells on the sensor response. In addition, the illumination efficiency when a synthetic beam is utilized for illumination is greater than 80% due to the uniformity of the synthetic beam. Representative measurements were also performed on a sensor with a simulated strain profile.

PAPER

I. PATCH- AND LOOP-BASED FREQUENCY SELECTIVE SURFACE MODEL BASED ON THE QUALITY FACTOR APPROACH

ABSTRACT

Frequency selective surfaces (FSSs) are periodic arrays of conductive elements illuminated with electromagnetic excitation. Theoretically, FSSs are analyzed using a unit cell with periodic boundaries and uniform illumination. Another analysis approach is based on a coupled-mode theory with Floquet excitation. To this end, the reflection response of a conductor-backed rectangular patch and loop-based FSSs is defined in terms of radiation, conductor and dielectric quality factors. Within this approach, the effect of fringing fields and the frequency-dependent behavior of the effective permittivity of the substrate is included. Specifically, the fringing field of the loop unit cell is discussed in the context of three factors: 1) the ratio of inter-element spacing to substrate thickness, 2) the ratio of loop length to substrate thickness, and 3) excitation mode of the loop (here, TM_{010} mode). In addition, the effect of fringing fields on the resonant frequency of the FSS is captured through and effective perimeter for the loop (and effective length for the patch). Then, a model for the radiation Q-factor of the loop is developed that includes the effect of fringing fields. The model does not include the effect of mutual coupling between adjacent elements or between two arms of the loop. The model for the radiation Q-factor is modified from the literature by including the effect of fringing. Finally, the reflection coefficient of both

unit cells are calculated using the Q-factor model. The results are in good agreement with full-wave simulation results for a wide range of substrate properties.

1. INTRODUCTION

Frequency selective surfaces (FSSs) are a planar array of conductive elements that can provide a reflection or transmission response when illuminated by an external electromagnetic source [1]. The frequency response of FSS is primarily affected by the element shape, substrate properties (permittivity, $\mathcal{E}_r$, loss tangent, $tan\delta$, and thickness, h), and inter-element (edge to edge) spacing (S). FSS have been utilized in many applications such as reflectors [1], lenses [2], spatial filters [3]-[4], radomes [5]-[6], absorbers [7]-[10], and recently as a wireless sensor [11]-[13]. Also, FSSs are low profile and suitable for many applications by providing wireless interrogation in addition to ease of fabrication and implementation. On a larger scale, the popularity of FSSs for different applications is due to the fact that, by using different element geometries and substrates, the frequency response of FSS can be quite diverse and hence tailored to many different applications.

FSSs are typically analyzed as a unit cell (i.e., the element with a specific periodicity on a substrate) with periodic boundaries and uniform illumination. In this way, the structure mimics an infinite array of elements. One such way to accomplish modeling of an infinite FSS is through Floquet theory [1], [14]-[15]. Among different methods, Floquet theory better approximates the infinite FSS response since it accounts for the effect of incident angle [14]-[15]. In [15], an analysis approach is introduced for reflectarray unit cell design using a coupled-mode theory including the Floquet modes of excitation to find

the reflection coefficient (Γ) of a unit cell backed by a conducting plane with periodic boundary analytically (in order to remove dependence on full wave simulation). This Γ is defined in terms of the quality factors for the element radiation, substrate and conductor. In the current paper, the Q-factor analysis based on the coupled-mode theory of [15] is applied to a rectangular patch and rectangular loop unit cells with a conductor-backed substrate in order to better understand the effect of design parameters such as element geometry, unit cell dimension, and substrate properties on the reflection coefficient of the infinite FSS. Hence, Γ of both (infinite) FSS designs with a uniform planewave excitation is analytically calculated. Also, to extend the model from [15], the model includes the effect of fringing fields and surface waves.

2. BACKGROUND

In order to find the reflection coefficient (Γ) of a unit cell (FSS/reflectarray element) with a conductor backed substrate, the coupled-resonator approach can be used along with the Q-factor analysis [15]. This method is applied to a rectangular patch and a rectangular loop unit cell, with both illustrated in Figure 1. The patch and loop unit cells are modeled inside a waveguide with dimensions of $a \times b$, which have the same length of W and L, respectively (see Figure 1), along the x- and y-directions, on the same substrate with a thickness of h. In addition, the width of the loop element is equal to t_w and t_l along x and y directions, respectively. The structure made up of the element, substrate, and conductor-backing can be modeled as a cavity resonator which is (as part of the FSS unit cell) subsequently considered as the load to a waveguide transmission line with a Floquet mode

excitation [15]. The two fundamental orthogonal Floquet modes, TE_{00} and TM_{00}, are considered to propagate inside the waveguide transmission line (polarization indicated in Figure 1). The incident propagating mode inside the waveguide can be coupled to the resonator radiating mode of TM_{010}. The E-field and magnetic current of the patch and loop resonator models for the TM_{010} mode are shown in Figure 2 (neglecting fringing). The E-field on edges of the patch and the exterior edges of the loop are shown in red, while the E-field on the interior edges of the loop are shown in green. Also, the magnetic current direction on the long edges is shown in black. As shown, the E-field at $y = \pm L/2$ (long edge of the cavity) is constant for both elements. However, the E-field along the short edges of the cavity (modeled below in (7) as a sinusoidal distribution), along the y-direction, is a function of y with a minimum of zero at $y = 0$. In other words, the E-field at the short edges (i.e., at $x = \pm W/2$) of the cavity is variable.

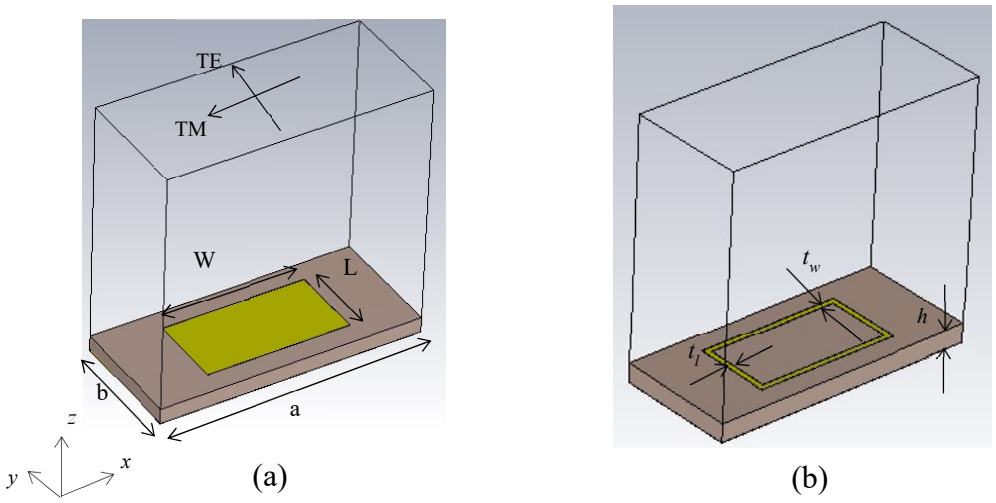

Figure 1. The unit cell load of a rectangular waveguide transmission line with Floquet excitation for (a) patch, and (b) loop unit cells.

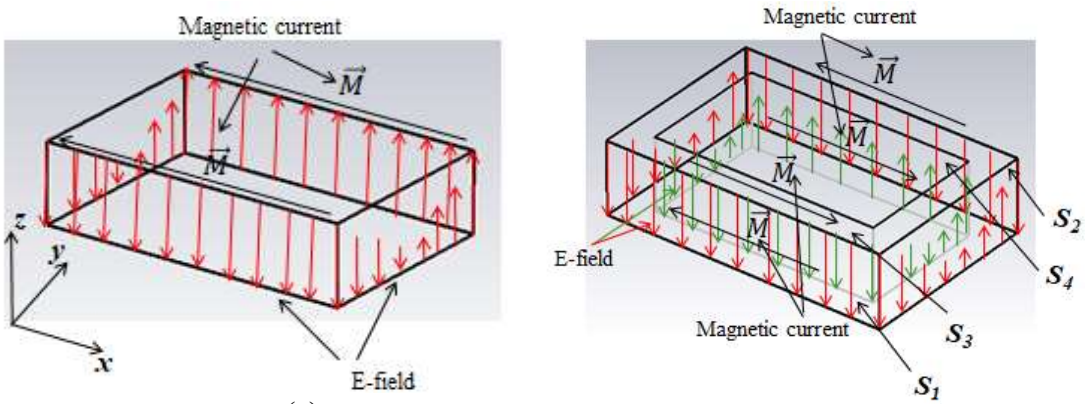

Figure 2. The electric field and magnetic current of the element using the cavity model with TM_{010} mode for the (a) patch, and (b) loop elements.

The power reflected from the element is reflected in co- and cross-polarized portions [15]. Specifically, there are three different reflections defined as follows [15]:

$$\Gamma_{TE,co}(f)=\frac{\frac{1}{Q_{rad,TE}}-\left(\frac{1}{Q_{rad,TM}}+\frac{1}{Q_0}\right)-\frac{2j(f-f_r)}{f_r}}{\frac{1}{Q_{rad,TE}}+\frac{1}{Q_{rad,TM}}+\frac{1}{Q_0}+\frac{2j(f-f_r)}{f_r}} \tag{1}$$

$$\Gamma_{TM,co}(f)=\frac{\frac{1}{Q_{rad,TM}}-\left(\frac{1}{Q_{rad,TE}}+\frac{1}{Q_0}\right)-\frac{2j(f-f_r)}{f_r}}{\frac{1}{Q_{rad,TM}}+\frac{1}{Q_{rad,TE}}+\frac{1}{Q_0}+\frac{2j(f-f_r)}{f_r}} \tag{2}$$

and

$$\Gamma_{cross}(f)=\frac{\frac{2}{\sqrt{Q_{rad,TE}Q_{rad,TM}}}}{\frac{1}{Q_{rad,TM}}+\frac{1}{Q_{rad,TE}}+\frac{1}{Q_0}+\frac{2j(f-f_r)}{f_r}} \tag{3}$$

where $Q_{rad,TE}$ and $Q_{rad,TM}$ are the radiation Q-factors for TE and TM modes, respectively, f is the operating frequency, f_r is the resonant frequency of the cavity resonator, and Q_0 is the parallel combination of conductor loss, $Q_c = h\sqrt{\pi f \mu \sigma}$ and dielectric loss, $Q_d = 1/\tan\delta$ as is shown in (4).

$$Q_0 = \frac{Q_c Q_d}{Q_c + Q_d} \tag{4}$$

Here, h is the substrate thickness, and μ and σ are the permeability and conductivity of the conductor, respectively. Additionally, Q_{rad} is in general formulated as:

$$Q_{rad} = 2\pi f_r \frac{W_S}{P_{rad}} \tag{5}$$

where W_s and P_{rad} are the stored energy within the cavity resonator and the power radiated from the resonator into the excited mode in the waveguide, respectively. To calculate Q_{rad} (5) depends on the element geometry, h, unit cell dimensions (i.e. waveguide dimensions), and incident angle, there are two steps. First, using the cavity model with an excitation mode of TM_{010} shown in Figure 2, the energy stored between the element and conductive plane can be found [15], [16]. Second, P_{rad} is excited by the volume magnetic current density on the long edge of the resonator (see Figure 2) and can be determined in terms of the excitation wave impedance and the reflected wave amplitude inside of the waveguide [18], [20]. Moreover, the Floquet excitation wave impedances are different for TE and TM modes [15], [17] (specific equations defined below). Hence, by knowing the $Q_{rad,TE}$ and $Q_{rad,TM}$ in addition to Q_0, the Γ of unit cell can be found. As such, the unit cell with different relative values of $Q_{rad,TE}$ and $Q_{rad,TM}||Q_0$, (for TE mode) operates in different coupling conditions [13], [15] when 1) $Q_{rad,TE} = Q_{rad,TM}||Q_0$, the resonator is critically coupled to the incident wave which means there is no reflection at f_r (which is proper for FSS application

[13]); 2) $Q_{rad,TE} < Q_{rad,TM}||Q_0$ and the resonator is over-coupled to the incident wave and will reflect the incident wave back with a large phase swing of Γ (proper for reflectarray antenna application [15]); and 3) $Q_{rad,TE} > Q_{rad,TM}||Q_0$, the resonator is under-coupled and a majority of the energy is stored inside the resonator and very little signal is reflected.

In [15], an analytical model for Q_{rad} of a rectangular patch unit cell is presented using the Q-factor approach with Floquet excitation. However, this work ignores the effect of fringing fields and the analytical results are presented for a thin and high permittivity substrate and a given resonant frequency. Hence, in [18], to achieve a more accurate model, the effect of fringing fields and effective permittivity ($\varepsilon_{r,eff}$) are considered for a square patch and a circular loop unit cell when the unit cell is considered inside the waveguide with TE_{10} excitation mode. However, the effect of fringing fields was assumed to be uniform for a loop-based unit cell, which is shown below to not be the case. Therefore, in this work, the complex Γ is modeled using the Q-factor approach with Floquet mode excitation (similar to [15]) for rectangular patch and loop unit cells including the effect of fringing fields and effective permittivity for a wide range of substrate properties ($tan\delta$, h, and ε_r). Specifically, the model for the rectangular patch unit cell is used from [15] and modified with including the fringing fields effect and calculating the resonant frequency based on the dimension of the patch element (similar to [18]). Moreover, the resonant frequency of the loop unit cell is studied in terms of $\varepsilon_{r,eff}$ and the effective perimeter of the loop by considering fringing fields. Using this definition of the resonant frequency, a more accurate definition of Q_{rad} and hence $\Gamma(f)$ are presented for the rectangular loop unit cell. The models for both patch and loop elements show good agreement between the analytical and full-wave results.

3. EFFECT OF FRINGING FIELDS ON RESONANT FREQUENCY

To begin, the resonant frequency of the patch (f_{rp}) and loop (f_{rl}) unit cells was calculated using two approaches. The first utilizes full wave simulation via CST© Microwave Studio, where the unit cells of Figure 1 were simulated with periodic boundary conditions and a Floquet excitation. The elements had dimensions of a = 22.86 mm, b = 10.16 mm, W = 12.5 mm, L = 6.5 mm (same for both patch and loop) and t_l = 0.5 mm and t_w = 0.5 mm for the loop. The unit cells are considered on a substrate with varying h from 5 mils to 140 mils, and ε_r of 2, 4.3 and 8, all with $tan\delta$ = 0.023. In addition, an analytical (closed form solution) approach based on the effective permittivity ($\varepsilon_{r,eff}$) and effect of fringing fields was also developed, with the results from this model compared to those from full wave simulation.

In the Q-factor approach presented in [15] and here, the unit cell is a microstrip-based element on a conductor-backed substrate. As is known for microstrip elements, $\varepsilon_{r,eff}$ of the substrate is dependent upon the ε_r and h of the substrate, and the ratio of the microstrip line width to h. In addition, dispersion also plays a role as the operating frequency increases. Therefore, the frequency dependent model for $\varepsilon_{r,eff}$ is used as part of the closed form solution of resonant frequency [19]:

$$\varepsilon_{r,eff}(f) = \varepsilon_r - \frac{\varepsilon_r - \varepsilon_{r,eff}(f=0)}{1 + \frac{\varepsilon_{r,eff}(f=0)}{\varepsilon_r}\left(\frac{f}{f_t}\right)^2} \tag{6}$$

where $\varepsilon_{r,eff}(f = 0)$ is the effective permittivity at low frequencies approaching f = 0, and

$f_t = Z_C(f=0)/2\mu_0 h$, where Z_C is the characteristic impedance of the microstrip transmission line.

As mentioned, an element on a substrate backed by a conducting plane can be modeled as a resonator cavity. In this way and for the patch and loop elements considered here, the E-field between the element and conducting plane (neglecting fringing fields) with a TM_{010} mode excitation (as shown in Figure 2) is polarized in the *z*-direction as follows:

$$\vec{E} = E_0 \sin\left(\frac{\pi y}{L}\right)\hat{z} \tag{7}$$

where E_0 is the amplitude of the E-field and L is the length of the patch/loop in the *y*-direction (see Figure 1). However, as mentioned above, this model does not include the effect of fringing fields [16]. Such an approximation is more accurate for thin substrates where the fringing fields are negligible. However, generally speaking, fringing fields may have a noticeable effect on FSS performance. As such, the effect of fringing fields specifically on the resonant frequency of the FSS will be captured through adjusted (or effective) physical dimension(s) of the element.

3.1. RESONANT FREQUENCY OF THE PATCH UNIT CELL

To illustrate the effect of fringing fields on the resonant frequency of the patch element, the magnitude of the E-field and surface current on the surface of the patch element on the substrate with $\mathcal{E}_r$ of 4.3 and h of 30 mils were simulated in CST and are shown in Figure 3. As seen (Figure 3a), the fringing field distribution at the long edges of the patch is mostly uniform. However, the fringing field distribution is variable at the short

edges of the patch (as a result of the variable E-field of (7)). In addition, the surface current of the patch is shown in Figure 3b, which has a maximum value at $y = 0$ and minimum at the long edges. This surface current variability in the y-direction illustrates that this dimension (L) dictates the resonant frequency. Hence, the length extension (addition to L) due to the fringing field at the long edges is important. Therefore, the length extension (δl, as shown in Figure 3) on each side of the patch along its length (L) affects the resonant frequency of the patch (f_{rp}). Hence, the effective length of the patch, $L_{p,eff,}$ is given as $L_{p,eff} = L + 2\delta l$, and is subsequently used to determine f_{rp} as follows [16]:

$$f_{rp} = \frac{c}{2L_{p,eff}\sqrt{\varepsilon_{r,eff}}} \tag{8}$$

where c is the speed of light.

The f_{rp} from CST and (8) of the patch unit cell is shown in Figure 4a, and as seen, it reduces as h increases. The increase in h will slightly reduce the average of $\mathcal{E}_{r,eff}$ over the frequency band, as shown in Figure 4b. However $L_{p,eff}$, shown in Figure 4c relative to the original length (L) increases as h increases. Therefore, since the rate of increase of $L_{p,eff}$ is greater than the rate of decrease of the square root of $\mathcal{E}_{r,eff,}$ the increase in h results in an overall reduction of f_{rp}. Also, as seen in Figure 4a, the increase in $\mathcal{E}_r$ of substrate reduces f_{rp}, which is (indirectly, through (6)) evident in (8). In addition, $L_{p,eff}$ for high $\mathcal{E}_r$ is slightly less than that with for a low $\mathcal{E}_r$ because the electric field beneath the element is more confined for higher values of $\mathcal{E}_r$.

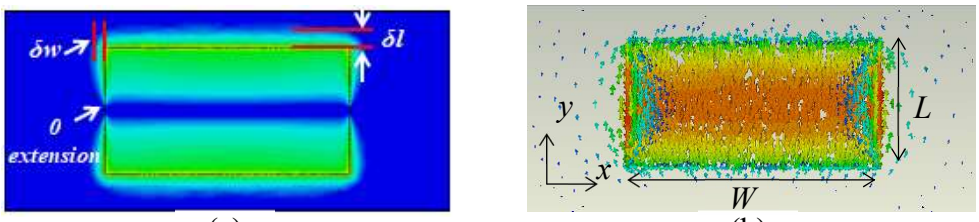

(a) (b)

Figure 3. 2D representation of (a) the electric field magnitude, and (b) the surface current of the patch.

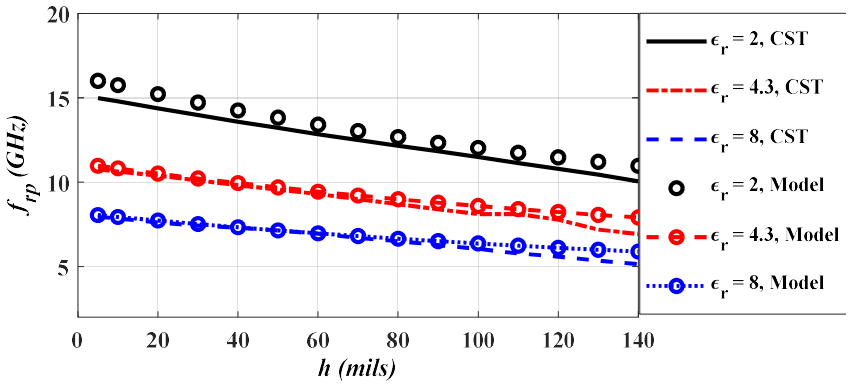

(a)

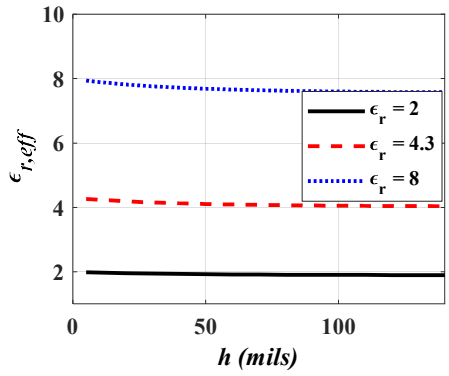

(b)

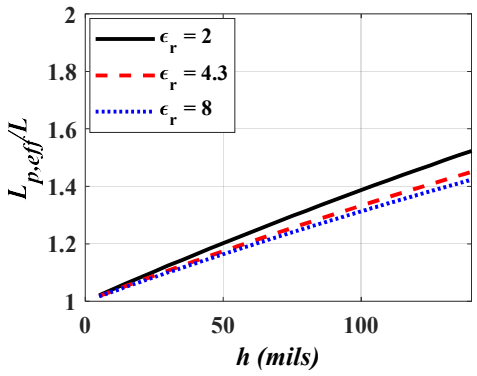

(c)

Figure 4. Comparison of simulated and analytical (a) resonant frequency, (b) $\mathcal{E}_{r,eff}$, and (c) $L_{p,eff}$ on different substrates of the patch unit cell.

3.2. RESONANT FREQUENCY OF THE LOOP UNIT CELL

The same approach (full wave simulation and closed form model) was applied to the loop element. In order to compare the results of the loop unit cell with the patch, the unit cell in Figure 1b is considered with the aforementioned dimensions and is referred to herein as loop unit cell #1. Later, as part of the discussion on the fringing fields effect on the resonant frequency of the loop unit cell, two more unit cells are studied.

In the case of the loop unit cell, the fringing fields on the exterior long and short edges of the loop are similar to the patch element, as shown in Figure 5a. However, the loop element has fringing fields on the interior edges as well. In addition, the surface current of the loop, shown in Figure 5b, follows the perimeter of the loop, with the minimum value at $x = 0$. The total electrical length of the loop is proportional to the perimeter of the loop [18], [21]. For a circular loop, this is true when the radius of the loop is much smaller than h [21]. Hence, generally the resonant frequency of the loop (f_{rl}) is related to its perimeter. However, since the effect of fringing fields is different on the inner and outer perimeters, the modified effective perimeter, $P_{l,eff}$, is defined in terms of the average of the physical perimeter, $P_0 = 2(L+W-t_l-t_w)$, in addition to the effect on the perimeter due to fringing fields.

With regards to the effect of fringing fields, it can be seen from Figure 5a that the fringing fields are almost uniform along the long edges of the element. However, since the E-field varies in terms of y (7) with the maximum at the exterior long edges ($y = \pm L/2$), the width extension of t_w at the exterior long edges is defined as δt_w, where δt_w is shown in Figure 6 and calculated using [16]. The width extension for the interior long edges is defined as δt_w multiplied by the coefficient of $\sin(\pi(L/2-t_W)/L)$ since the E-field at

$y = \pm L/2 \mp t_w$ is reduced in comparison with the exterior long edges (Figure 5a). On the other hand, the width extension for t_l along the short edges is variable since the E-field is a function of y. As seen, the width extension approaches to zero when y approaches zero, since E-field gets zero. Therefore, the width extension, δt_l is modeled as $\delta t_l \sin(\pi y / L)$ on both the exterior and interior short edges, because the E-field has sinusoidal behavior in this direction. Also, the fringing at the exterior corners, common between the two orthogonal edges, are modeled as a right triangle with base and height of δt_w, and δt_l, respectively.

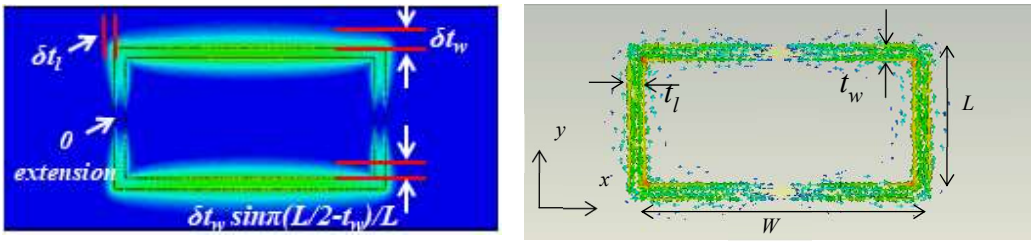

(a) (b)

Figure 5. 2D representation of (a) the electric field magnitude, and (b) surface current of loop unit cell #1.

It should be mentioned that to calculate δt_w (which is the width extension of the arm with the width of t_w), the ratio of t_l to h is used in the equation from [16], similar to the patch. This is because the fringing fields along the x-direction follow the width extension that occurs at the ends of the microstrip line with width of t_l. Then, since the E-field at the exterior long edge is constant, the fringing fields along the arm with a width of t_w (the long arm) follows the fringing at the ends of the exterior long edges. Therefore, the width

extension along the long edge is considered uniform and equal to δt_w, Similarly, δt_l is calculated in terms of t_w/h in the equation from [16].

To estimate the average perimeter of the loop, the length of the sinusoidal paths of the perimeter is calculated via a line integral along these curved sections and is given in the Appendix. Then, the average perimeter of the loop element due to the fringing fields is calculated but without the nulls located at $y = 0$. Also, in order to capture the effect of nulls in addition to mutual coupling due to the adjacent elements, a final modification to $P_{l,fringe}$ is done to determine the overall effective perimeter of the loop, $P_{l,eff}$. In fact, the presence of the nulls effectively removes a small section of the short edges of the loop. However, the mutual coupling between adjacent elements can increase as h increases by reducing the b/h ratio (same for S/h) [10] which leads to an increase in the effective exterior perimeter. Therefore, $P_{l,eff}$ was determined by simulating (in CST) the resonant frequency, calculating the effective permittivity (using (6)), and using

$$P_{l,eff} = \frac{c}{f_{rl}\sqrt{\varepsilon_{r,eff}}} \tag{9}$$

In order to use (9) to determine $P_{l,eff}$, $\varepsilon_{r,eff}$ is necessary. To determine this parameter, (6) was used. In addition, for the range of ε_r and h considered here, $t_{w,eff}(f = 0)/h > 1$ and therefore the approximation for $\varepsilon_{r,eff}(0)$ of [22] is used. To this end, $\varepsilon_{r,eff}$ is shown in Figure 7 for t_w = 0.5 mm (low frequency and high frequency averaged over the band values). Specifically, in Figure 7a, it is shown that $\varepsilon_{r,eff}(0)$ reduces as h increases. However, as seen in Figure 7b, the average of $\varepsilon_{r,eff}$ over the frequency band exponentially decreases for small values of h. For larger values of h, the behavior of $\varepsilon_{r,eff}$ linearly increases with h.

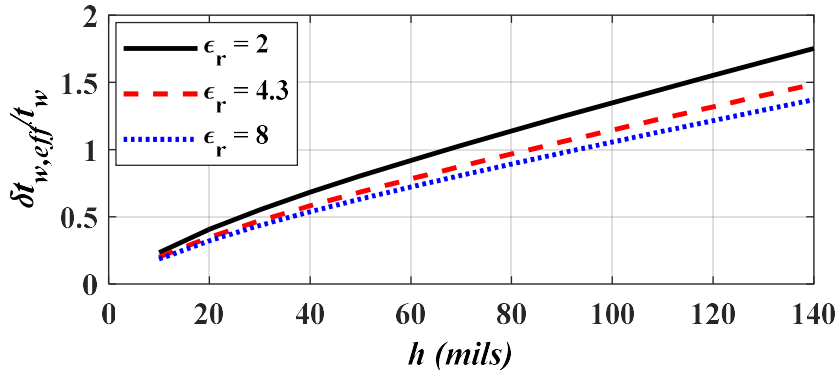

Figure 6. $\delta t_w/t_w$ vs. h for different $\mathcal{E}_r$.

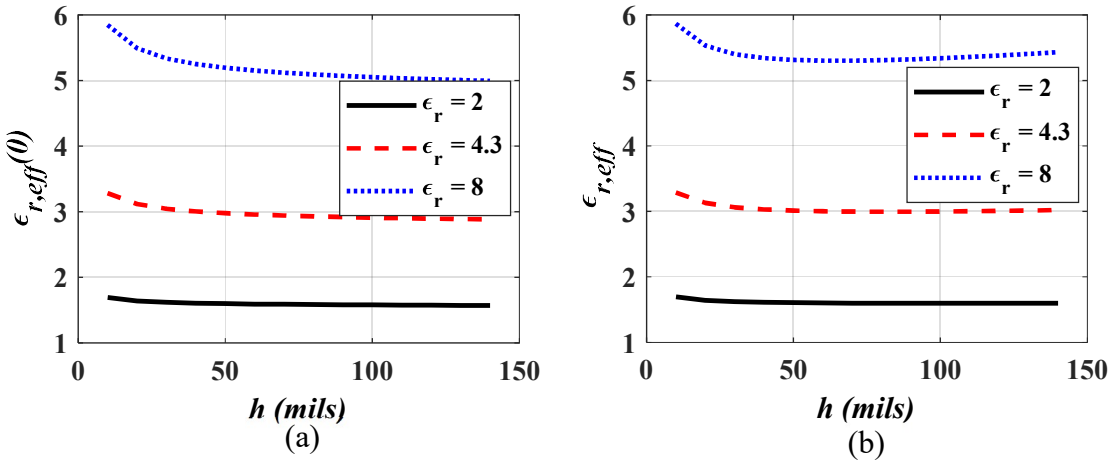

Figure 7. (a) $\mathcal{E}_{r,eff}$ from for a range of substrate heights, h, at (a) lower frequencies and (b) higher frequencies.

Next, f_{rl} was simulated in CST, as shown in Figure 8, along with the calculated f_{rl} from (9) for loop unit cell #1, and using $\mathcal{E}_{r,eff}$ results from Figure 7 and calculated $P_{l,fringe}$. As can be seen, there are minor differences between the simulated and analytical model results. These differences are attributed to the fact that the presence of the nulls is not taken into account, in addition to the S/h ratio as it relates to the mutual coupling between adjacent elements in the FSS (as the model does not include such effects). Moreover, in all

cases, f_{rl} increases for small values of h, with the most substantial increase occurring for $\mathcal{E}_r$ = 2. This is a result of the behavior of $\mathcal{E}_{r,eff}$ and (9), where larger changes in $\mathcal{E}_{r,eff}$ have a less substantial effect on f_{rl} and vice versa. For larger values of h, f_{rl} remains essentially constant with a slight decrease as h increases (consistent with the trends of Figure 7c).

Once $\mathcal{E}_{r,eff}$ and f_{rl} are known, $P_{l,eff}$ can be determined from (9), as is shown in Figure 9. Also, $P_{l,fringe}$ from above is included for comparison. In all cases and to faciliate comparison, the values have been normalized with respect to the original perimeter, P_0. As seen, $P_{l,fringe}$ is slightly less than P_0 (maximum of 1% difference). As h increases, $P_{l,fringe}$ decreases, and then for thicker substrates, slightly increases which is due to an increase in fringing fields which leads to an increase in $P_{l,fringe}$. In fact, since the rate of increase in the exterior perimeter and rate of reduction of the interior perimeter are very similar, $P_{l,fringe}$ is similar to P_0. However, $P_{l,eff}$ shows more variation in comparison with P_0 than $P_{l,fringe}$ as a function of h. More specifically, $P_{l,eff}$ reduces as h increases due to the nulls, and then increases as h increases due to the reduction in S/h which increases the electric field coupling between elements (and reduces the electric field located between the element and conductive ground plane (as is discussed in detail next).

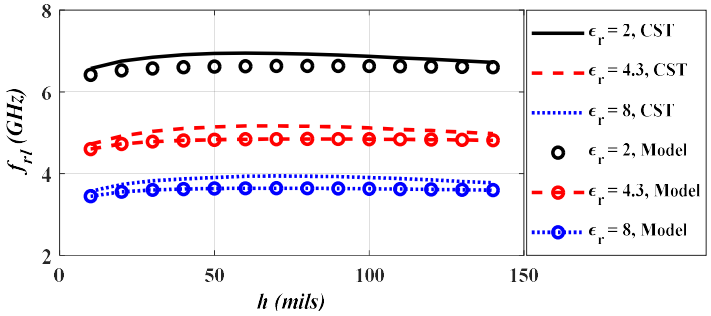

Figure 8. Resonant frequency of the loop for different $\mathcal{E}_r$.

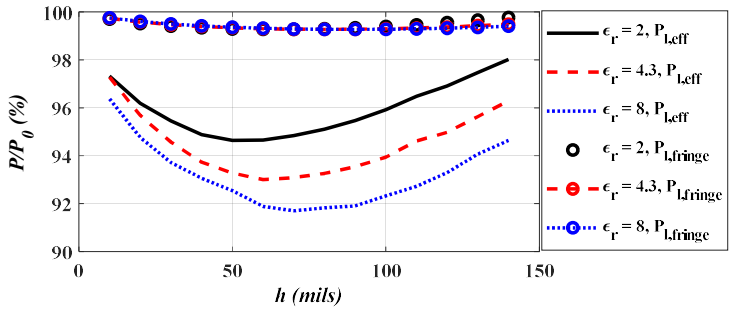

Figure 9. Comparison of $P_{l,fringe}$ and $P_{l,eff}$ vs. h for different $\mathcal{E}_r$.

To better understand the behavior of $P_{l,eff}$, the E-field of the loop unit cell is studied, as shown in Figure 10 and Figure 11. The reduction in $P_{l,eff}$ for increasing h is related to the width of the null in the electric field. That is to say, as h increases, the width of the null increases and the effective perimeter decreases, as is shown in Figure 10a-c. A side view of the element is shown in Figure 10d-f in the y-z plane at $x_1 = -(L-t_l)/2$ (location of nulls), where the null width is also evident. However, while in Figure 10c/f (h = 140 mils), the width of the null is greater than that of Figure 10b/e (h = 70 mils), $P_{l,eff}$ for h = 140 mils is larger than that of h = 70 mils. To illustrate the reason for this behavior, the E-field at x = 0 and the y-z plane (location of maximum E-field) is shown in Figure 11. As seen, for small h (i.e. 10 mils, Figure 11a), the concentration of the E-field is primarily located between the conductive loop and the conducting plane on the back of the substrate. However, as h increases, the E-field located between the conductive loop and ground plane reduces, and instead is primarily located around the conductive loop and coupled with the adjacent conductor loop (Figure 11b-c). In fact, in addition to h, the inter-element spacing (S) on the FSS affects the resonant frequency of the loop unit cell (here, the unit cell with the periodic boundary conditions represents an infinite array of loop elements). This is why the modeling of the loop shows small changes in $P_{l,fringe}$ with increasing h due to the effect of

fringing fields only (i.e., the effect of mutual coupling and nulls are not included). It should be noted that the scaling used in Figure 10 is used also valid for Figure 11-Figure 13.

As it relates to the mutual coupling effect, in [10], it is shown that when the ratio of substrate thickness to the periodicity of the unit cell (i.e., h/b) is less than 0.3, the capacitance between the element and conductor backing substrate exponentially decreases with increasing h. Meaning, for a thicker h, which is a factor of 0.3 greater than the periodicity, the mutual coupling is dominant in comparison with the field stored beneath the element. The aforementioned loop unit cell reaches $h/b > 0.3$ for $h > 120$ mils.

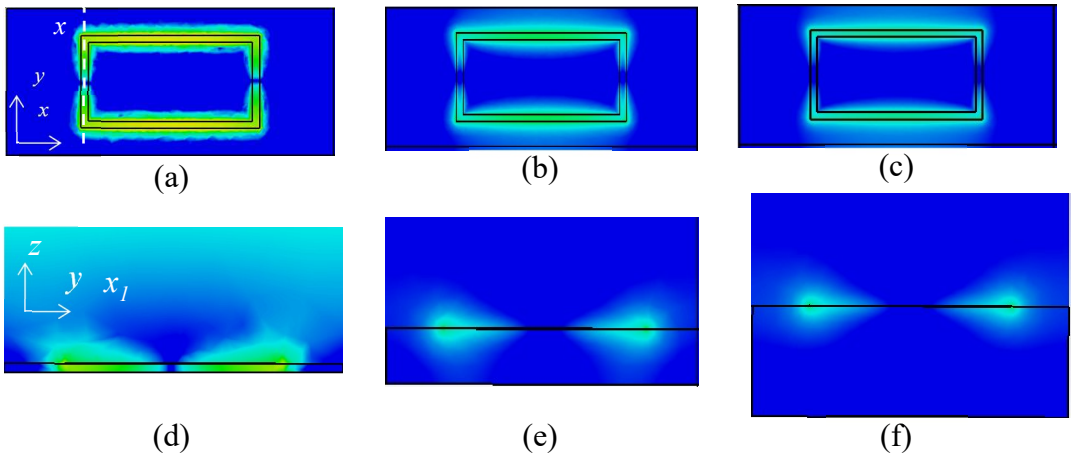

Figure 10. The E-field magnitude on the loop unit cell for $\mathcal{E}_r = 4.3$ and h equal to (a) 10 mils, (b) 70 mils, and (c) 140 mils, and the E-field magnitude in the y-z plane at $x = L/2$-$t_l/2$ (location of nulls) for h equal to (d) 10 mils, (e) 70 mils, and (f) 140 mils.

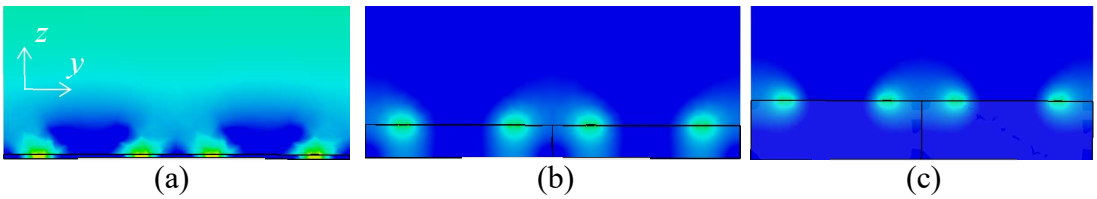

Figure 11. The E-field magnitude in the y-z plane at $x = 0$ (location of maximum E-field) for $\mathcal{E}_r$=4.3 and h equal to (a) 10 mils, (b) 70 mils, and (c) 140 mils.

Regarding to the effect of $\mathcal{E}_r$ on $P_{l,eff}$ from Figure 9, it is evident that as $\mathcal{E}_r$ increases, $P_{l,eff}$ decreases. This is due to the increased confinement of the E-field as $\mathcal{E}_r$ increases. Hence, the mutual coupling effect will be reduced by increasing $\mathcal{E}_r$ which results in more confinement in the E-field, as shown in Figure 12a-c for $\mathcal{E}_r$ of 2, 4.3 and 8, respectively. Also, the E-field around the nulls is more confined which causes a longer null and consequently a smaller $P_{l,eff}$. The elongation of the null with increasing $\mathcal{E}_r$ is evident in Figure 12d-f. Additionally, since the E-field is more confined for higher $\mathcal{E}_r$, the minimum $P_{l,eff}$ (Figure 9) occurs for a greater h (i.e. minimum at h = 50 mils for $\mathcal{E}_r$ of 2 and h = 75 mils for $\mathcal{E}_r$ of 8).

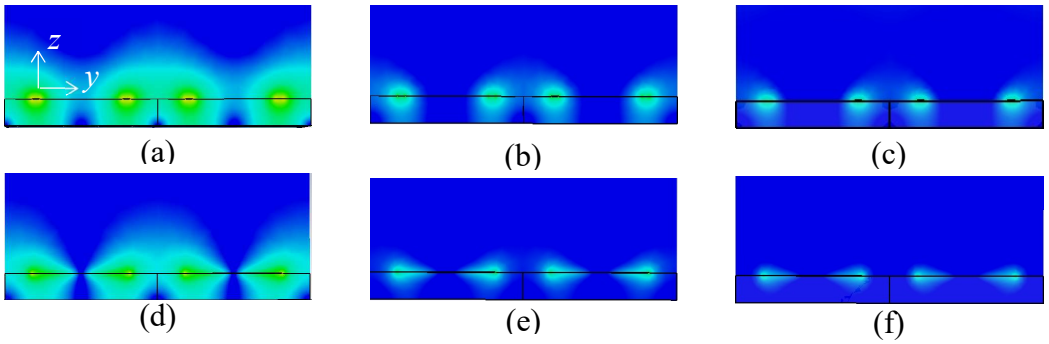

Figure 12. The E-field magnitude in the y-z plane at x = 0 (location of maximum E-field) for h equal to 70 mils and $\mathcal{E}_r$ of (a) 2, (b) 4.3, (c) 8 and the E-field magnitude in the y-z plane at $x=L/2-t_l/2$ (location of nulls) for $\mathcal{E}_r$ equal to (d) 2, (e) 4.3, and (f) 8.

To show the effect of inter-element spacing (S), the dimension in the y direction ("b" in Figure 1b) of unit cell #1 is increased to 22.86 mm, with the other dimensions remaining the same. The new unit cell is herein referred to as unit cell #2. In this way, the inter-element spacing is increased and the coupling between adjacent loop elements

reduced. The E-field is shown in Figure 13 for unit cell #2 on a substrate with $\mathcal{E}_r = 4.3$ and h = 10, 70, and 140 mils. As seen, because of the large spacing between adjacent loop elements, the E-field is concentrated between the loop conductor and ground plane for small h (Figure 13a). However, as h increases, the coupling between two arms of the loop (along the x-direction) also increases, as is shown in Figure 13b-c for h equal to 70 and 140 mils, respectively. The coupling inside of loop unit cell #2 (conductor arms of the loop) dominates since the ratio of distance between arms to h, $(L-2t_w)/h$, for thick substrates is much smaller than the S/h ratio (i.e. for h of 70 mils, $(L-2t_w)/h$ is 3.1 and 9.2, respectively). While S/h was smaller than $(L-2t_w)/h$ for the unit cell #1 (i.e. for h of 70 mils, $(L-2t_w)/h$ = 5.15, S/h = 2). Hence, more coupling inside of the loop also reduces the effect of nulls as well, as is evident in Figure 13b, in comparison with that of loop unit cell #1 on the same substrate with smaller S (see Figure 10e).

As discussed above, the E-field distribution (including fringing fields) differs from that shown in Figure 5a for different design parameters such as S/h and $(b-2t_w)/h$, as a majority of the coupling can take place between adjacent elements or inside the loop. Hence, in order to reduce the coupling between adjacent elements (i.e., unit cell #1, Figure 11b-c) due to small S/h and the coupling inside of the loop element (i.e., unit cell #2, Figure 13b) due to small $(L-2t_w)/h$, unit cell #3 is considered with similar S/h and $(L-2t_w)/h$ ratios. Unit cell #3 has dimensions of $a = b$ = 22.86 mm, $L = W$ = 12.5 mm, and $t_w = t_l$ = 0.5 mm. The E-field on the surface of loop unit cell #3 is shown in Figure 14 for h equal to 10 mils, 70 mils, and 140 mils. As seen, by increasing h, the fringing fields and the null length increase. Also, the E-field coupling with adjacent elements and inside the loop are eliminated as a result of the particular dimensions.

In order to compare the behavior of unit cells with different S/h and $(b-2t_w)/h$, f_{rl} and $P_{l,eff}$ for unit cells #2 and #3 are shown in Figure 15. As seen, over the range of h considered here, f_{rl} of unit cells #2 and #3 solely increases as h increases. This is in contrast with the behavior of f_{rl} of Figure 8 (unit cell #1), where first an increase and then a decrease is evident. This is a result of small S which causes more mutual coupling for thicker substrates and the subsequent increase in $P_{l,eff}$. More specifically, since S is large, E-field coupling between elements is minimal and the behavior is dictated by the presence of nulls (and the effective perimeter). That is to say, for small h, the effect of nulls is dominant (as explained above). However, for large h, since the coupling inside of the loop is greater (see Figure 13b-c), the effect of nulls decreases and $P_{l,eff}$ shows an asymptotic behavior. In addition, the rate of decrease in $P_{l,eff}$ of unit cell #2 is less than that of unit cell #3. This is because unit cell #3 has a larger physical perimeter, and hence the reduction in $P_{l,eff}$ due to the null is less. Also, for unit cell #2, as h increases, the coupling is primarily located within the loop (see Figure 13b) and hence the effect of nulls is reduced and $P_{l,eff}$ is more similar to the interior perimeter. A last point to be made involves $P_{l,eff}$ for $\mathcal{E}_r = 4.3$ of unit cell #2 (Figure 15a); specifically, that is less than that of $\mathcal{E}_r = 8$. This is a result of the behavior of (9) (used to calculate $P_{l,eff}$).

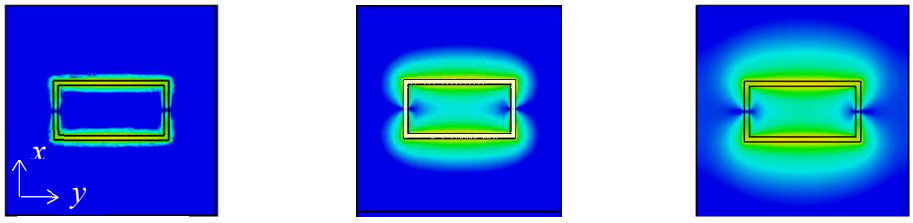

(a) (b) (c)

Figure 13. The E-field magnitude of loop unit cell #2 for h of (a) 10 mils, (b) 70 mils, and (c) 140 mils.

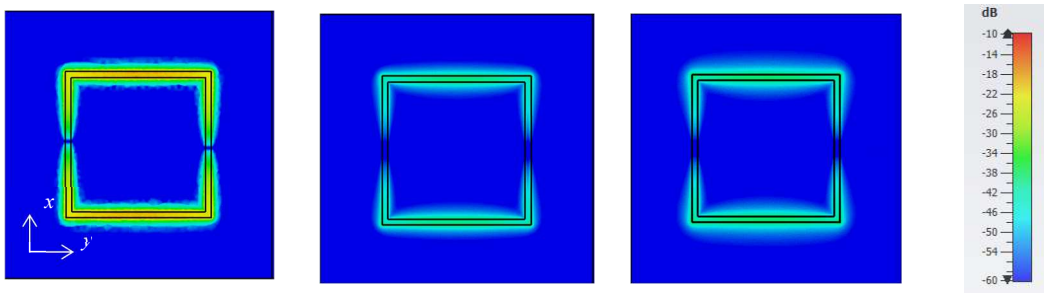

(a) (b) (c) (d)

Figure 14. The E-field magnitude of loop unit cell #3 for *h* of (a) 10 mils, (b) 70 mils, (c) 140 mils and (d) scaling in dB.

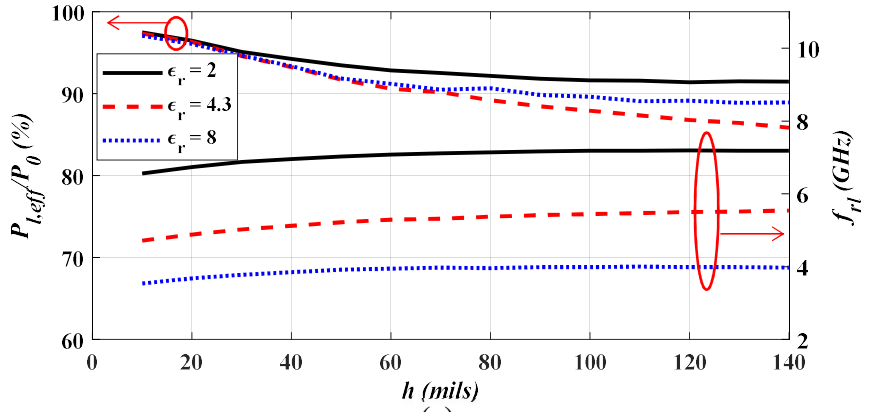

(a)

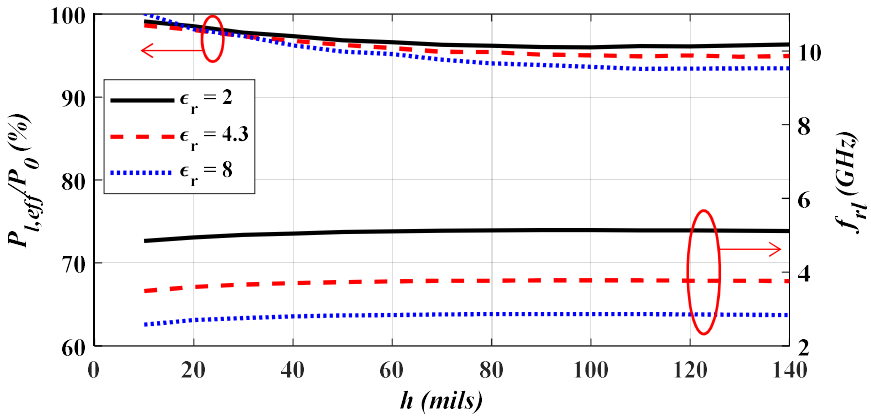

(b)

Figure 15. The resonant frequency and $P_{l,eff}$ of the loop unit cell (a) #2, (b) #3.

4. QUALITY FACTORS AND THE REFLECTION RESPONSE

Using the results of Section 2, in this section, the Q-factor of the rectangular patch and the loop unit cells will be presented in order to calculate the Γ from the patch and loop unit cells. In this Section, the rectangular patch in Figure 1a and loop unit cell #3 are used to show the results of the Q_{rad} model and Γ calculated using Q-factors. It should be noted that to calculate Q_{rad} and Γ, the analytical f_{rp} was used for the patch unit cell. However, the simulated f_{rl} is used for the loop unit cell to avoid the effect of the small difference between the full wave simulation results and those from the analytical model developed above (i.e. Figure 8) on Q_{rad} and Γ.

As discussed in Section 2 and shown in (5), Q_{rad} of the patch and loop in the cavity model depends on W_S and P_{rad} from the resonator coupled into the excited mode (here, fundamental Floquet modes of TE_{00} and TM_{00}). The patch/loop element in the cavity model with an excitation mode of TM_{010} has the field distribution beneath the element given in (7) and shown in Figure 2, along with the equivalent magnetic current direction on each longer edge ($\vec{M}$). Hence, to find an analytical expression for Q_{rad} (5) of an element, W_S and P_{rad} are required. However, in the cavity model of [18], [20], the fringing fields are ignored. Therefore, in order to develop a more accurate expression for $Q_{rad,}$ the physical extension of the geometry due to the fringing fields is taken into account (as discussed above). Additionally, the surface wave effect (seen in thicker substrates) is included since the radiation by the element for thick substrates will be reduced by surface waves [21], [23]. In other words, the surface wave efficiency, η_{SW}, is included as a coefficient in Q_{rad} in order to capture the effect of the surface waves and is defined as follows:

$$\eta_{SW} = \frac{P_{SP}}{P_{SP} + P_{SW}} \tag{10}$$

where P_{SP} is the space-wave radiated power and P_{SW} is the surface wave power (both of which are defined in [20]).

Using the approach presented in [18] for the patch unit cell, the general form of Q_{rad} for any element type can be defined for TE_{00} and TM_{00} incident modes and including η_{SW} as follows:

$$Q_{rad,TE} = \eta_{SW} \pi f_r \varepsilon_r ab \frac{\eta_0}{\cos\theta \cos^2 \varphi} \alpha, \tag{11}$$

and

$$Q_{rad,TM} = \eta_{SW} \pi f_r \varepsilon_r ab \frac{\eta_0 \cos\theta}{\sin^2 \varphi} \alpha \tag{12}$$

where α is a constant related to element geometry, W_S and P_{rad}. In this way, general expressions can be defined for Q_{rad} and the element details captured within specific values of α (i.e., α_p for the patch and α_l for the loop, as is described below).

Using this approach, for the rectangular patch element, Q_{rad} is determined by considering $\alpha_p = L_{eff} / 4hW$. However, Q_{rad} of the rectangular loop is more complicated when the fringing fields are considered. Therefore, W_S and P_{rad} of the loop are defined first. To this end, W_S is found as:

$$W_S = \frac{\varepsilon}{4} \iiint |\vec{E}|^2 \, dv. \tag{13}$$

To add the physical extension of the loop element (area) due to the fringing fields, the loop element is considered as 10 sections, as is shown in Figure 16. Also, the effect of fringing field on the width of the loop along *x*- and *y*-directions and corners are considered

as shown in Figure 5a and explained in Section 3. By using this fringing field model, the stored energy is found by calculating the summation of the volume integral of ten sections of the loop (Figure 16) with limits of integral along *x*-and *y*-directions by considering th width extension as shown in Figure 5a. As such, W_S from (13) is calculated for the loop element as follows:

$$W_S = \frac{\varepsilon}{4} h \sum_{i=1}^{10} \iint_{S_i} |\vec{E}|^2 \, dydx \tag{14}$$

where $\sum_{i=1}^{10} \iint_{S_i} |\vec{E}|^2 \, dydx = \chi_1 E_0^2$. A detailed derivation is available in Appendix in (4)-(5).

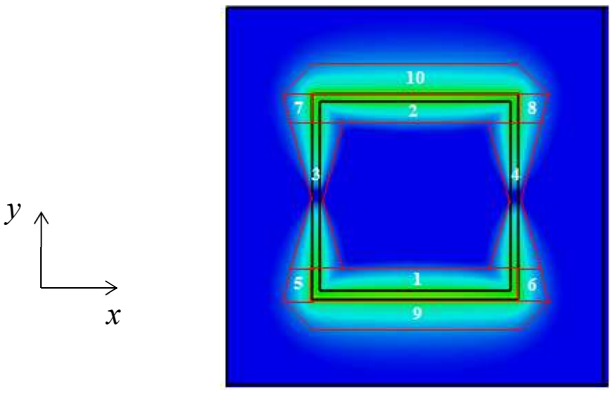

Figure 16. The fringing field model of the loop element including illustrating 10 sections.

Next, to find P_{rad} into the Floquet excitation mode using the volume magnetic current density, the reflected wave amplitude (A^+) can be found by evaluating the volume integral of the product of the magnetic current density and magnetic field (which is the modal magnetic field of Floquet TE or TM modes) [15], [17]. A^+ for both TE and TM modes is given as [15]:

$$A_{TE}^{+}=\frac{1}{P_{TE}}\iiint_{v}\vec{h}_{TE}.\vec{M}dv,\qquad A_{TM}^{+}=\frac{1}{P_{TM}}\iiint_{v}\vec{h}_{TM}.\vec{M}dv \tag{15}$$

where $P_{TE}=2/Z_{TE}$ and $P_{TM}=2/Z_{TM}$. Z_{TE} and Z_{TM} are the wave impedances for TE and TM modes. The wave impedance for the fundamental Floquet TE_{00} and TM_{00} modes are as follows [15]:

$$Z_{TE}=\frac{\eta_0}{\mathrm{Cos}\,\theta},\qquad Z_{TM}=\eta_0\,\mathrm{Cos}\,\theta \tag{16}$$

where η_0 is the free space impedance. It should be mentioned that the volumetric integrals over the edges (parallel to the *y*-*z* plane, Figure 2b) are zero. Then, A_{TE}^{+} due to the magnetic currents ($\vec{M}$) on the edges (walls parallel to the *x*-*z* plane shown in Figure 2b) is as follows:

$$A_{TE}^{+}=\frac{1}{P_{TE}}\left\{\sum\int\vec{h}_{TE}.\vec{M}dx\right\} \tag{17}$$

where $\vec{M}=-2hE_0\hat{x}$ and $\vec{M}=2hE_0\sin(\pi(L-2t_l)/2L)\hat{x}$ at $y=\pm L/2$ and $y=\pm L/2\mp t_l$, respectively. Also, the magnetic current at the corners has a component along the *x*-direction which contribute in A_{TE}^{+} which is $\vec{M}=-\sqrt{2}hE_0\hat{x}$ at the corners of the area 9 and 10 as shown Figure 16, respectively. Therefore, A_{TE}^{+} is calculated in the Appendix as:

$$A_{TE}^{+}=\frac{2hE_0\chi_2\cos\varphi}{\sqrt{ab}},\qquad A_{TM}^{+}=\frac{2hE_0\chi_2\sin\varphi}{\sqrt{ab}} \tag{18}$$

where $\chi_2=W-(W-2t_l-2\delta t_l\sin\pi y_0/L)\sin\pi y_0/L+\sqrt{2}\delta t_l$ and $y_0=L/2-t_W-\delta t_W\sin\pi(L/2-t_W)/L$ as derived in the Appendix. Hence, P_{rad} for TE and TM modes is as follows:

$$P_{rad,TE}=\frac{|A_{TE}^{+}|^2}{Z_{TE}}=\frac{4h^2E_0^2\chi_2^2\cos^2\varphi\cos\theta}{ab\eta_0}, \tag{19}$$

which are shown for the fundamental Floquet modes of TE_{00} and TM_{00}. Hence, the Q_{rad} of the loop for TE and TM modes can be found from (11) and (12), when $\alpha_l = \chi_1 / 8\chi_2^2$ where χ_1 is provided in the Appendix (2) and χ_2 is given above.

4.1. CALCULATION OF THE QUALITY-FACTORS

As mentioned before, the relative values of $Q_{rad,TE}$ and $Q_{rad,TM}||Q_0$ of the unit cell create different coupling conditions (for TE mode). Hence, the Q-factors of the patch and loop unit cells are presented as a function of h for ε_r = 2, 4.3, and 8 (as above in Section 3) and $tan\delta$ = 0.023 and 0.09 in Figure 17 and Figure 18, respectively. Here, two different values of $tan\delta$ are considered to show the effect of dielectric loss on Q_0 and consequently Γ. The results are for normal incidence ($\theta = \varphi = 0$), meaning $Q_{rad,TM}$ is infinite and hence $Q_{rad,TM}||Q_0 = Q_0$. In all cases, when h increases, $Q_{rad,TE}$ reduces. This is due to the fact that W_S is directly proportional to h (14), while P_{rad} is proportional to h^2 (19)-(20). In this way, P_{rad} will have a dominant effect on $Q_{rad,TE}$.

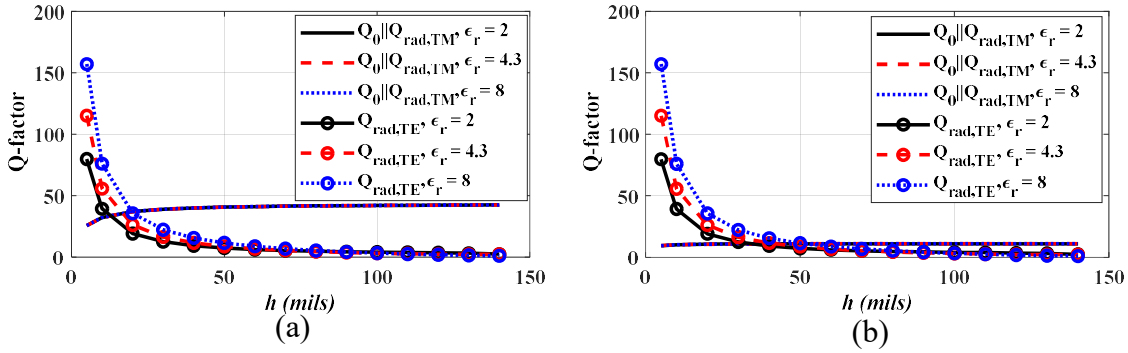

Figure 17. Analytical model results of Q-factors vs. h for patch unit cell on a substrate with $tan\delta$ of (a) 0.023 and (b) 0.09.

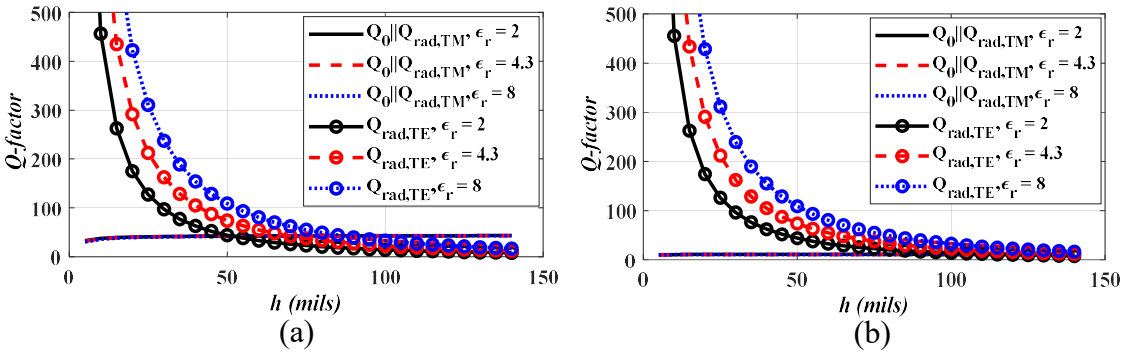

Figure 18. Analytical model results of Q-factors vs. h for loop unit cell on a substrate with $tan\delta$ of (a) 0.023 and (b) 0.09.

In addition, for all cases, when h increases, Q_c ($h\sqrt{\pi f \mu \sigma}$), and consequently Q_0, (4), will increase. However, since Q_c is large (due to large σ), Q_0 will be closer to Q_d ($1/tan\delta$). This is why for different $\mathcal{E}_r$ (and fixed $tan\delta$), $Q_0||Q_{rad,TM}$ is almost equivalent. Hence, as seen in Figure 17 and Figure 18, $Q_0||Q_{rad,TM}$ increases slightly with increasing h and has asymptotic behavior as h continues to increase. In addition, a larger $tan\delta$ will result in a lower Q_d and consequently a lower Q_0, as seen in Figure 17a for the patch unit cell on the substrate with $tan\delta$ of 0.023 in comparison with Figure 17b for $tan\delta$ of 0.09. Similar behavior for Q_0 of the loop is shown in Figure 18.

The substrate permittivity ($\mathcal{E}_r$) affects the stored energy in the cavity resonator. As $\mathcal{E}_r$ increases, W_S (5) increases because the E-field is more confined, which results in an increase in $Q_{rad,TE}$ for all cases. This is more obvious for thinner substrates when $Q_{rad,TE}$ is greater than $Q_{rad,TM}||Q_0$ in Figure 17 and Figure 18.

Additionally, the loop unit cell, with the same dimensions as the patch unit cell, has a larger $Q_{rad,TE}$. This is due to the fact that, while the loop has a smaller W_S and P_{rad}, the ratio, which is proportional to Q_{rad}, is larger. Also, Q_{rad} is directly proportional to resonant

frequency (5). As shown in Figure 4a and Figure 8/Figure 15b (f_{rp} and f_{rl}, respectively), the loop unit cell (as compared to the patch) has a lower resonant frequency but still a larger Q_{rad} due to the effect of the ratio of W_S to P_{rad}. As a result, for equivalent loop and patch dimensions (as is the case here), the loop must have a thicker substrate (larger h) as compared to the patch to achieve the FSS operation coupling condition of $Q_{rad,TE} = Q_{rad,TM}||Q_0$. That is to say, in Figure 17a (patch), this condition is met for values of h between 10-20 mils, and in Figure 18a (loop), for values of h between 50-80 mils.

4.2. CALCULATION OF THE REFLECTION COEFFICIENT RESPONSE

Next, using the calculated Q-factors, $\Gamma_{TE,co}$ is calculated in terms of frequency from (1) as a function of substrate thickness and dielectric properties. For the patch unit cell, the analytical f_{rp} (shown in Figure 4a) is used in $Q_{rad,TE}$. The same has also been simulated using CST for comparison. Specifically, the resonant depth in terms of h is shown for the patch unit cell in Figure 19. As can be seen, there is a good agreement between the simulated response and analytical results for h = 5 mils to 140 mils and $tan\delta$ of 0.023 and 0.09. The maximum resonant depth occurs (for TE excitation) when $Q_{rad,TE} = Q_{rad,TM}||Q_0$ (i.e., the condition necessary for FSS application). For the cases considered here (and as seen in Figure 19), a thinner substrate is needed for FSS operation when $tan\delta$ is low (0.023). For example, for $\mathcal{E}_r$ of 4.3, the maximum resonant depth occurs for h = 10 mils when $tan\delta$ = 0.023 (Figure 19a), while h = 40 mils required when $tan\delta$ increases to 0.09 (Figure 19b). Also, as $\mathcal{E}_r$ increases (for a fixed $tan\delta$), the maximum resonant depth is achieved for a thicker substrate.

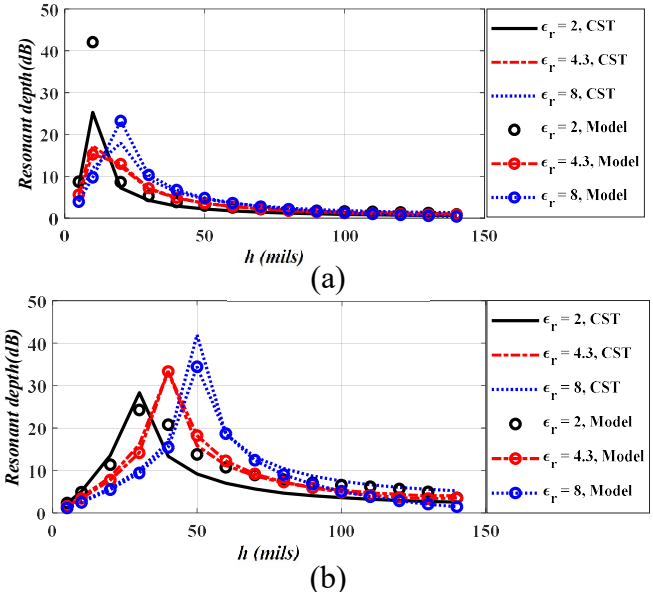

Figure 19. Comparison of simulated and analytical model results for the patch unit cell resonant depth vs. *h* for a substrate with *tanδ* of (a) 0.023 and (b) 0.09.

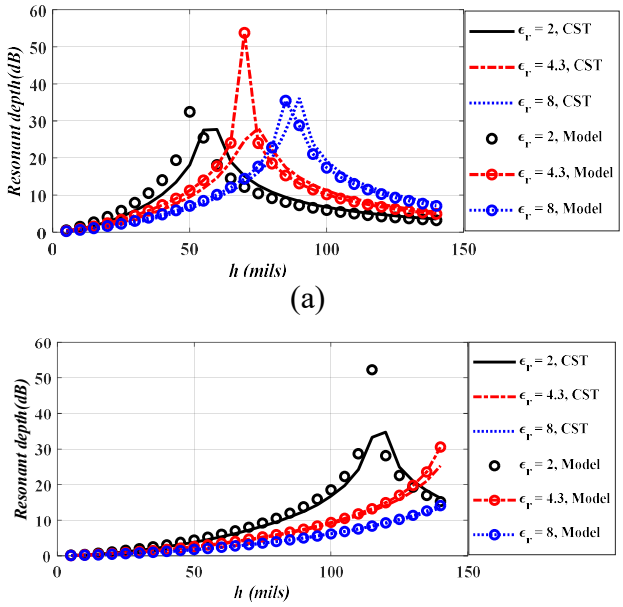

Figure 20. Comparison of simulated and analytical model results for the loop unit cell resonant depth vs. *h* for a substrate with *tanδ* of (a) 0.023 and (b) 0.09.

A similar approach is considered to calculate $\Gamma_{TE,co}$ (1) of the loop unit cell using the $Q_{rad,TE}$ and $Q_{rad,TM}$ of the loop from (11) and (12). Since f_{rl} is related to $P_{l,eff}$, the simulated resonant frequency of the loop unit cell is used to avoid any discrepancy in Γ due to the difference in the analytical and simulated f_{rl}. The resonant depth of $\Gamma_{TE,co}$ of the loop unit cell is shown in Figure 20 versus h. As seen, a similar trend (to the patch) occurs for the resonant depth of the loop unit cell, except a thicker substrate is required (in comparison with the patch) for a given $\mathcal{E}_r$ and $tan\delta$. This is because the loop has a larger $Q_{rad,TE}$ than the patch, and consequently the maximum resonant depth (where $Q_{rad,TE} = Q_{rad,TM}||Q_0$) occurs for a thicker substrate (as discussed earlier). The resonant depth of the loop unit cell for $tan\delta = 0.023$ shows good agreement between simulation and the analytical results. As mentioned for $Q_{rad,TE} = Q_{rad,TM}||Q_0$, Γ at the resonance is zero. Hence, the difference in simulation and modeling of the patch and loop unit cells for the cases with larger resonant depth ($Q_{rad,TE}$ and $Q_{rad,TM}||Q_0$ are almost equivalent) are attributed to small differences in the calculated $Q_{rad,TE}$. As an example, the resonant depth result shown in Figure 19a for the patch when $\mathcal{E}_r$ is 2 and h is 10 mils. Also, the resonant depth results of the loop shown in Figure 20 has a large difference with the full-wave simulation results for low loss material when $\mathcal{E}_r$ is 4.3 and h is 70 mils (Figure 20a) and for high loss substrate when $\mathcal{E}_r$ is 2 and h is 120 mils (Figure 20b).

5. CONCLUSION

In this paper, an analytical approach for an infinite FSS using Floquet excitation and based on a quality factor analysis is used to define the reflection coefficient of a unit

cell with periodic boundary. This approach is used for rectangular patch and loop unit cells with conductor-backed substrates, which are modeled as a cavity with the dominant excitation mode of TM_{010}. To expand the Q-factor model for a wide range of substrate properties from the current model, the effect of fringing fields and the frequency dependent effective permittivity are included. The fringing field effect on the patch element is well-known and its resonant frequency is related to the effective length of the patch along the interrogating polarization. However, resonant frequency of the loop is related to the effective perimeter of the loop. It is shown that the effective perimeter (the average of interior and exterior perimeters) of the loop depends on the mutual coupling between adjacent elements, the coupling between conductor arms of the loop, and the excitation mode of the loop (here, it is shown for TM_{010} mode). Hence, the effective perimeter of the loop is evaluated for different loop designs using the effective permittivity and resonant frequency from the full wave simulation of the loop unit cell. In addition, to find the radiation Q-factor, the extension of the geometry of the elements due to fringing field are considered. The model for the radiation Q-factor for the patch is modified and a model for the radiation Q-factor of the loop is developed at the resonant frequency of the elements. Then, using radiation, conductor and dielectric Q-factors of each unit cell, the analytical reflection coefficient in terms of frequency for the patch and loop unit cells are calculated. The analytical results are in good agreement with the full wave simulation results for a wide range of permittivity (2-8), $tan\delta$ (0.02-0.09), and substrate thickness (5 mils to 140 mils).

APPENDIX

Regarding to the average perimeter of the loop element by considering the effective dimension due to the fringing fields, the model in Figure 5a is considered as explained in subsection 3.2. The exterior perimeter includes four equal curved sections (l_{ext}) along both shorter edges (two per edge). The line integral along the length of this curvature path is evaluated assuming $\vec{l} = \hat{x}dx + \hat{y}dy + \hat{z}dz$ to find l_{ext} as follows:

$$l_{ext} = \int |\, \vec{dl}\, | = \int\ dy \sqrt{\left(\frac{dx}{dy}\right)^2 + 1 + \left(\frac{dz}{dy}\right)^2} \tag{1}$$

To find l_{ex} on the top right curvature in Figure 5a, the x position is written as a function of y as $x = W/2 + \delta t_l \sin(\pi L / y)$. Hence, $dx/dy = (\pi \delta t_l / L)\cos(\pi L / y)$. Therefore, (20) can be calculated as shown below:

$$l_{ext} = \int_0^{L/2} \sqrt{1 + \left(\frac{\pi \delta t_l}{L}\right)^2 \cos^2\left(\frac{\pi y}{L}\right)}\, dy \tag{2}$$

To calculate l_{ext} from (22), MATLAB is used. Hence, the exterior perimeter is calculated as $P_{ext} = 4l_{ext} + 2(W + 2\sqrt{\delta t_l{}^2 + \delta t_W{}^2})$. A similar process is used for the other three curved sections.

To calculate the interior perimeter (P_{int}), a similar approach is used. The extension of t_l toward the interior side of the loop is a function of y (as explained in Subsection 3.2). Hence, the length of curvature (l_{int}) is calculated using (21) for the range of y from 0 to $y_1 = L/2 - t_W - \delta t_W \sin(\pi(L/2 - t_W)/L)$ and calculated in MATLAB. Then,

$P_{\text{int}} = 4l_{\text{int}} + 2(W - 2t_l - 2\delta t_l \sin(\pi y_1 / L)$. Therefore, P_{fringe} is considered as the average of P_{ext} and P_{int}.

Next, the calculation of W_S for the loop unit cell is explained. As mentioned in Section 4, in order to calculate the reflection coefficient $\Gamma(f)$, of the unit cell backing a conductor using Q-factors, Q_{rad} of the element is required. Hence, to find the Q_{rad} of a conductor backed loop element into the waveguide, the approach shown in [18] for patch element is used here (see Figure 1). In this way, the loop element with conductor on the back of the substrate is modeled as cavity with dominant mode of TM_{010}. It is also considered as a load at the end of a waveguide transmission line, which is excited by fundamental Floquet modes (TE_{00}, and TM_{00}). To calculate Q_{rad} from (5) and considering the dimension extension of the loop element, it is considered as ten segments as shown in Figure 16. Therefore, the stored energy (W_S) and radiated power into the excited modes (P_{rad}) are required. W_S is calculated from (13) as a summation of the volumetric integral over each piece of the loop (Figure 16) as (14). To calculate W_S from (14), the integral ranges are commensurate with the fringing fields of Figure 5a. Hence, in (14), $W_S = (\varepsilon h / 4)\sum_{i=1}^{10} \iint_{S_i} |\vec{E}|^2 \, dydx$ is equal to $(\varepsilon h / 4) E_0^2 \chi_1$ where

$$\chi_1 E_0^2 = \int_{-L/2}^{-L/2+t_w+\delta t_w \sin y_0} \int_{-W/2}^{w/2} |\vec{E}|^2\, dxdy + \int_{L/2-t_w-\delta t_w \sin y_0}^{L/2} \int_{-W/2}^{w/2} |\vec{E}|^2\, dxdy +$$

$$\int_{-L/2+t_w+\delta t_w \sin y_0}^{L/2-t_w-\delta t_w \sin y_0} \int_{-W/2-\delta t_l \sin\frac{\pi y}{2L}}^{-W/2+t_l+\delta t_l \sin\frac{\pi y}{L}} |\vec{E}|^2\, dxdy + \int_{-L/2+t_w+\delta t_w \sin y_0}^{L/2-t_w-\delta t_w \sin y_0} \int_{W/2-t_l-\delta t_l \sin\frac{\pi y}{L}}^{W/2+\delta t_l \sin\frac{\pi y}{L}} |\vec{E}|^2\, dxdy +$$

$$\int_{-L/2}^{-L/2+t_w+\delta t_w \sin y_0} \int_{-w/2-\delta t_l}^{-w/2-\delta t_l \sin\frac{\pi y}{L}} |\vec{E}|^2\, dxdy + \int_{-L/2}^{-L/2+t_w+\delta t_w \sin y_0} \int_{w/2+\delta t_l \sin\frac{\pi y}{L}}^{w/2+\delta t_l} |\vec{E}|^2\, dxdy +$$

$$\int_{L/2-t_w-\delta t_w \sin\frac{\pi y_0}{L}}^{L/2} \int_{-W/2-\delta t_l}^{-W/2-\delta t_l \sin\frac{\pi y}{L}} |\vec{E}|^2\, dxdy + \int_{L/2-t_w-\delta t_w \sin\frac{\pi y_0}{L}}^{L/2} \int_{W/2-t_l-\delta t_l \sin\frac{\pi y}{L}}^{W/2+\delta t_l} |\vec{E}|^2\, dxdy +$$

$$2E_0^2 \delta t_W (L+\delta t_l) = E_0^2 \chi_1 \tag{3}$$

The χ_1 is found as

$$\begin{aligned}
\chi_1 &= W\left[(t_W + \delta t_W \sin\frac{\pi y_0}{L}) + \frac{L}{2\pi}\sin\frac{\pi}{L}(\frac{L}{2} - t_W - \delta t_W \sin\frac{\pi y_0}{L})\right] \\
&+ t_l(L - 2t_W - 2\delta t_W \sin\frac{\pi y_0}{L}) - \frac{t_l L}{\pi}\sin\frac{\pi}{L}(\frac{L}{2} - t_W - \delta t_W \sin\frac{\pi y_0}{L}) + \\
&2\delta t_l(t_w + \delta t_w \sin\frac{\pi y_0}{L}) - \frac{\delta t_l L}{3\pi}\sin\frac{3\pi}{L}(\frac{L}{2} - t_W - \delta t_W \sin\frac{\pi y_0}{L}) + \\
&2\delta t_W(\delta t_l + W)
\end{aligned} \tag{4}$$

The Prad is also calculated. To find it, A_{TE}^{+} is calculated as follows:

$$\begin{aligned}
A_{TE}^{+} &= \left(\frac{4hE_0}{P_{TE/TM}}\right) \\
&= \left\{\int_{-W/2}^{W/2} \vec{h}_{TE}.(-\hat{x})dx + \int_{-W/2+t_l}^{W/2-t_l} \vec{h}_{TE}.(-\sin\frac{\pi}{L}y_0\hat{x})dx + \int_{-W/2}^{-W/2-\delta t_l} \vec{h}_{TE}.(\frac{-\hat{x}}{\sqrt{2}})dx + \int_{W/2+\delta t_l}^{W/2} \vec{h}_{TE}.(\frac{-\hat{x}}{\sqrt{2}})dx\right\} \\
&= \left(\frac{4hE_0}{P_{TE}}\right)\chi_2
\end{aligned} \tag{5}$$

where $\chi_2 = W - (W - 2t_1 - 2\delta t_1 \sin\frac{\pi}{L} y_0) \sin\frac{\pi}{L} y_0 + \sqrt{2}\delta t_1$ and $y_0 = L/2 - t_W - \delta t_W \sin\pi(L/2 - t_W)/L$

. Hence, P_{rad} for TE and TM modes can be found from (19), and (20), respectively. From this, the final expression of Q_{rad} for the fundamental Floquet modes are presented in Section 4.

REFERENCES

[1] B. A. Munk, *Frequency Selective Surfaces Theory and Design*, NewYork: Wiley, 2000.

[2] M. Li, Mudar A. Al-Joumayly, and Nader Behdad, "Broadband True-Time-Delay Microwave Lenses Based on Miniaturized Element Frequency Selective Surfaces," *IEEE Transactions on Antennas and Propagation* 61, No. 3, pp.1166-1179, 2013.

[3] X. D. Hu, et al, "A miniaturized Dual-Band Frequency Selective Surface (FSS) with Closed Loop and its Complementary Pattern," *IEEE Antennas and Wireless Propagation Letters* 8, pp 1374-1377, 2009.

[4] Rashi id, A. K., et. al, "A novel band-reject frequency selective surface with pseudo-elliptic response," *IEEE Transactions on Antennas and Propagation*, Vol. 8, No. 4, pp. 1220-1226, 2010.

[5] F. Costa, et al, "A frequency Selective Radome with Wideband Absorbing Properties," *IEEE Transactions on Antennas and Propagation* 6, No. 6, pp. 2740-2747, 2012.

[6] H. Chen, et al, "Design of Frequency-Selective Surfaces Radome for a Planar Slotted Waveguide Antenna," *IEEE Antennas and Wireless Propagation Letters* 8, pp. 1231-1233, 2009.

[7] A. Edalati, and Kamal Sarabandi, "Wideband, wide angle, polarization independent RCS reduction using nonabsorptive miniaturized-element frequency selective surfaces", *IEEE Trans. on Ant. and Prop.*, Vol. 62, No. 2, pp. 747-754, 2014.

[8] Mei Li, et al., "An Ultrathin and broadband broadband Absorber Using Resistive FSS", *IEEE Trans. on Ant. and Prop*, Vol. 11, pp. 748-751, 2012.

[9] M. Mahmoodi, et al, "Wideband Multi-Loop FSS Absorber Design Based on Q-factor Approach," *2018 IEEE International Symposium on Antennas and Propagation & USNC/URSI National Radio Science Meeting*. IEEE, pp. 2061-2062 2018.

[10] F. Costa, et al, "A circuit-based model for the interpretation of perfect metamaterial absorbers," *IEEE Transactions on Antennas and Propagation* Vol. 61, No. 3, pp. 1201-1209, 2012.

[11] M. Mahmoodi, et al, "Novel FSS-Based Sensor for Concurrent Temperature and Strain Sensing," *2017 IEEE International Symposium on Antennas and Propagation & USNC/URSI National Radio Science Meeting.* IEEE, pp. 679-680, 2017.

[12] D. F. Pieper, et al, "Application of Frequency Selective Surfaces for Inspection of Layered Structures," *2015 IEEE International Instrumentation and Measurement Technology Conference (I2MTC)*. IEEE, 2015.

[13] M. Mahmoodi, et al, "Performance Metrics for FSS-Based Sensors," *IEEE Sensor Letters 1*, No. 6, Nov. 2017.

[14] A. K. Bhattacharyya*, Phased Array Antennas: Floquet analysis, Synthesis, BFNs and Active Array Systems*. New York, NY, USA:Wiley, 2005.

[15] Kalyan K. Karnati, et al. "Q-Factor Analysis of Reflectarray Elements Investigating the Effects From Angle of Incidence Using Floquet Modes," IEEE Transactions on Antennas and Propagation Vol. 62, No. 10, pp. 5017-5028, 2014.

[16] C. A. Balanis*, Antenna Theory: Analysis and Design*, 3rd ed. New York, USA: Wiley, 2006, ch. 14.

[17] D. M. Pozar*, Microwave Engineering*, 3rd ed. NY, USA: Wiley, 2005.

[18] C. J. Vourch, et. al., "Analytical and full-wave analysis of square and ring patch structures for reflectarray unit cells," *The 8th European Conference on Antennas and Propagation (EuCAP 2014)*. IEEE, 2014.

[19] C. A. Balanis, *Advanced Engineering Electromagetics*, Wiley, 1989, Ch. 8.

[20] M. David Pozar, "Rigorous closed-form expressions for the surface wave loss of printed antennas," *Electronics Letters* Vol. 26, No. 13, pp. 954-956, 1990.

[21] Jia-Shen G Hong, et. al., *Microstrip filters for RF/microwave applications*. Vol. 167, John Wiley & Sons, 2004, Ch. 4.

II. PERFORMANCE METRICS FOR FREQUENCY SELECTIVE SURFACE-BASED SENSORS

ABSTRACT

A frequency selective surface (FSS) is a periodic array of conductive elements (located on a dielectric substrate) that has a specific transmission or reflection response when illuminated with electromagnetic energy. Since the FSS response is sensitive to changes in substrate properties (permittivity, loss tangent, and thickness) as well as element geometry, FSS-based sensors have strong potential as a wireless sensing solution. To this end, this paper proposes three performance metrics (resonant frequency, resonant depth, and quality factor) to quantify the effect of substrate properties on sensor performance. These metrics are applied to a patch- and loop-based FSS sensor. The results show that the patch-based sensor has improved performance when designed using a thinner and high loss substrate, while the loop-based sensor has better performance when a substrate with less loss but increased thickness is used. Additionally, measurements are also provided for sensors utilizing the low loss substrate. Lastly, the performance of the two sensors is shown for strain sensing. The results indicate that the resonant frequency shift (when under mechanical loading) of both sensors is largely independent of the substrate permittivity.

1. INTRODUCTION

Frequency selective surfaces (FSSs) are periodic arrays of conductive elements located on a dielectric substrate. These arrays have a specific reflection or transmission

response that is directly related to the element geometry and spacing (often referred to as the unit cell), substrate thickness, and dielectric properties near the FSS (dielectric substrate and surrounding environment) [1]. As such, FSS-based sensors have recently shown potential for structural health monitoring (SHM) applications. More specifically, FSS-based sensing has been used for crack detection [2], normal strain sensing by monitoring the shift in resonant frequency (f_r) [3], and shear strain sensing by monitoring the cross-polarized reflection response (meaning the polarization of the reflected signal was orthogonal to that of the interrogating signal). In addition, [4] considered an FSS sensor for delamination detection. FSS sensors have also been used in the terahertz regime to monitor paper thickness and humidity changes [5].

FSS sensors can be designed to operate in reflection or transmission mode. This is important as it relates to the practicality of the sensor, as a sensor designed to operate in reflection mode is interrogated in a single-sided manner, while transmission mode requires a two-sided inspection. For many applications, accessibility to both sides of a structure is challenging or impossible to achieve (e.g., bridge deck, aircraft, etc.). Thus, the sensors considered in this work operate in reflection mode. In this way, the sensor response can be measured by measuring the complex reflection coefficient, Γ, when illuminating the sensor with electromagnetic energy.

In order to better understand the relationship of Γ with the FSS sensor design, an approach similar to [6] is used to evaluate FSS sensor performance. More specifically, in [6], the reflection response of a reflectarray unit cell (similar to a conductor-backed FSS unit cell) is studied using an equivalent coupled resonator approach. To this end, the reflection coefficient is given as [6]:

$$\Gamma(f) = \frac{\frac{1}{Q_{rad}} - \frac{1}{Q_0} - \frac{2j(f - f_r)}{f_r}}{\frac{1}{Q_{rad}} + \frac{1}{Q_0} + \frac{2j(f - f_r)}{f_r}} \quad (1)$$

where Q_{rad} is the radiation quality factor (Q-factor) and is given as $Q_{rad} = 2\pi f_r \frac{Energy\ \ Stored}{P_{rad}}$, P_{rad} is radiated power, and Q_0 is a parallel combination of two Q-factors that represent conductive losses $Q_C = h\sqrt{\pi f \mu \sigma}$ (h is substrate thickness) and dielectric losses Q_d = 1/tanδ, (tanδ is the loss tangent of the substrate) and is given as $Q_0 = \frac{Q_c Q_d}{Q_c + Q_d}$.

As discussed in [6], based on the relative values of Q_{rad} and Q_0, three different conditions exist: 1) when $Q_{rad} = Q_0$, there is no reflection at f_r and the energy is dissipated in the unit cell; 2) when $Q_{rad} < Q_0$, the unit cell will resonate and the response is totally reflective (desirable for reflectarray design); and 3) when $Q_{rad} > Q_0$ the phase of the reflection response at f_r is 180°. The condition $Q_{rad} = Q_0$ results in a resonant reflection response (i.e. zero reflections) at f_r, as shown in (1). It is this condition that is met by an FSS at its resonant (design) frequency. Since the substrate properties directly affect the reflection response of an FSS-based sensor, this Q-factor approach for modeling the reflection properties of the sensor can be used to explain and quantify the performance of a sensor. Specifically, the performance metrics are defined and applied to two FSS sensors (patch- and loop-based). In this way, the effect of substrate thickness, permittivity (ε_r) and tanδ on the sensor performance are studied from a resonant cavity perspective [6] through simulation and measurement. Based on the conclusions from the proposed metrics, a design flowchart is provided as a design guide to evaluate and optimize FSS sensor performance. Lastly, the performance of the FSS sensors for strain sensing is also considered.

2. PERFORMANCE METRICS

In order to quantify the performance of a given FSS design, three performance metrics are defined: resonant frequency (f_r), resonant depth, and Q-factor. For this work, Q-factor is defined as the ratio of f_r to BW of $|\Gamma|$ when $|\Gamma|$ is less than -10 dB. In this way, a reflection response that is measureable in the presence of noise/other environmental reflections is ensured.

Many basic FSS designs are based on patch- and loop-type elements, with more complex designs featuring combinations of these structures. Accordingly, the performance of two different sensors (unit cells shown in Figure1), one with a rectangular patch unit cell and the other a loop unit cell with similar dimensions to that of the patch, are chosen to be analyzed and their performance quantified with proposed performance metrics. The dimensions of the patch were chosen to achieve resonance in the X-band (8.2-12.4 GHz) with a substrate permittivity (ε_r) of 4.3 and tanδ = 0.023 (i.e., FR4). As such, to facilitate measurements, the patch unit cell periodicity is defined equal to X-band dimensions (22.86 mm × 10.16 mm) and its dimensions are D = 6.5 mm and L = 12.5 mm. The loop unit cell has the same periodicity (and a width of 0.5 mm) in order to keep both unit cells dimensionally comparable.

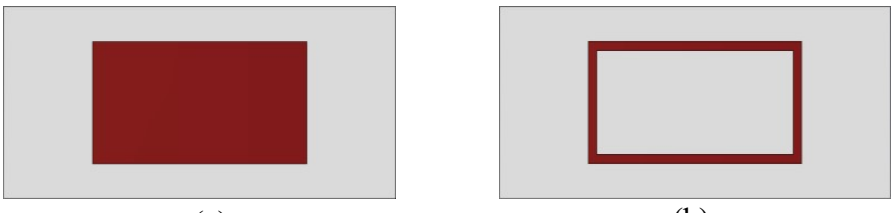

(a) (b)

Figure 1. FSS unit cells (a) patch, (b) loop.

2.1. EFFECT OF SUBSTRATE

In order to study the effect of dielectric properties and substrate thickness on the performance of the two sensor designs of Figure1, full wave electromagnetic simulations were conducting using CST Microwave Studio©. A change in dielectric properties may occur in practice if the substrate properties of an FSS sensor were to change (such as due to cracking or moisture ingress). Therefore, it is important to understand how such changes will affect the sensor performance. Additionally, considering the effect of substrate thickness on sensor performance is useful in the design phase in order to determine whether a thick or thin substrate will provide optimal performance. To this end, for both unit cells of Figure1, two substrates were considered; one with tanδ = 0.09 (a high loss substrate) and one with tanδ = 0.023 (the value for FR4 and representing a low loss substrate). For both cases, ε_r of 2, 4.3, and 8 were considered.

Figure2 shows the effect of substrate thickness on the three performance metrics for both sensor designs for a high loss dielectric substrate. As shown in Figure2a, f_r is reduced for both unit cells as ε_r increases. This trend can be explained by considering $f_r = v_p/\lambda$, where the wave speed $v_p = c/\sqrt{\varepsilon_r}$, and c is the speed of light. Thus, as ε_r increases, the wave speed is reduced and f_r as well. However, the effect of substrate thickness is different for each unit cell. For the patch, f_r decreases with increasing substrate thickness. Conversely, f_r of the loop increases with substrate thickness up to 20 mils and after that remains constant. The behavior of the patch can be explained by considering the patch element as a patch antenna [7]. Thus, $f_r = c/2L_{eff}\sqrt{\varepsilon_{eff}}$, where L_{eff} is the effective electrical length of the patch taking into account the effect of fringing fields and ε_{eff} is effective permittivity (considering the substrate and dielectric material above the unit cell), as is the

case for microstrip lines [7]. Hence, when the substrate thickness increases, the stored energy decreases, causing more fringing fields and a subsequent increase in L_{eff} and decrease in f_r. Additionally, ε_{eff} itself decreases slowly with increasing substrate thickness, thereby having a negligible effect. Therefore, as can be seen in Figure 2a, f_r of the patch decreases with increasing substrate thickness. On the other hand, f_r of the loop increases with increasing substrate thickness to ~20 mils, at which point it becomes constant. This trend can also be explained by considering the effect of fringing fields and change in ε_{eff} but from a different perspective. Thus, f_r of a circular loop is proportional to $(D_{ave}\sqrt{\varepsilon_{eff}})^{-1}$, where D_{ave} is the average diameter of the ring (and depends on the inner and outer diameters and effect of fringing fields on both diameters) [8]. The effect of fringing fields on the effective inner and outer diameters (i.e., related to D_{ave}) is equal and opposite, causing a net effect of zero on D_{ave} and subsequently no change to f_r. However, ε_{eff} does effect f_r. More specifically, considering each side of the loop as a microstrip line, as the substrate thickness increases to 20 mils (equal to the width of square loop), ε_{eff} reduces slowly [7]. After that, for thicknesses larger than the loop width, ε_{eff} does not change much. Thus, as shown in Figure 2a, f_r increases by reducing ε_{eff} up to 20 mils and then remains constant.

In Figure 2b, the effect of thickness on resonant depth is shown. For both designs, maximum resonant depth is achieved by using a thicker substrate for larger ε_r. This behavior can also be explained by considering Q_{rad}. That is to say, the energy stored in the substrate increases with increasing ε_r. Thus, Q_{rad} also increases, but Q_0 does not. In order to reach $Q_{rad} = Q_0$, the substrate thickness must be increased, thereby increasing Q_0. In addition, increasing substrate thickness decreases Q_{rad}. This occurs since P_{rad} and the stored energy increase with increasing thickness. However, the increase in P_{rad} is more significant

than that of the stored energy, resulting in an overall decrease in Q_{rad} [6]. Generally, there is a tradeoff between increasing ε_r and thickness, and the optimal substrate thickness is found when $Q_{rad} = Q_0$ (resulting in maximum resonant depth). Figure 2b also shows that the loop element achieves maximum resonant depth for a slightly thicker substrate (compared to the patch). This occurs since the loop element has less (effective) area and consequently has smaller Q_{rad}. Thus, a thicker substrate is needed to reduce Q_0 in order to maintain $Q_0 = Q_{rad}$. Figure 2c shows the effect of substrate thickness on the Q-factor. As shown, the Q-factor for both designs is finite for thicknesses with a related resonant depth (see Figure 2b) less than -10 dB.

To verify the simulation results, the waveguide simulator approach (WSA) [9] was used to measure $|\Gamma|$ of both unit cells when placed inside a standard rectangular waveguide, with the results included in Figure 3. Specifically, Figure 3a shows f_r as a function of substrate thickness which exhibits a similar behavior to that of Figure 2a (high loss material). The maximum resonant depth for the low loss dielectric occurs with a thinner substrate thickness (as compared to the high loss case of Figure 2b) as illustrated in Figure 3. This occurs since Q_0 is increased by the reduction in tanδ. Thus, in order to maintain $Q_0 = Q_{rad}$, Q_{rad} must increase. As discussed above, since Q_{rad} is inversely proportional to substrate thickness, a thinner substrate thickness is needed. Lastly, Figure 3c shows the Q-factor for the low loss substrate. The advantage of using a lower loss substrate is that a higher Q-factor is achieved (evident by comparing Figure 2c with Figure 3c), because the low loss substrate will store more and attenuate less energy at f_r. Specifically, the optimum case for both sensors is achieved for thicknesses less than ~ 80 mils for the low loss material. This differs from that of the high loss substrate, where optimal conditions are

achieved for a thicker substrate (see Figure 2c). Lastly, the simulated and measured results are in good agreement for f_r and resonant depth for both unit cells for substrate thicknesses of 15 mils and 32 mils. However, there are differences in the resonant depth and Q-factor of the loop element with a substrate thickness of 62 mils (attributed to a change in periodicity necessary for WSA measurements).

In order to illustrate how the performance metrics can be used to guide the design procedure rather than simply assess the performance of a given sensor, a flowchart is provided in Figure 5. As shown, first, the desired f_r and BW are defined. Then, the geometry of the unit cell should be chosen to provide a large or small Q_{rad}. Next, the unit cell must be modified if the resonant depth is less than -10 dB. Care must also be taken to ensure that the Q-factor is not deceptively large. For example, the loop element with a high loss substrate (ε_r of 4.3 and thickness of 90 mils) has a resonant depth of ~-11 dB (barely meeting the metric), but the BW is very narrow, causing the resulting large Q-factor (~50 in Figure 2c). This indicates the importance of assessing performance using resonant depth and Q-factor together. In addition, the minimum BW needed for an accurate measurement of a measureable resonant response depends on measurement parameters and application (equipment resolution, minimum measurement time, etc.). Therefore, the metrics proposed here provide a framework for sensor design, but the final sensor performance must be verified against application/measurement needs.

2.2. STRAIN SENSOR PERFORMANCE

It is also useful to see how the two sensor designs considered here perform in an actual sensing setting. Thus, simulations were conducted to see the effect of strain for both

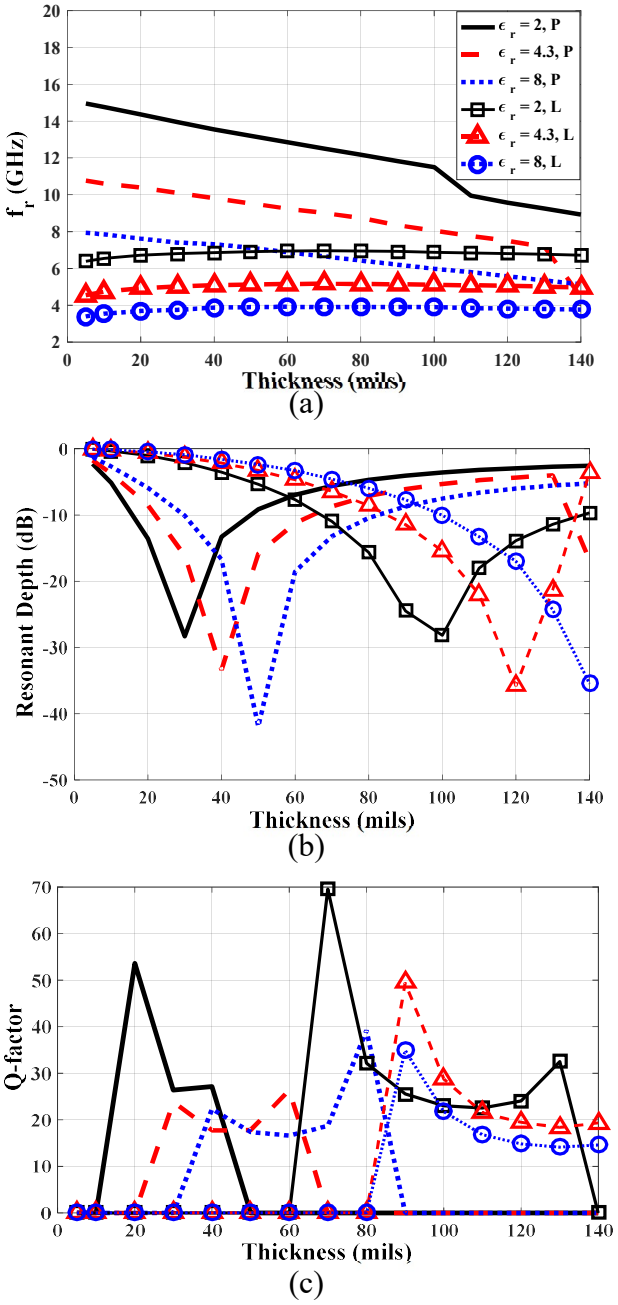

Figure 2. Performance metrics of FSS unit cells for a high loss substrate (P: patch, L: loop): (a) resonant frequency, (b) resonant depth, (c) Q-factor.

sensors on a substrate with $\varepsilon_r = 4.3$ and $\tan\delta = 0.09$, with ε_r equal to 2 and 8 also considered (to capture the effect of practical issues such as cracking and moisture ingress,

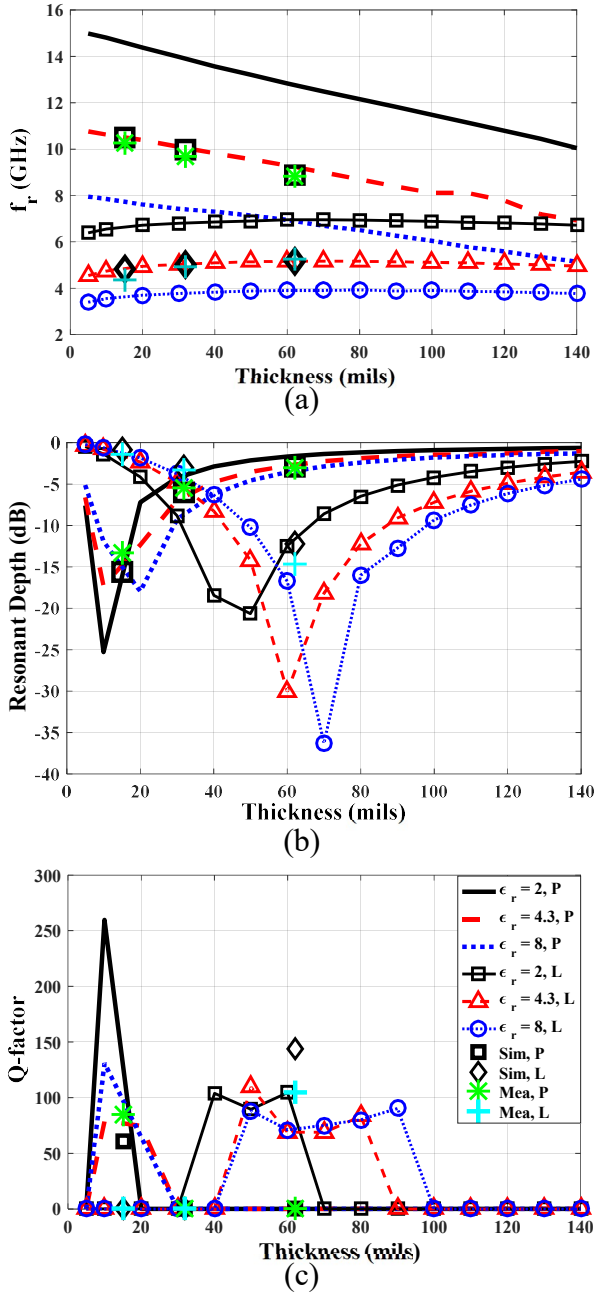

Figure 3. Measured and simulated performance metrics of FSS unit cells for a low loss substrate (P: patch, L: loop, Sim: simulation, Mea: measurement): (a) resonant frequency, (b) resonant depth, (c) Q-factor.

respectively). The substrate thickness is chosen to achieve maximum resonant depth (with an acceptable Q-factor) from Figure 2b (40 mils for the patch and 120 mils for the loop).

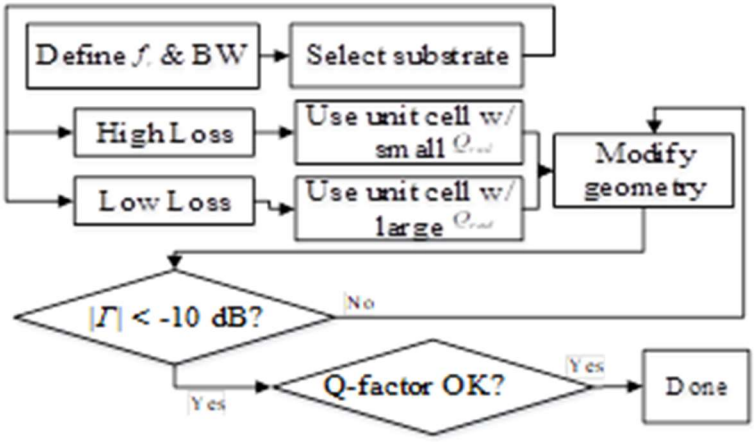

Figure 4. Flowchart for FSS sensor design procedure.

As discussed earlier, when ε_r increases, f_r is reduced. Also, when the strain increases, the dimensions of the unit cell will increase (in the direction of imposed strain), and subsequently f_r will decrease. In order to quantify these changes in f_r and obtain the sensitivity of each sensor, the change in f_r, Δf_r, is calculated as $\Delta f_r = | f_{r,NoStrain} - f_{r,WithStrain} | / f_{r,NoStrain}$, where $f_{r,NoStrain}$ is the resonant frequency without strain, and $f_{r,WithStrain}$ is the resonant frequency when the sensor is experiencing strain. As such, Δf_r for both sensors is shown in Figure 6.

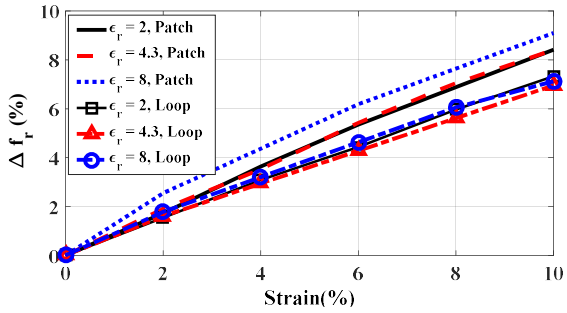

Figure 5. Comparison of the frequency shift between patch and loop.

The results in Figure 6 indicate a linear relationship between Δf_r and strain. The patch and loop-based sensors provide strain measurement sensitivity of 3.8% and 3% (respectively) for 4% strain. In [2], [3], where different sensor designs (cross dipole and grounded tripole) are used, strain sensitivity of 2.7% and 3% (for f_r), respectively, is achieved for the same strain. Therefore, by optimizing the design, improved sensing sensitivity can be achieved. In addition, for a given strain, changes in ε_r do not substantially affect the resultant Δf_r.

3. CONCLUSION

FSS-based sensors are ideal for structural health monitoring due their planar structure, ease of implementation, and remote interrogation. To this end, three performance metrics (resonant frequency, resonant depth, and quality factor) are proposed that can be used to guide and optimize FSS sensor design. These performance metrics have been applied to rectangular patch and loop-based sensors to quantify the effect of dielectric properties and thickness on sensor performance. The patch element performs better for thinner and high loss dielectric substrates. While the loop (for the same substrate) requires a thicker substrate for optimum performance. In addition, it is important to utilize resonant depth and Q-factor together when quantifying sensor performance. Lastly, the frequency shift of both sensors is largely independent of substrate permittivity, an important feature as it relates to practical measurement performance. The proposed metrics may be used in the future to quantify the effect of incident angle and surface waves on sensor performance.

REFERENCES

[1] Munk B A (2000), *Frequency Selective Surfaces Theory and Design*, NY: Wiley.

[2] Jang S, et al., (2012), "Frequency Selective Surface Based Passive Wireless Sensor for Structural Health Monitoring," *Smart Mater. and Struc.*, Vol. 22, No. 2.

[3] Kinzel E., (2014), "Design of a Frequency-Selective Surface strain sensor," *IEEEAntennas and Propag. Society International Symposium (APSURSI),* pp. 2074-2075.

[4] Pieper D F, Donnell K M (2015), "Application of Frequency Selective Surfaces for Inspection of Layered Structures," *Instrumentation and Measur. Tech. Conference (I2MTC), 2015 IEEE International.*

[5] Martin G, Skorobogatiy M (2013), "Terahertz Multiparameter Sensor using Fiber-Interrogated Frequency Selective Surface," *arXiv* preprint arXiv:1311.6390.

[6] Karnati Kalyan K, et al. (2013), "Theoretical analysis on reflection properties of reflectarray unit cells using quality factors," *IEEE Trans. on Antennas and Propag.,* Vol. 61, No. 1, pp. 201-210.

[7] Balanis, C A (2012), *Advanced Engineering Electromagnetics*, 2nd ed., John Wiley & Sons.

[8] Vourch C J, and Timothy D D (2014), "Analytical and full-wave analysis of square and ring patch structures for reflectarray unit cells," *Antennas and Propag. (EuCAP), 8th European Conference on*. IEEE, pp. 1925-192.

[9] Hannan P, and Balfour M (1965), "Simulation of a Phased-Array Antenna in Waveguide," *IEEE Transactions on Antennas and Propagation* Vol13, No. 3, pp. 342-353.

III. AN APERTURE EFFICIENCY APPROACH FOR OPTIMIZATION OF FSS-BASED SENSOR RESOLUTION

ABSTRACT

Frequency selective surfaces are periodic arrays of conductive elements, and when illuminated by electromagnetic energy, have a specific frequency response. FSS-based sensing is a relatively new application of FSSs, and such sensors have shown promise for crack detection and strain sensing, amongst others. Generally, when an FSS sensor is illuminated in full, the response of the sensor is related to the entire FSS landscape. In this way, the resolution of the sensor is equal to the FSS dimensions. However, this limits localized sensing. As such, to improve the achievable resolution, the sensor must be illuminated locally in order for the response to be related to a specific region of the sensor. Under this approach, an FSS sensor is considered to consist of many sensor cells. Therefore, to quantify the sensor cell efficiency in terms of the illuminating footprint in order to obtain the optimum sensor cell size, an analysis approach based on reflectarray aperture efficiency is used. As such, by maximizing the sensor cell efficiency, an optimum sensor cell size can be determined for a given illuminating footprint. This approach is applied to a grounded square loop-based FSS sensor, with simulation and measurement results provided. The results indicate that optimal sensor cell dimensions can be determined where the total efficiency of a given footprint is maximized. To support this, three different sensor cells are considered with the same maximum total efficiency, of which the smallest sensor cell gives the highest resolution of ~3 cm × 3 cm.

1. INTRODUCTION AND BACKGROUND

Frequency selective surfaces are periodic arrays of conductive elements located on a dielectric substrate, and when illuminated by electromagnetic energy, have a specific transmissive or reflective frequency response. This frequency response is dependent upon inter-element spacing, element geometry, substrate properties (dielectric properties and thickness) and the local environment [1]. There are numerous (traditional) applications of FSSs including filters [2], absorbers [3], [4], radomes [4], [5], reflectors and lenses [6]. More recently, FSSs have also shown potential as sensors for structural health monitoring (SHM) [7]-[13]. Their ease of implementation, planar structure, and wireless interrogation make such sensors ideal for SHM. For example, FSS-based sensing has recently been utilized for crack detection [7]. In this case, the presence of a crack causes a shift in the resonant frequency of the FSS. Similarly, in [8], normal and shear strain sensing are achieved by monitoring the reflection response of an FSS sensor. In [9], an FSS is used as an embedded sensor on a concrete/composite column for detection of strain and buckling during displacement load testing. FSS-based sensing has also found application for concurrent temperature and strain sensing [10], and detection of delaminations/disbonds within layered structures [11]. Also, the addition of active components to FSS sensors can improve the sensitivity of the sensor to environmental noise by modulating the frequency response [12]. In this way, the modulated FSS response can be easily delineated from other signals that may be present. The particular sensor design of [12] also included the potential for energy harvesting (to power the active elements). FSS sensors have also been utilized in the terahertz regime for chemical and biochemical sensing (i.e., humidity changes and

paper thickness) [13]. Metamaterials (structures similar in design and illumination to FSSs) have also found application in the sensing regime, including a telemetric strain sensor based on a split-ring-resonator [14].

As mentioned, FSSs can be designed to operate in reflection [9, 11] or transmission mode [7], [14]. From a practical point of view, FSS sensors operating in reflection mode (in general designed with a conductive backing to the substrate) [11] are desirable from a sensing perspective, as they require a one-sided interrogation (as opposed to needing access to both sides of a structure to perform transmission based measurements). It is also beneficial to utilize a reflection-based sensor from a signal detection point-of-view, as the sensor response may be attenuated by the structure under test if two-sided measurements are performed. The addition of a conductor backing to the sensor also prevents the material properties of the structure under test from affecting the sensor response [15].

In the theory, the response of an FSS is analyzed assuming infinite dimensions, an infinite number of unit cells (where the unit cell includes element shape, dimensions, and inter-element spacing), with a uniform plane wave excitation. However, in practice, an FSS has a finite number of unit cells and is illuminated with a spatially-varying electric field pattern from an antenna (for example, a horn antenna). As such, there are three factors that cause a deviation in the finite FSS's response from that of the ideal case: 1) the non-uniform excitation, 2) the effect of edges (truncation from an infinite array), and 3) the number of FSS unit cells within the FSS [16]. As such, the effect of the number of unit cells and non-uniform excitation are studied explicitly in this work with the goal of optimized sensor resolution. Edge effects are considered as part of the background effects, as is discussed below in Section 3.

The issue of a non-uniform excitation and the corresponding illumination pattern is particularly important as it relates to localized sensing. More specifically, when an FSS is interrogated with an illumination pattern that covers the entire FSS, the frequency response is affected by all FSS unit cells. As such, it is impossible to locate where, within the FSS dimensions, a change occurred. Therefore, in order to achieve a sensor resolution smaller than the dimensions of the (entire) FSS, the excitation must be adjusted accordingly. In other words, to monitor an FSS sensor locally, the FSS must be illuminated locally. In this way, the frequency response due to specific locations within the FSS landscape can be detected and changes attributed to these localized areas. For example, in [17], the ability of an FSS sensor to detect localized changes (i.e., the presence of damage within a unit cell) is studied by illuminating the sensor locally with a horn antenna (which was physically scanned over the entire FSS). However, since the step size of the scan (essentially the varying position of the horn) is smaller than the beamwidth of the antenna, the frequency response due to each illuminated area "overlaps", rendering a low measurement resolution and ultimately a large area is determined to contain the detected damage. To overcome this issue, an FSS sensor can be considered as an array of sub-FSS (or sensor) cells, with each cell illuminated independently. In this way, localized sensing and subsequent improved sensor resolution can be accomplished. Hence, it is important to study the effect of illumination pattern and sensor cell dimensions on the sensor cell response in order to determine the optimum achievable resolution per application needs. To this end, this work expands upon the preliminary investigation published in [18] by determining the optimum sensor cell size by applying a modified version of the reflectarray aperture efficiency analysis of [20].

2. SENSOR CELL EFFICIENCY

As mentioned, the dimensions of the illuminating pattern on the FSS sensor (herein referred to as the footprint) play a role the resolution of the sensor. To this end, in [18], the footprint was defined as the dimensional area within which 75% of the incident energy (or 6 dB variation in electric field) was contained. Under this definition, 25% of the incident energy excites the sensor outside the footprint (and hence the sensor cell) of interest, and as such, may also affect the response of a given cell. To this end, to better quantify the effect of the illuminating footprint on the performance of an FSS sensor, an FSS can be considered similar to a reflectarray since both are planar arrays that are remotely illuminated. It is well known that the aperture efficiency of a reflector antenna is related to the aperture size, its distance from the illuminating source (focal length), and the pattern of the illuminating source [19]. In other words, the aperture efficiency is dependent upon the illumination pattern for a fixed aperture. Hence, a similar approach, based on the aperture efficiency analysis of reflectarray antennas [20], can be applied to FSS sensors in order to quantify the optimum sensor cell size in terms of illumination footprint. In particular, the sensor cell efficiency, η_{sc}, is studied to obtain the resolution (e.g., sensor cell size) of the sensor analytically in terms of a given illumination pattern.

For the case of reflectarrays, the aperture efficiency of a reflector antenna is affected by the ratio of focal length (h) to the diameter of the aperture (D) [20], as shown in Figure 1a. Therefore, to apply this approach to FSS sensors, the sensor cell dimensions are considered as the aperture dimensions for this analysis. In this way, η_{sc} is defined as the product of 1) the illumination efficiency, η_{ill}, which is related to the non-uniform electric

field across illumination footprint on the sensor, and 2) the spill-over efficiency, η_s, which is defined as the ratio of the amount of energy that illuminates the sensor cell to the total amount of radiated energy from the illuminating source [20]. To expand this approach for FSS-based sensing, only the non-uniformity of the illumination footprint is considered in the modified (from [20]) definition of $\eta_{ill,}$ (whereas in [20], the element factor of the reflectarray is included as part of the total electric field across the aperture). Additionally, the illumination footprint (i.e., antenna pattern) is considered to be represented by $cos^q\theta$ (which can be used to model the radiation intensity of a horn antenna for an elevation angle of θ). In this way, increasing q represents a more directive pattern. Therefore, using this illumination pattern model (i.e., $cos^q\theta$) and considering a linear polarization (here, in the x-direction as shown Figure 1a), a modified illumination efficiency and (equal to that of [20]) spill-over efficiency are given as:

$$\eta_{ill} = \frac{\left[\left(\frac{1-\cos^{q}\theta_e}{q}\right)+\left(\frac{1-\cos^{q-1}\theta_e}{q-1}\right)\right]^2}{2\tan^2\theta_e\left[\left(1-\cos^{2q+1}\theta_e\right)/\left(2q+1\right)\right]} \tag{1}$$

$$\eta_S = 1-\cos^{2q+1}\theta_e \tag{2}$$

where θ_e is half of the subtend angle from the illuminating source to the aperture ($tan\theta_e = SC/2h$, where SC is the sensor cell length) as shown in Figure 1a. Since this approach is modified from [20] (which focused on reflectarrays), the given equations are for a circular aperture. Therefore, since the sensor cells considered here are dimensionally square (sized in this way due to the square nature of the unit cell), a sensor cell with a length of SC, as shown in Figure 1b, is represented by an equivalent circular area with a diameter, D, of $2 \times SC/\sqrt{\pi}$ (see Figure 1a).

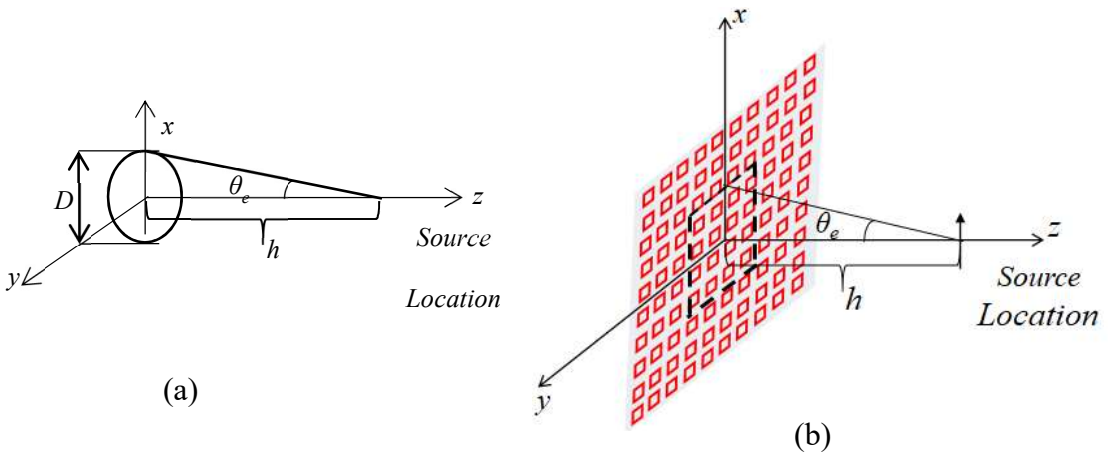

Figure 1. The schematic of aperture and illuminating source geometry for (a) a reflector antenna, (b) an FSS sensor.

From (2), it can be seen that η_s increases with θ_e. Additionally and per (1), as θ_e increases, η_{ill} reduces and hence these two efficiencies have complementary behavior with respect to each other [20]. Hence, the maximum η_{sc} occurs when the product of η_{ill} and η_s is maximum (which may not be when η_{ill} or η_s is maximum). To this end, in Figure 2, the efficiencies are shown in terms of q (for a $cos^q\theta$ radiation pattern) for θ_e from 15º to 30º with step size of 5º. In this way, a range of illuminating footprints incident on the aperture (i.e. FSS sensor) are represented. The complementary behavior can be seen since η_{ill} decreases and η_s increases with θ_e. Additionally, an increase in q means the pattern becomes more directive, meaning the electric fields on the sensor cell has more variation from the center to the edge of the sensor cell. In this way, the electric fields are less uniform and hence η_{ill} reduces. On the other hand, for a given sensor cell size, by increasing q, most of the incident energy is contained within the desired sensor cell. As such, the spill-over energy (incident outside the sensor cell) reduces which improves η_s. Also and as seen in Figure 2a, when θ_e increases, η_s increases for a fixed q (i.e., a specific illumination pattern).

For a fixed q, increasing θ_e represents an increase in footprint size. Hence, increasing the footprint size for a given pattern decreases the uniformity of the electric field over the footprint dimensions. Also in this case, a larger portion of radiated energy from the illuminating source is contained within the footprint and less energy is incident outside it. Therefore, η_{ill} reduces as θ_e increases (for a fixed q/pattern), while η_s increases.

Using η_{ill} and η_s of Figure 2a, η_{sc} is calculated and shown in Figure 2b. It can be seen that a smaller θ_e causes a higher maximum efficiency when q (in $cos^q\theta$) is large (i.e. q greater than ~30 or a more directive pattern). This is due to the fact that the illuminating footprint is more uniform and directive for large q and small θ_e. Hence, the footprint is "focused" and the illumination efficiency dominates in η_{sc} (since η_s approaches 100% as shown in Figure 2a). It can also be seen that the maximum values for η_{sc} are not equivalent as a function of θ_e. This is because for smaller values of q, the footprint is less directive and hence a larger θ_e is needed in order to achieve a greater η_s (i.e., less spillover energy). Hence, for small q and large θ_e, η_s dominates the overall η_{sc}.

3. SIMULATION RESULTS

In order to study the sensor cell efficiency of an FSS sensor, full-wave electromagnetic simulations were conducted using CST Microwave Studio© (frequency domain solver) considering a grounded square loop design. To begin, the ideal FSS sensor response is simulated using periodic boundary conditions (to create an infinite array of unit cells) with a uniform plane wave excitation. The unit cell, along with the reflection response, $|S_{11}|$, of the FSS are shown in Figure 3. This FSS is designed to resonate at 10

GHz (see Figure 3b) with design parameters of D = 10mm, a = 4.95 mm, w = 0.4 mm on an FR-4 substrate with a thickness of t = 32 mils.

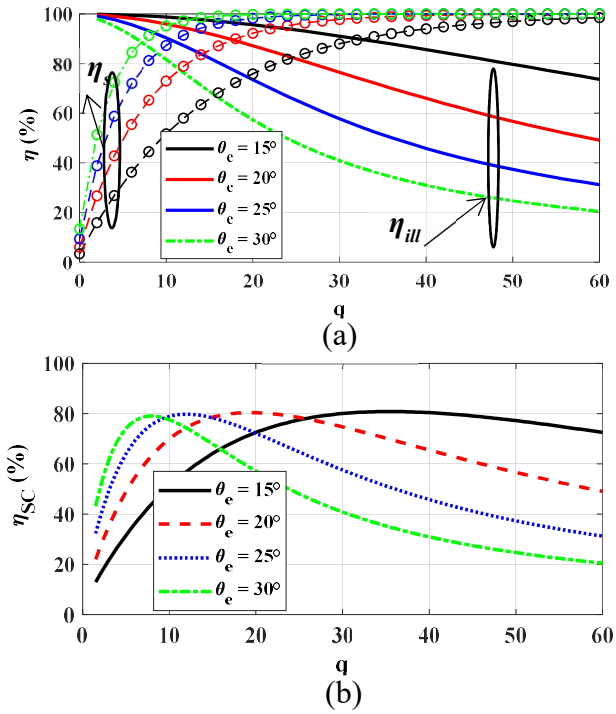

Figure 2. (a) η_{ill} and η_S versus q (b) η_{sc} versus q for different θ_e.

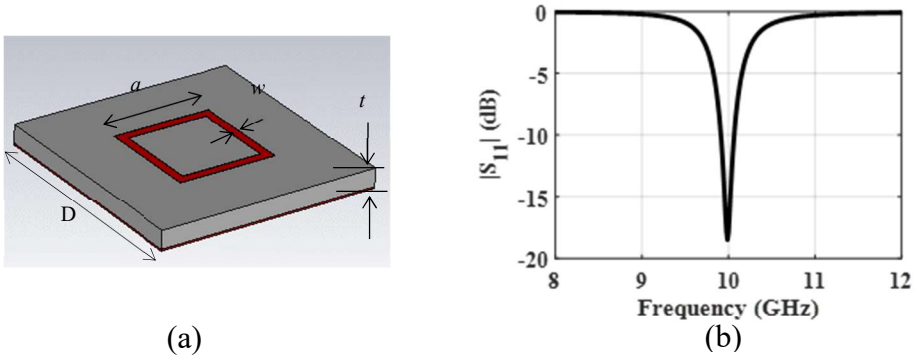

Figure 3. (a) Unit cell schematic, and (b) $|S_{11}|$ of the ideal FSS.

To illuminate the FSS, an X-band (8.2 – 12.4 GHz) pyramidal horn antenna is considered as the illuminating source. The simulated magnitude of the reflection coefficient ($|S_{11}|$) of this antenna radiating into free space is shown in Figure 4 (used later for normalization purposes), along with a photograph of the horn antenna modeled here and used later for measurements. The dimensions of the horn antenna aperture (shown in Figure 4b) are a = 67 mm and b = 56 mm, and the length of the flared section is 92.8 mm.

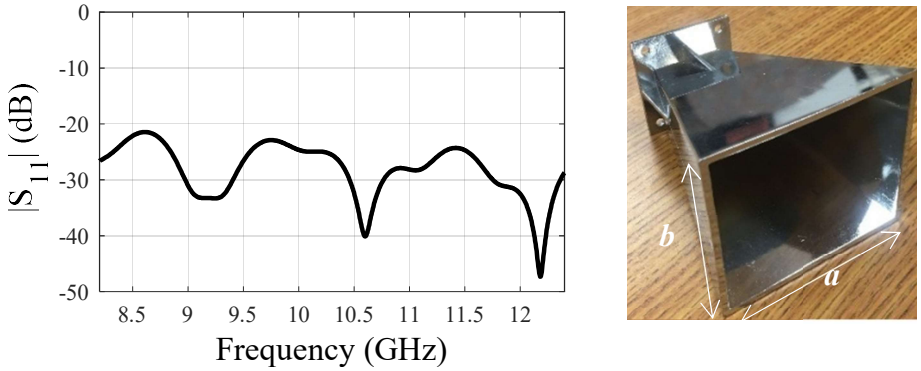

(a) (b)

Figure 4. Simulated $|S_{11}|$ of the horn radiating into free space (a), and photograph of the horn antenna (b).

In order to verify that the approach used in (1) and (2) is valid for any field pattern within all regions of the horn antenna considered here, field patterns at distances of $1\lambda_0$, $5\lambda_0$, and $10\lambda_0$ (near field, radiating near field, and beginning of far field, respectively) from the horn aperture were simulated in Ansys HFSS© and compared with far field patterns from Ansys HFSS© and CST©, with the results shown in Figure 5. . As can be seen, all patterns have similar distributions (in the main lobe) as $cos^{13.5}\theta$. Therefore, the radiation

intensity of the horn antenna is modeled as $cos^{13.5}\theta$ in order to calculate the efficiencies, as shown in Figure 6 as a function of θ. As seen, the maximum η_{sc}, of 80% occurs for θ_e = 25°.

As discussed earlier, it is important to obtain an optimal illumination footprint where the η_{sc} is maximum in order to have less spill-over energy outside of the sensor cell and more uniformity in electric field across the sensor cell. To illustrate this, three different sensor cell sizes are considered with dimensions of $1\lambda_0 \times 1\lambda_0$ (3×3 unit cells), $1.67\lambda_0 \times 1.67\lambda_0$ (5×5 unit cells) and $3.34\lambda_0 \times 3.34\lambda_0$ (10×10 unit cells). As mentioned and shown in Figure 1, θ_e represents the illuminating footprint size. Hence, to achieve the optimal footprint for a given sensor cell using the horn antenna of Figure 4, the optimal distance (h_{opt}) between the horn antenna and the sensor cell can be determined where η_{sc} is maximum (since the electric field distribution is different at different distances from the aperture). Therefore, the efficiencies shown in Figure 6, which are in terms of θ_e, can be converted to in terms of h. Hence, h_{opt} can be determined in order to find the optimal footprint for maximum η_{sc}, as shown in Figure 7 (h_{opt} is indicated for the largest cell).

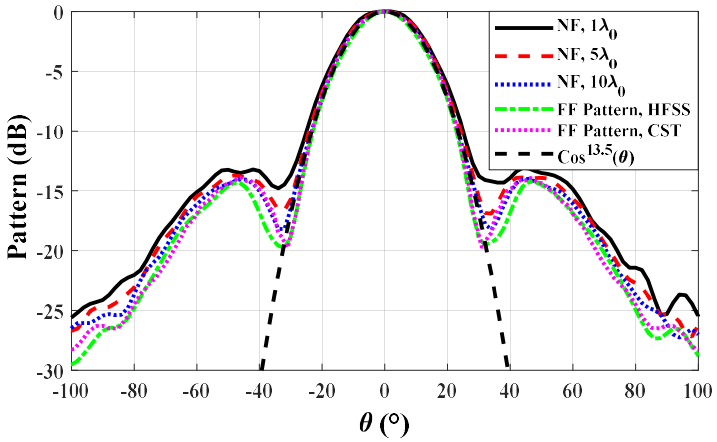

Figure 5. $Cos^q\theta$ pattern for q = 13 in comparison with pattern of horn antenna.

As seen in Figure 7, as h increases, η_{ill} increases. This indicates that the non-uniformity of the electric fields over the footprint reduces. In other words, for a fixed footprint (or a specific h), a smaller sensor cell experiences less variation in the incident electric field and hence a larger η_{ill} is achieved (as shown). Further, as the sensor cell size increases, η_{ill} reduces for a fixed illumination footprint for distances smaller than a few λ_0 (Figure 7a). However, as h exceeds a few λ_0, η_{ill} becomes constant and hence insensitive to h since the electric field distribution begins to approximate that of the far field region and hence becomes more uniform, as illustrated in Figure 8 (shown over an area of 100 mm × 100 mm). On the other hand, with regards to η_s, for a given sensor cell size, as h increases, more energy spills outside of the sensor cell. This causes a reduction in η_s, as is evident in Figure 7a. Since η_{ill} and η_s are complementary to each other, h_{opt} (indicated in Figure 7b) occurs when the product of η_{ill} and η_s (or η_{sc}) is maximum. Otherwise, for other values of h: 1) when $h<h_{opt}$, there is significant variation in the electric field across the sensor cell (i.e., low η_{ill}), or 2) $h>h_{opt}$ and there is large spill-over energy outside of the sensor cell (i.e., low η_s). Hence, it is important to select an optimum h to avoid unnecessary non-uniformity or spill-over. To this end, in Figure 7b, it can be seen that, the optimum h for a sensor cell size with dimensions of $1\lambda_0 \times 1\lambda_0$, $1.67\lambda_0 \times 1.67\lambda_0$, and $3.34\lambda_0 \times 3.34\lambda_0$, is $1.33\lambda_0$, $2.2\ \lambda_0$, and $4.43\ \lambda_0$, respectively.

3.1. APPLICATION OF SENSOR CELL EFFICIENCY

As discussed earlier, localized illumination (and the concept of sensor cells) can be used to improve the resolution of FSS-based sensors in order to achieve a distributed sensing map of an area of interest. As such, three different sensor cells are selected

(commensurate with those of Figure 7). Specifically, FSS sensors with 3×3 (30×30 mm^2 or $1\lambda_0 \times 1\lambda_0$), 5×5 (50×50 mm^2 or $1.67\lambda_0 \times 1.67\lambda_0$), and 10×10 (100×100 mm^2 or $3.34\lambda_0 \times 3.34\lambda_0$) unit cells are considered with an illuminating source of the horn antenna of Figure b.

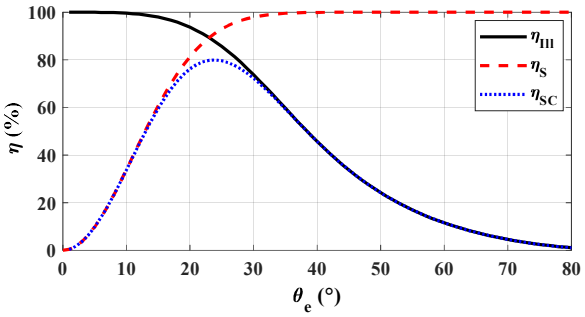

Figure 6. Efficiencies in terms of θ_e for pattern of $cos^{13.5}\theta$.

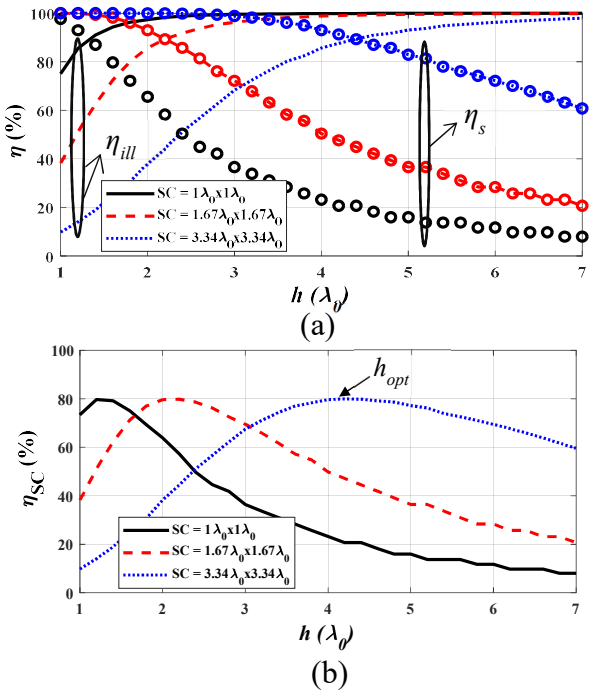

Figure 7. Efficiencies vs. distance for different sensor cell sizes (a) illumination and spill-over efficiencies, (b) sensor cell efficiency.

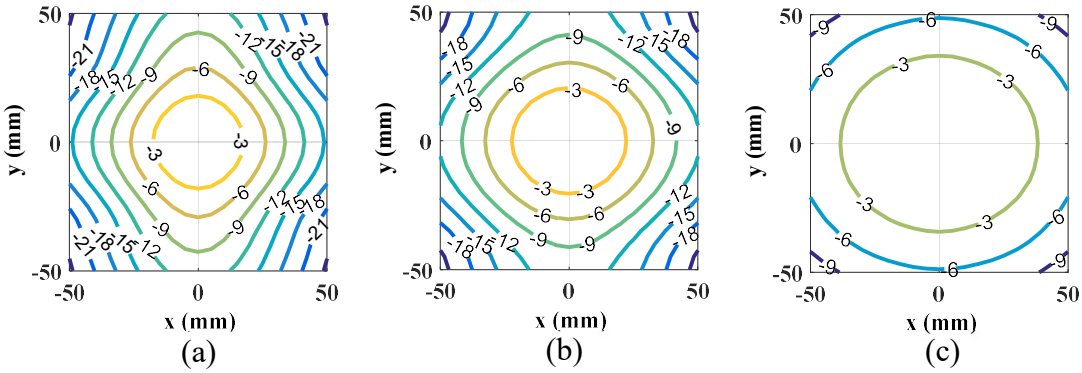

Figure 8. Illumination pattern for (a) $h = 1.33\lambda_0$, (b) $h = 2.2\lambda_0$, and (c) $h = 4.43\lambda_0$.

Since the footprint (i.e. radiation pattern from the antenna) can only be adjusted (in this case) by changing the distance between the horn antenna and sensor, three distances from illumination source to the sensor are considered in order to capture three different illuminating footprints; namely, $h = 1.33\lambda_0$, $2.2\lambda_0$ and $4.43\lambda_0$. The illumination footprints will be herein be referred to as high variation (HV), medium variation (MV), and low variation (LV), respectively, and are shown across the sensor area of 100 mm×100 mm in Figure. 8. These distances to achieve specific footprints are selected from Figure. 7 for the maximum η_{sc}. As discussed earlier, for each footprint (i.e., value of h), the optimum sensor cell size can be determined by obtaining the optimum illumination footprint (i.e., when η_{sc} is maximized). Similarly, for a given cell size, one of the illuminations of Figure. 8 will result in improved sensor cell performance over than other two. In other words, for each footprint of Figure 8 one footprint will have a maximum η_{sc}, while the two other footprints will have a smaller η_{sc} due either low η_s or low $\eta_{ill.}$ To better illustrate this, Figure 9 shows the efficiencies for each sensor cell size for the footprints of Figure 8.

As seen in Figure 9a, the smallest sensor cell ($1\lambda_0 \times 1\lambda_0$) has a maximum η_{sc} for the HV footprint (HVF). Further, as the footprint changes from HV to LV, the sensor cell size

is smaller than the optimal sensor cell size for the MV and LV footprints. Hence, η_{ill} increases since the variation in footprint reduces and results in increased uniformity across the sensor cell. Conversely, η_s reduces because the sensor cell is small and more energy will be incident outside the cell.

As shown in Figure 9b (sensor cell of $1.67\lambda_0 \times 1.67\lambda_0$), an η_{sc} occurs for the MVF ($h = 2.2\lambda_0$). For the HVF ($h = 1.33\lambda_0$), η_s approaches 100%. This indicates that the sensor cell is large enough to capture all incident energy (no spill-over energy outside of the sensor cell). However, the uniformity of the incident electric field decreases and hence η_{ill} reduces. On the other hand, the LVF ($h = 4.43\lambda_0$) provided more uniformity across the sensor cell but at the cost of an increase in spill-over energy since the optimal sensor cell size for the LVF is larger than the sensor cell considered.

Lastly, for the largest sensor cell size ($3.34\lambda_0 \times 3.34\lambda_0$), shown Figure 9c, a maximum η_{sc} occurs for the LVF ($h = 4.43\lambda_0$). A reduction in h (or more variation in footprint, i.e. MVF or HVF) will increase the non-uniformity of the electric field across the sensor cell and consequently reduce η_{ill}. In addition, since the size of sensor cell is larger than the optimal footprint for HVF and MVF, all of the energy is incident on the sensor and hence η_s approaches 100%.

3.2. FREQUENCY RESPONSE OF SENSOR CELLS

As mentioned earlier, the FSS sensor can be considered as consisting of many sensor cells and the sensor cell dimensions can be adjusted through adjustment of the footprint size. To this end and to isolate the effect of footprint dimensions on the sensor response, three individual sensors are considered with dimensions equal to the cells

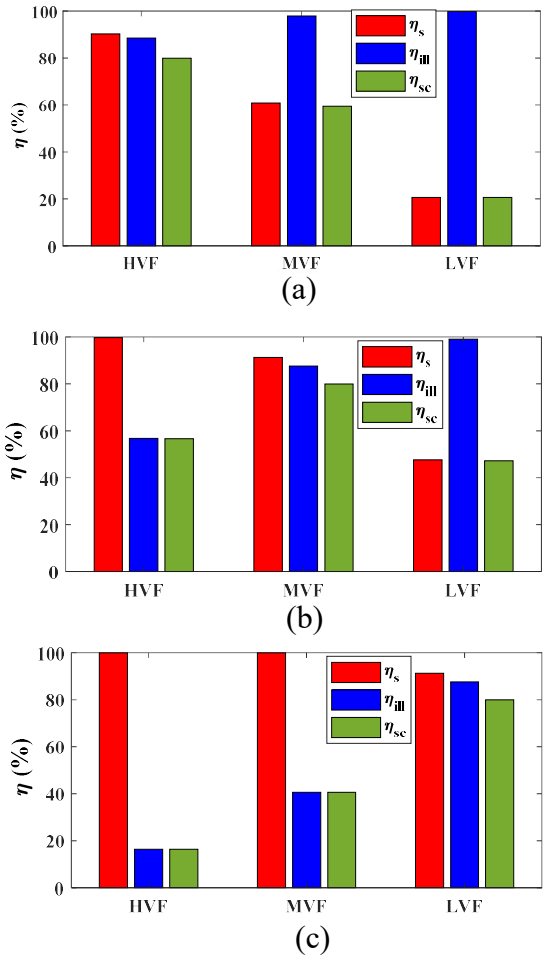

Figure 9. Efficiencies of sensor cells when illuminated with different footprints for sensor cells with dimensions of (a) $1\lambda_0 \times 1\lambda_0$, (b) $1.67\lambda_0 \times 1.67\lambda_0$, and (c) $3.34\lambda_0 \times 3.34\lambda_0$.

considered above and their response analyzed in terms of η_s and η_{ill}. This approach of utilizing only one cell is particularly important when the illuminating footprint is larger than the cell. In other words, if adjacent cells are present, the partial illumination of these adjacent cells may contribute to the detected frequency response. Therefore, to see the effect of a large spill-over, the size of the sensor is considered equal to that of a sensor cell.

In order to isolate the frequency response of a finite FSS from other environmental reflections resulting from the illumination antenna aperture and local environment, the free

space frequency response of the antenna (radiating into the environment within which the sensor resides) is necessary and therefore simulated. In this way, all environmental reflections can be coherently removed from the FSS response in order to obtain the normalized signal from FSS or the signal of interest (i.e. the response from the FSS specifically, or S_{11}), as:

$$|S_{11}| = |S_{11,\text{WholeStructure}} - S_{11,\text{FreeSpace}}| \quad (3)$$

where $S_{11,\text{WholeStructure}}$ is the total signal with the FSS present, and $S_{11,\text{FreeSpace}}$ is the signal when the illuminating source is radiating into free space (Figure 4a).

The simulations of finite FSS sensor cells (dimensions as above) with the horn antenna illumination shown in Figure 8 were conducted using the time domain solver in CST Microwave Studio©. The sensor cells are chosen as above and are illuminated by HVF, MVF, and LVF. The resulting frequency responses are normalized per (3) and shown in Figure 10. As discussed earlier in detail, the relative sensor cell and footprint size affects the sensor cell efficiencies. Hence, the frequency response of sensor cells for different footprints can be categorized in three cases as follows:

1. *The optimum illumination footprint is smaller than the sensor cell size and* $\eta_{ill} < \eta_s$*;*
2. *The optimum illumination footprint is equal to the sensor cell size and* η_{sc} *is maximum; and*
3. *The optimum illumination footprint is larger than the sensor cell size and* $\eta_{ill} > \eta_s$*.*

As seen in Figure 10a, for Case 1 where $\eta_{ill} < \eta_s$, the frequency response of the sensor cells with 5×5 and 10×10 unit cells and a HVF are very similar. This similarity occurs since the number of illuminated unit cells are the same (limited by the HVF), even though the size of sensor cell increases. However, when the illumination footprint changes

to MVF for the sensor cell with 10×10 unit cells, the frequency response shows a slightly larger resonant frequency and depth. This is due to illuminating more unit cells within the sensor cell (i.e., a wider footprint).

This behavior differs in Figure 10b, where the optimum sensor cell efficiency (η_{sc}) is achieved (Case 2). That is to say, even though the sensor cell efficiency is optimized for all three sensors considered, the resonant frequency for the sensor cell with 3×3 unit cells is slightly less than that of the other two (which are near the ideal response of 10 GHz). This is due to the fact that the number of unit cells (3×3) on the sensor cell is not sufficient to achieve optimum (i.e., ideal) FSS behavior, whereas the other two sensors are converging (at 9.91 GHz) to the ideal resonant frequency of 10 GHz.

The results for Case 3, when $\eta_{ill} > \eta_s$, are shown in Figure 10c. Here, the illumination footprint is very uniform but the illuminating energy "spills outside" of the sensor cell. For example, for the 3×3 sensor cell, when illuminated by the LVF, the frequency response is ~10 dB less than the other two scenarios considered. This is due to an increase in spillover energy since the sensor cell size is much smaller than the footprint. More specifically, in this case, the area encompassed by the sensor cell is only 9% of the area illuminated by the footprint, and as such, a low amount of signal return less energy is reflected back to the antenna by the sensor. However, the illumination uniformity is high and therefore the sensor cell properly resonates. For the other two sensor cells, the slight decrease in resonant frequency is attributed to the increase in footprint variation. When the same sensor is illuminated by an MVF (which is larger than the sensor cell size), the frequency response is improved regarding the signal level and resonates at 9.88 GHz. Similarly, the sensor cell

with 5×5 unit cells when illuminated by a larger footprint (here, LVF) than its size, the sensor cell resonates at 9.89 GHz.

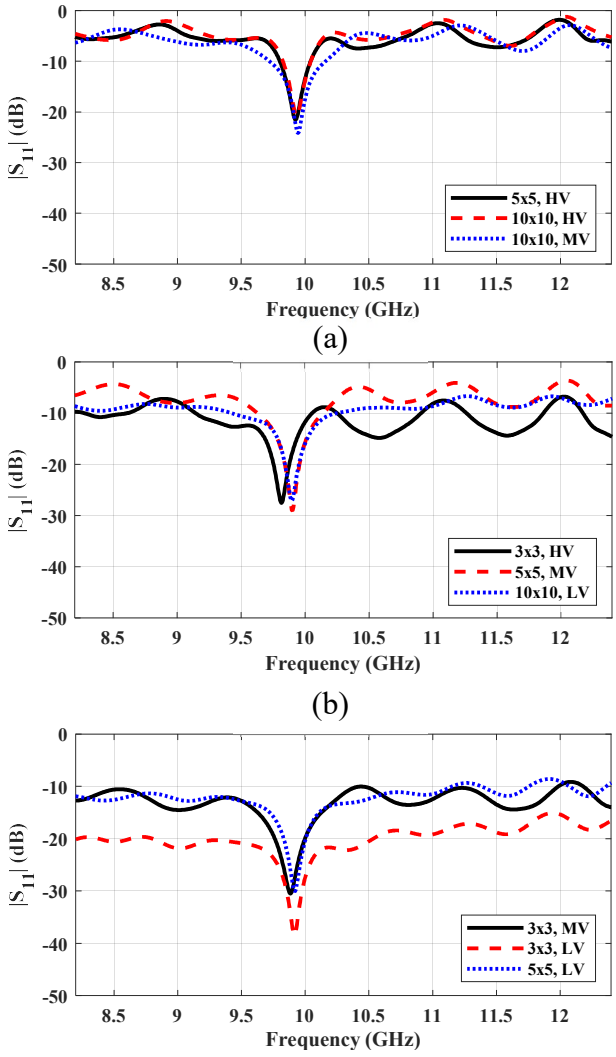

Figure 10. Simulated $|S_{11}|$ of three different FSS sensors when (a) $\eta_s > \eta_{ill}$, (b) max η_{SC}, and (c) $\eta_s < \eta_{ill}$.

4. MEASUREMENT RESULTS

To apply the modified efficiency approach developed above and verify the simulation results, FSS sensors (of the same dimensions as above) with 3×3, 5×5 and 10×10 unit cells were fabricated, as shown in Figure 11. The S_{11} from each was measured by connecting a source (horn antenna) to a calibrated port of an Agilent 8510C vector network analyzer and placed such that the illumination patterns of Figure 8 were achieved. The measurements were performed on 5 sensors of each size, with the average $|S_{11}|$ shown in Figure 12 in terms of the efficiencies (as was done for the simulated results of Figure 10). In addition, the normalization procedure of (3) is utilized with the measured results (including that of the horn radiating into freespace) to remove the effect of the background.

It can be seen in Figure 12a that when the optimum illumination footprint is smaller than the sensor cell size and hence $\eta_{ill} < \eta_{s,}$ (Case 1), the frequency response is in agreement with simulation. However, the resonant depth is larger which is attributed to measurement anomaly, as resonant depth (both simulated and measured) is challenging to capture precisely, especially in highly resonant cases. In Figure 12b (Case 2), the results of the sensor cells when illuminated by an optimum illumination footprint (and hence η_{sc} is maximum,) is shown. When comparing these results with the simulated results of Figure 10b, there is good agreement between the 5×5 and 10×10 unit cells. The minor increase in resonant frequency between the measured and simulated result for the 3×3 unit cell sensor is attributed to measurement error. Lastly, for the results of Figure 12c, where the illumination footprint is larger than the sensor cell size and $\eta_{ill} < \eta_s$ (Case 3), the measured results are also in good agreement with the simulation results.

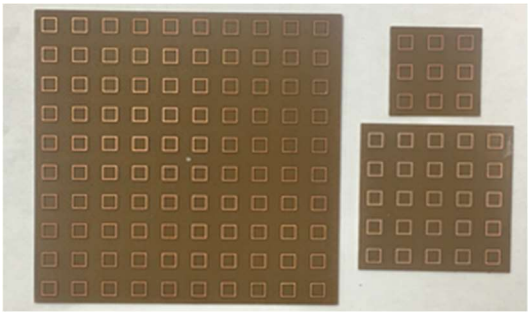

Figure 11. Photograph of the FSS sensors.

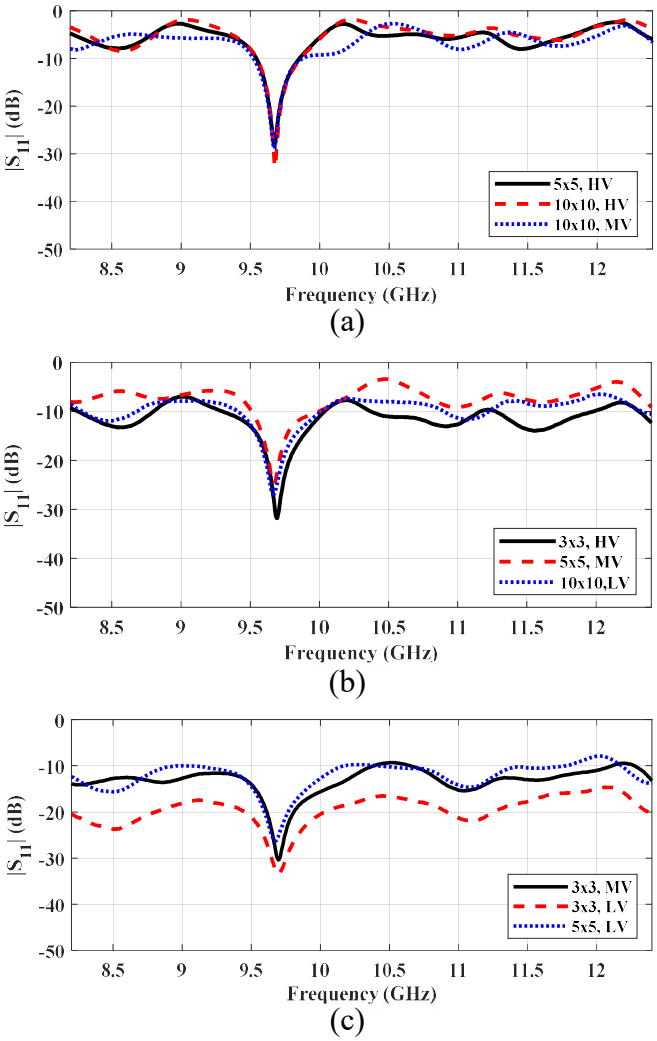

Figure 12. Measured $|S_{11}|$ of three different FSS sensors when (a) $\eta_s < \eta_{ill}$, (b) max η_{SC}, and (c) $\eta_s > \eta_{ill}$.

Further measurements were performed on a sensor containing 15×20 unit cells (with a photograph of the sensor shown in Figure 13). This sensor contains a small area (3×3 unit cells) within which the unit cell dimensions have been increased by 5% along the *y*-direction in order to model the effect of unidirectional localized strain. This area is indicated by a red square in Figure 13. To this end, measurements were performed using the three illumination footprints of Figure 8 where the footprints illuminate 3×3, 5×5 and 10×10 unit cells, respectively. Moreover, to illustrate the localized sensing capability, measurements were performed when the antenna is in line with the strained area of the sensor and offset (in the negative *x*-direction). The sensor response is shown in Figure 14. As can be seen in Figure 14a, the sensor response, when directly illuminated by an HVF (~3×3 unit cell footprint), the frequency response shows a resonant frequency of 9.51 GHz. When the illuminating antenna is moved off-center, the frequency response resonates at 9.61 GHz and does not change. This indicates that the strained area is not detected. This is as expected as it is not contained within the footprint. The sensor response for a MVF (~5×5 unit cell footprint) shows a similar (to Figure 14a) behavior, as is illustrated in Figure 14b. In this case, when the source is offset by 35 mm, the illumination still illuminates a few strained elements. However, the frequency response is dominated by the unstrained elements and the received power near the edge of the footprint (i.e., location of the strained elements) is ~ 6dB less than that of the center of footprint (see Figure 8b). Therefore, the effect of the strained elements is minimal and the frequency response is similar to those farther than 35 mm from the strained.

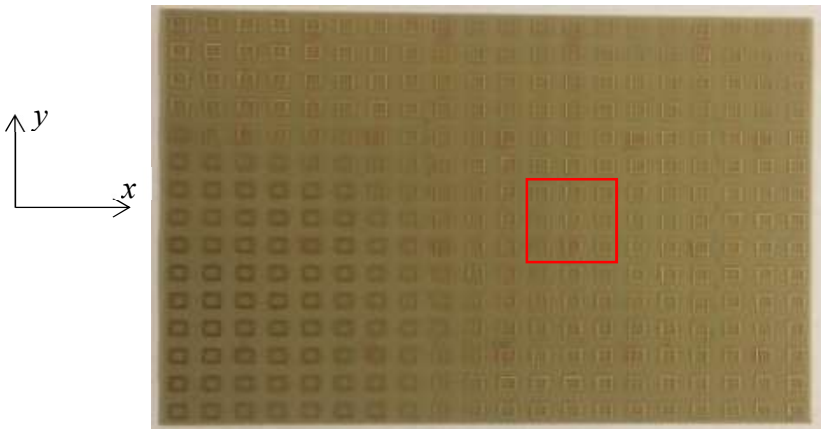

Figure 13. Photograph of a large FSS sensor with 3×3 strained elements indicated in the red square.

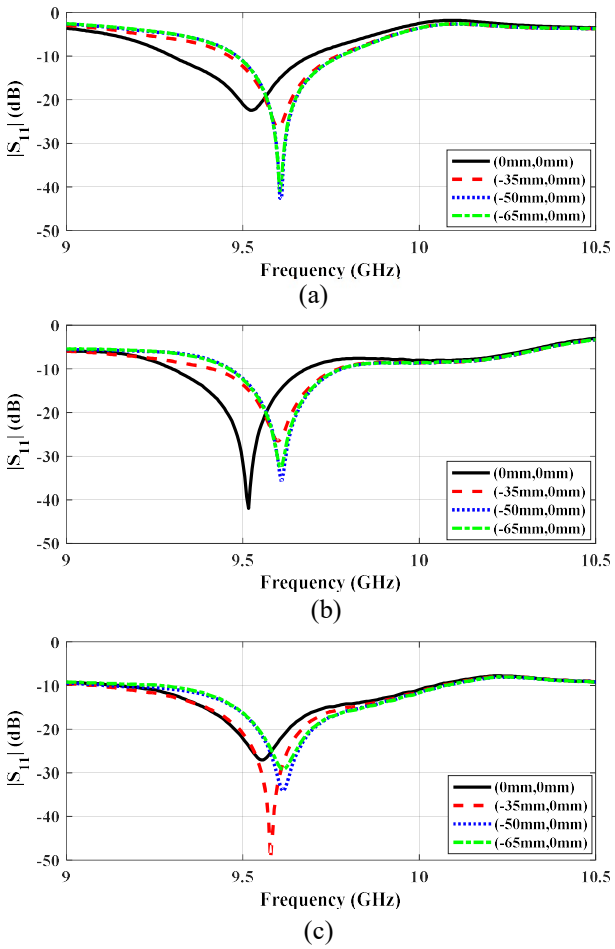

Figure 14. Measured $|S_{11}|$ of FSS sensor when illuminated by (a) HVF, (b) MVF, and (c) LVF.

5. CONCLUSION

Frequency selective surface (FSS)-based sensors have shown promise for numerous structural health monitoring (SHM) applications due to their sensitivity to the FSS geometry, substrate properties and environment. Additionally, their ease of implementation, planar structure and wireless interrogation are also positive attributes for SHM sensors. From a sensing perspective, the resolution of an FSS sensor is important as it relates to localized sensing applications. Therefore, this paper has studied (through simulation and measurement) the effect of illumination pattern and its footprint on the FSS sensor performance through the illumination and spill-over efficiencies of the sensor. It is shown that the optimum sensor cell dimensions (and hence maximum achievable resolution) for a given footprint is obtained when the maximum sensor cell efficiency (product of illumination and spill-over efficiencies) occurs. This is further supported through simulation and measurement results of individual sensor cells and a larger sensor that indicate the same.

REFERENCES

[1] B. A. Munk, Frequency Selective Surfaces Theory and Design. NewYork: Wiley, 2000.

[2] X. D. Hu, et al, “A miniaturized dual-band frequency selective surface (FSS) with closed loop and its complementary pattern," *IEEE Antennas and Wireless Propagation Letters* 8, pp 1374-1377, 2009.

[3] M. Mahmoodi, and K. M. Donnell, “Wideband Multi-Loop FSS Absorber Design Based on Q-factor Approach,” *2018 IEEE International Symposium on Antennas and Propagation & USNC/URSI National Radio Science Meeting*. IEEE, 2061-2062, 2018.

[4] F. Costa, and A. Monorchio, “A frequency Selective Radome with Wideband Absorbing Properties,” *IEEE Transactions on Antennas and Propagation* 6, No. 6, pp. 2740-2747, 2012.

[5] H. Chen, X. Hou, and L. Deng, “Design of Frequency-Selective Surfaces Radome for a Planar Slotted Waveguide Antenna,” *IEEE Antennas and Wireless Propagation Letters* 8, pp. 1231-1233, 2009.

[6] M. Li, Mudar A. Al-Joumayly, and Nader Behdad, “Broadband True-Time-Delay Microwave Lenses Based on Miniaturized Element Frequency Selective Surfaces,” *IEEE Transactions on Antennas and Propagation* 61, No. 3, pp.1166-1179, 2013.

[7] S. Jang, B. Kang, and J. Kim, “Frequency Selective Surface Based Passive Wireless Sensor for Structural Health Monitoring,” Smart Materials and Structures 22, No. 2, 2013.

[8] E. Kinzel, “Design of a Frequency-Selective Surface Strain sensor,” *2014 IEEE International Symposium on Antennas and Propagation & USNC/URSI National Radio Science Meeting.* IEEE, pp. 2074-2075, 2014.

[9] D. Pieper, et al. "Embedded FSS sensing for structural health monitoring of bridge columns." *Instrumentation and Measurement Technology Conference Proceedings (I2MTC), 2016 IEEE International*. IEEE, 2016.

[10] M. Mahmoodi, and K. M. Donnell, “Novel FSS-Based Sensor for Concurrent Temperature and Strain Sensing,” *2017 IEEE International Symposium on Antennas and Propagation & USNC/URSI National Radio Science Meeting.* IEEE, pp. 679-680, 2017.

[11] D. F. Pieper, and K. M. Donnell, “Application of Frequency Selective Surfaces for Inspection of Layered Structures,” *2015 IEEE International Instrumentation and Measurement Technology Conference (I2MTC)*. IEEE, 2015.

[12] M. Mahmoodi, and K. M. Donnell, “Active Frequency Selective for Strain Sensing,” *2017 IEEE International Symposium on Antennas and Propagation & USNC/URSI National Radio Science Meeting*. IEEE, pp. 675-676, 2017.

[13] Ch. Debus, and Peter Haring Bolivar, "Frequency Selective Surfaces for High Sensitivity Terahertz Sensing," *Applied Physics Letters* 91. No. 18, p. 184102, 2007.

[14] R. Melik, et al. "Metamaterial based telemetric strain sensing in different materials," *Optics express* 18.5, pp. 5000-5007, 2010.

[15] M. Mahmoodi, and K. M. Donnell, "Performance Metrics for FSS-Based Sensors," *IEEE Sensor Letters 1*, No. 6, Nov. 2017.

[16] B. A. Munk, *Finite antenna arrays and FSS*. John Wiley & Sons, 2003.

[17] Shishir, M. D., et al, "Frequency-Selective Surface-Based Chipless Passive RFID sensor for Detecting Damage Location," *Structural Control and Health Monitoring*, Vol. 24, No. 12, 2017.

[18] M. Mahmoodi, and K. M. Donnell. "Effect of illumination pattern on FSS-based sensor resolution," *2018 IEEE International Instrumentation and Measurement Technology Conference (I2MTC)*. IEEE, 2018.

[19] C. A. Balanis, "Antenna Theory: Analysis & Design, John Willey & Sons," *Inc. Publication*, 1997.

[20] J. Huang, "Analysis of a microstrip reflectarray antenna for microspacecraft applications," 1995.

IV. ADAPTIVE RESOLUTION FOR LOCALIZED FSS-BASED SENSING BY SYNTEHTIC BEAMFORMING

ABSTRACT

Recently, frequency selective surface (FSS)-based sensors have shown potential for structural health monitoring due to their sensitivity to changes in element geometry, inter-element spacing, substrate properties, and local environment. In addition, these sensors are remotely interrogated and are planar in design, thereby providing a wireless sensing solution that can cover large areas. Traditionally, FSS sensors are analyzed assuming a uniform (plane wave) illumination. However, practically speaking, the sensor will be illuminated with a non-uniform excitation. In this way, the resolution of the sensor is limited to the illumination pattern (footprint) on the sensor. As such, a flexible illumination pattern is advantageous as it relates to the ability to interrogate the sensor on a localized or comprehensive basis. To this end, this paper considers a synthetic beamforming approach as a solution for localized sensing applications. This approach is proposed to generate an arbitrary beam shape with a desired footprint. Moreover, the illumination and spill-over efficiencies of the synthetic beam are defined, simulated, and discussed. The results show that a minimum focal area of $1\lambda_0 \times 1\lambda_0$ (3×3 unit cells for the FSS sensors considered here) is essential to achieve a spill-over efficiency of greater than 80%, thereby reducing the contribution of other neighboring unit cells on the sensor response. In addition, the illumination efficiency when a synthetic beam is utilized for illumination is greater than 80% due to the uniformity of the synthetic beam. Representative measurements were also performed on a sensor with a simulated strain profile.

1. INTRODUCTION

Frequency selective surfaces (FSSs) are periodic arrays of resonant structures (such as a patch or loop) located on a planar surface. When these arrays are illuminated with electromagnetic energy, a specific transmissive or reflective frequency response results [1]. When designed to operate in reflection mode, one-sided measurements are inherently facilitated. This is often of interest since some applications do not include access to both sides of the structure under test. Such one-sided sensors typically include a ground plane beneath the sensor substrate, which also provides an inherent insulating quality to the effect of the electromagnetic (material) properties of the structure upon which the sensor has been placed.

FSSs have traditionally been used for numerous applications including filters [2], reflectors and lenses [3], absorbers [4], [5], and radomes [5], [6]. In addition, FSS-based sensors have recently shown potential for applications in structural health monitoring (SHM) since the particular frequency response of an FSS is sensitive to the element geometry, inter-element spacing and substrate properties, along with the local environment. More specifically, these geometrical changes or changes in the substrate properties (dielectric constant, loss tangent, and thickness) can change the frequency response according to changes in conductor, dielectric and radiation losses. Hence, the frequency response features such as resonant depth, resonant frequency or quality factor can be monitored to determine the physical and geometrical changes on the FSS [7]. As a result, FSS-based sensing has shown promise for normal and shear strain sensing [8], crack detection [9], and detection of delaminations/disbonds within layered structures [10]. It is

also possible to monitor multiple measurands with a properly designed FSS-based sensor, such as the FSS sensor of [11] that has been designed for concurrent temperature and (normal) strain sensing. FSS sensors can also include active components. In this way, the sensor response can be modulated (or "tagged") and hence clearly delineated from other signals present [12]. Furthermore, FSS-based sensing has also seen application in the terahertz regime for measurement of paper thickness and humidity [13]. Another similar area of study is metamaterial-based sensors. Metamaterials are synthetic composite materials that can be considered similar to FSSs when used within an array of elements and externally illuminated. An example of metamaterial-based sensors is the double split ring resonator-based metamaterial for strain sensing [14], and a multi-functional metamaterial sensor for sensing of moisture, density and temperature [15]. Also, a metamaterial-based sensor for dual axis strain sensing in terahertz regime is presented in [16].

2. BACKGROUND

Generally speaking, sensor resolution is an important parameter for any sensor design. As it relates specifically to FSS-based sensing, the resolution is related to the illuminating excitation and sensor dimensions [18], [19]. As it relates to both of these concepts, theoretically, FSS analysis is conducted assuming the FSS to be an infinite two-dimensional (2D) array of elements that is illuminated by a uniform plane wave (i.e., an ideal FSS). However, in practice, an FSS is dimensionally finite with a finite number of elements. As a result, the surface current induced on the outer elements is different than the current induced on the central elements [17]. A similar deviation from the theoretical

is created due to a (practical) non-uniform excitation such as that from a horn antenna (rather than the uniform plane wave illumination). In fact, this is true even if the FSS is infinite in dimensions.

From a practical point-of-view, if an FSS-based sensor is utilized for sensing applications, exciting the FSS sensor with a sufficiently wide and uniform illumination pattern will excite all elements on the FSS simultaneously, resulting in low sensor resolution (as all elements will contribute to the FSS response). Thus, the sensing resolution will be equal to the FSS dimensions in this case. As a result, it is impossible to determine specific locations that are contributing to the comprehensive sensor response. That is to say (for example), a strain or temperature profile within the sensing area (i.e., FSS dimensions) cannot be quantified. Hence, if the sensor is considered to consist of many sensor cells (sub-FSSs) that can be illuminated on a local scale, the resolution of the sensor will be increased. To this end, localized FSS-based sensing has been considered in terms of the illumination footprint (on the FSS) and number of unit cells within the illuminated area [18], where the illumination footprint from a horn antenna is defined as containing 75% of the incident energy (with 25% of the radiated energy incident outside the sensor area of interest and hence not contributing to the desired sensor response). As such, the illumination approach may be improved by illuminating the area of interest with a highly focused (and low side lobe level) beam which illuminates uniformly over the area of interest. In this way, the (wasted) energy that is incident beyond the sensor area of interest is reduced, as is the unwanted effect of neighboring unit cells on the sensor cell response. To this end, in this paper, the potential for utilizing a synthetically focused beam as the illuminating source for localized FSS-based sensing is studied. This work is an extension

of [19], which focused on using synthetic beamforming (SBF) to generate a highly focused beam by focusing on a single unit cell within an FSS sensor. In this work, the SBF method is extended to generate a focused illumination footprint with an arbitrary beamwidth in order to provide flexibility in the illumination footprint dimensions and hence flexible resolution.

3. SYNTHETIC BEAMFORMING FOR FSS-BASED SENSING

In order to create a highly directive (i.e., focused) illumination pattern with a desired beamwidth and low side lobe level (SLL) for localized FSS-based sensing, the synthetic beamforming approach is used. Generally speaking, SBF techniques can be used to simulate a large synthetic aperture from which a highly directive beam can be obtained [19]-[20]. There are numerous techniques that can be used to realize SBF including raster scanning a single radiating antenna [19]-[20], or using mechanical or phased array scanning [21]. While a phased array approach lends itself to practical application, such systems are often custom designed per specific applications at considerable costs. Hence, for ease of use and to show proof-of-concept, in this work, SBF is achieved by raster scanning a small and wide-beamwidth antenna (open-ended waveguide, referred to as the transceiver) over the FSS sensor, as is illustrated in Figure 1. Specifically, a scanning aperture (i.e. raster scan path for the transceiver) located a distance, h, above the focal plane is shown, with step sizes for the raster scan in the x- and y-directions of Δx and Δy, respectively. The raster scan plane (and hence location of the transceiver) is referred to as the aperture plane, and the plane of the sensor, the focal plane.

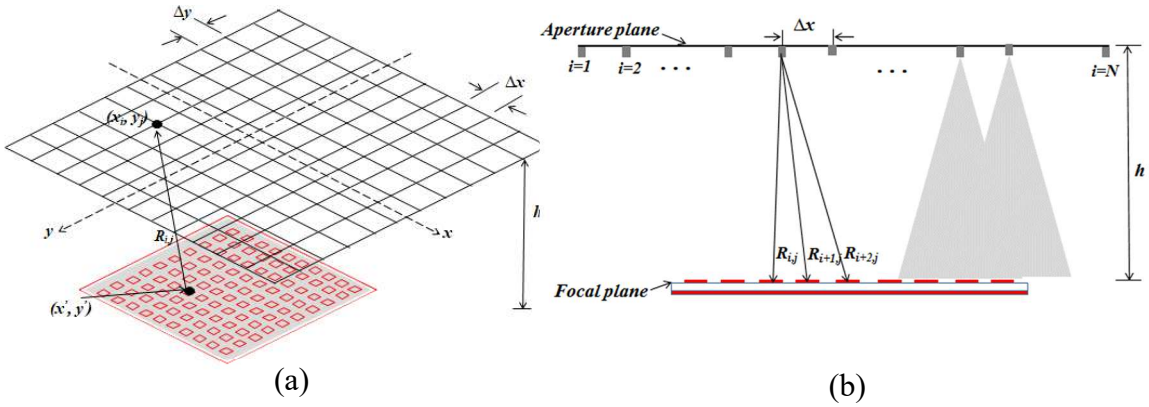

Figure 1. Schematic of two-dimensional scan for FSS-based sensing: a) 3D representation, and b) side view.

Using raster scanning, the complex reflection coefficient at the transceiver (S_{11}) can be measured. Then, the reflection coefficient or reflectivity function (Γ) at the focal plane can be found from the measured S_{11} [19]. Within this process, the effect of the two-way phase difference (due the round-trip distance from each scan location on the aperture plane to a focal point on the focal plane) must be considered. This phase delay is introduced as the point spread function (*PSF*) in [22], and is given as $PSF_{i,j}(x, x_i', y, y_j', z, z' = h, f) = e^{-j2k|R_{i,j}|}$; where x'_i and y'_j indicate the location of focal points, and x and y are the location of the transceiver antenna on the aperture plane in the x- and y-directions, respectively, k is the wave number equal to $2\pi/\lambda_0$, λ_0 is the wavelength of the operating frequency (for FSS-based sensing, the resonant frequency of the FSS), and R_{ij} is the distance between each scan location on the aperture plane and a focal point on the focal plane and is given as $R_{i,j} = \sqrt{(x_i - x')^2 + (y_j - y')^2 + h^2}$. Hence, S_{11} can be defined as the 2D convolution of Γ and *PSF* as follows:

$$S_{11}(x,y,f,z=0)=\sum_{x'}\sum_{y'}\left\{\begin{matrix}\Gamma(x',y',z=h,f)\\ PSF_{i,j}(x,x_i',y,y_j',z,z'=h,f)\end{matrix}\right\} \quad (1)$$

Here, in order to create a focused beam (from S_{11}) at a particular focal point, Γ can be found by back propagating the measured backscattered signal, $S_{11}(x, y, z = 0, f)$, to the focal point in order to correct the phase. The phase correction for the component of S_{11} from each array element (transceiver location) is related to the distance between the focal point and the array element on the aperture plane (or the conjugation of the *PSF*, PSF^*). Hence, Γ can be found from (2) as:

$$\Gamma(z=h,f)=\sum_{x}\sum_{y}S_{11}(x_i,y_j,z=0,f)(PSF)^* \quad (2)$$

It is possible to create a focused beam at all focal points (x', y') within the desired focal plane and obtain [Γ] for all locations of interest on the focal plane simultaneously. To this end, a synthetic beamforming technique utilizing the fast Fourier transform (FFT), similar to the synthetic aperture radar (SAR) algorithm of [20], can be used as follows:

$$\Gamma(x,y,z=h,f)=FT^{-1}\left\{FT\left\{S_{11}(x,y,z,f)\right\}.e^{jK_z h}\right\} \quad (3)$$

where $K_z=\sqrt{4K^2-K_x^2-K_y^2}$, $K_x=2\pi/\Delta x$ and $K_y=2\pi/\Delta y$ and are the wave numbers in the *z*, *x*, and *y* directions, respectively. As mentioned above, the SBF approach for a single focal point for FSS-based sensing is discussed in [19]. However, generating a synthetic beam (SB) with an arbitrary focal area is advantageous in that this approach can provide an adjustable illuminating footprint (and hence resolution) for the sensor. In this way, the changes on the sensor can be inspected on a small or large scale, depending on the illumination footprint. In addition, only one raster scanning measurement is required, and then, in conjunction with the adaptable SBF approach, different synthetic beams can be

generated synthetically off-line and hence the corresponding sensor response can be calculated as needed.

For clarity, it should be noted that the focal area represents the area within which the focal points are located (and are separate by the defined step sizes used in the SBF algorithm.). The focal area is also finite and has defined boundaries. This is in contrast with the illuminating footprint that represents the portion of the SB that is focused within the focal area along with the additional portion of the SB that is incident outside of the focal area. The footprint, therefore, does not have finite physical boundaries.

The focal area of the SB alone determines the achievable resolution of FSS-based sensor. However, the sensor response may differ when one unit cell vs. multiple unit cells are illuminated. More specifically, when a highly focused beam is used to illuminate an FSS sensor, it may achieve the highest possible resolution. However, if it illuminates only one unit cell within the sensor, FSS behavior will not be achieved since this (theoretical) response is related to the unit cell geometry and interaction between adjacent cells. To capture this inter-element effect, multiple focal points may be considered to generate a beam focused on an area larger than one unit cell, as is illustrated in Figure 2.. In this way, by increasing the focal area size, the frequency response may be improved. Hence, the method presented in [19] and also provided here in (1) and (2) can be expanded in such a way as to create a synthetic beam with a specified focal area. To this end, the summation of $PSF_{i,j}(x, x_i', y, y_j', z, z' = h, f)$ for all a set of focal points representing a focal area is defined as $J(x, y, z, f)$ and is given as:

$$J(x, y, z = 0, f) = \sum_{x'} \sum_{y'} PSF_{i,j}(x, x_i', y, y_j', z = 0, z' = h, f) \tag{4}$$

Therefore, by substituting $J(x, y, z = 0, f)$ from (4) into (2), Γ at the focal area can be found as (5):

$$\Gamma(z = h, f) = \sum_i \sum_j S_{11}(x_i, y_j, z = 0, f) J^*(x_i, y_j, z = 0, f) \tag{5}$$

where $J^*(x, y, z, f)$ is the conjugate of $J(x, y, z, f)$.

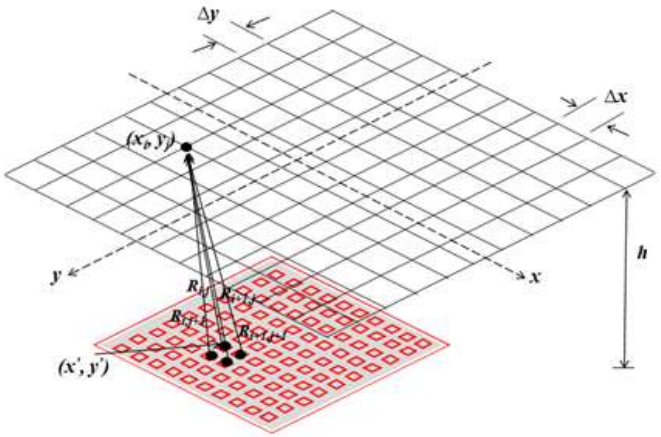

Figure 2. 3D representation of schematic of two-dimensional scan for FSS-based sensing.

To this end and to generate a simulated synthetic beam, the synthetic aperture size is considered to be 250 × 300 mm^2 (8.34 × 10 λ_0^2). Since the FSS sensor considered later is this work resonates in the X-band (8.2 – 12.4 GHz), the raster scan step sizes, Δx and Δy, were selected to be 5 mm (each) in order to meet the Nyquist sampling criteria (step size must be smaller than λ/4 at the highest operating frequency of 12.4 GHz) [20]. The step size also defines the dimensions of one focal point (i.e., 5×5 cm^2 in this case). In addition, four different focal areas are considered to represent different achievable resolutions, namely, 1, 5×5, 10×10, and 20×20 focal points. As discussed in [19] for a SB focused at a

single focal point, the effect of distance between the aperture and focal planes is more substantial [20]. In other words, the footprint is increased with increasing h. Therefore, since in this work, the focal area is expanded from that of [19] (i.e., one focal point vs. multiple), the effect of h on the illuminating footprint is considered here.

Another important property of an SB illumination is the SLL. More specifically, when the SLL of a synthetic beam is large, the frequency response of the illuminated area on the sensor may be affected by those elements outside of the main beam that are illuminated by a side lobe. In this way, the intended resolution is degraded. Also, as discussed in [19], the SLL of a SB (footprint of one focal point) is reduced with the application of a Hanning window. However, in [19], a symmetric Hanning window (symmetric distribution with maximum at the center of focal plane and minimum at the edges [23]) was used. This symmetric window caused a widening of the illuminating footprint for SBs focused off-center within the focal plane, specifically for larger h. Hence, to avoid this effect, an asymmetric Hanning window is used in this work with the maximum located at the center of focal area (footprint), as opposed to the center of the full focal plane. In this way, the effect of the Hanning window on the footprint of the synthetic beam with multiple focal points is studied, with the results valid for focal points located anywhere within the focal plane.

To this end, the reflectivity function on the focal plane (Γ) is simulated with and without the application of a Hanning window at 10 GHz, with the results shown in Figure 3 and Figure 4 for an h of $1\lambda_0$ and $5\lambda_0$, respectively. The results are represented along the x-axis since the response is symmetric in both directions. As seen in Figure 3, with the application of a window, the SB has a large SLL (~ -10 to -15dB as shown in Figure 3b

and d). As seen, for each SB with specific focal area, the inclusion of the Hanning window reduces the SLL. In addition, the Hanning window improves the uniformity of |Γ| across the focal area, as is shown in Figure 3b and c.

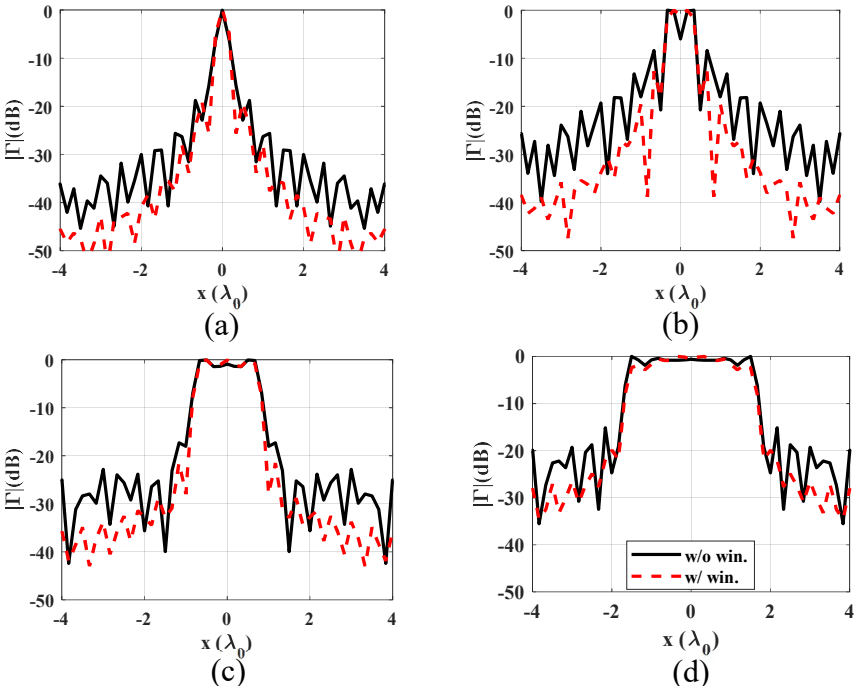

Figure 3. Synthetic beam with and without Hanning window when $h = 1\lambda_0$ and beamwidth with (a) 1 focal point, (b) 5×5 points, (c) 10×10 points, and (d) 20×20 points.

Next, by increasing h from $1\lambda_0$ to $5\lambda_0$, as shown in Figure 4, the SB is widened. The beam is further widened by the application of the Hanning window. Widening the beam means a larger illuminating footprint than the desired focal area is achieved, which increases the energy deposited outside of the intended focal area. This externally-deposited energy is larger for the SBs with smaller focal areas, as seen in Figure 4 a and b (with a single and 5×5 focal points, respectively). Also, the uniformity of |Γ| over the focal area is worse for $h = 5\lambda_0$ with the Hanning window. For example, SBs (i.e., |Γ|) with more focal

points (Figure 4c and d), are less uniform at edge of the focal area due to a widening of the footprint in comparison with the beams in Figure 3c and d for smaller *h*. However, in Figure 4 it can be seen that |Γ| outside of the focal area reduces to less than -40 dB when the Hanning window is applied. This can improve the performance of sensor response (specifically, the resolution) since the radiated energy is essentially solely incident upon the focal area of interest and not beyond it. To this end, in order to quantify the uniformity and degree of focus of the illuminating footprint, efficiency metrics common to reflectarray antennas [24]-[25] are adapted for FSS-based sensing, as is discussed next.

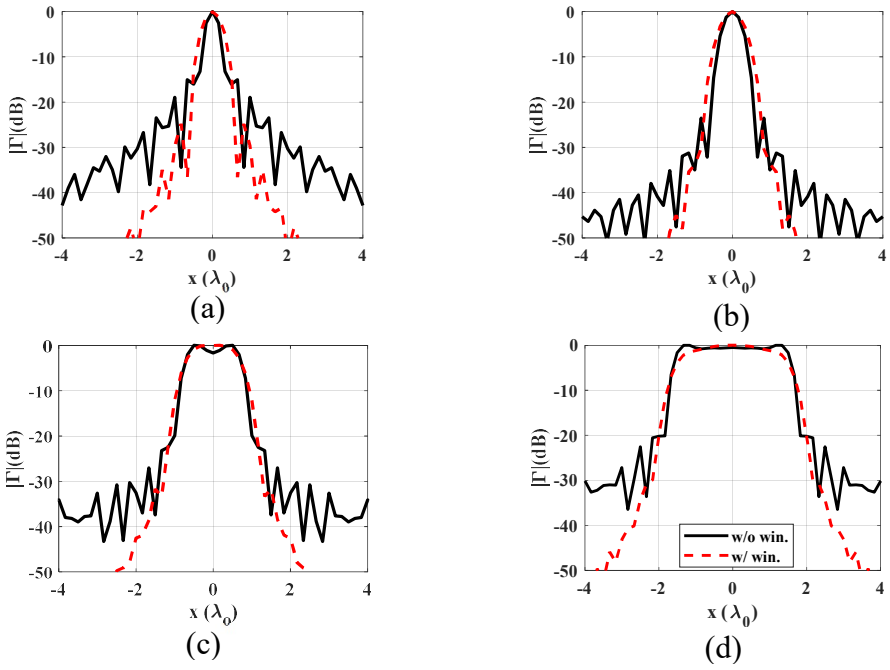

Figure 4. Synthetic beam with and without Hanning window when $h = 5\lambda_0$ and beamwidth with (a) 1 focal point, (b) 5×5 points, (c) 10×10 points, and (d) 20×20 points.

3.1. EFFICIENCY OF ILLUMINATING BEAM

In reflector and reflectarray antenna, the aperture efficiency metric is used to design an efficient antenna by a proper selection of the aperture size and the illumination beam pattern [24]-[25]. For reflectarrays in particular, the aperture efficiency is defined as product of two additional quantities known as illumination efficiency, η_{ill}, and spill-over efficiency, η_s. The illumination efficiency (η_{ill}) quantifies the uniformity of the electric field distribution over the aperture, and the spill-over efficiency (η_s) quantifies the portion of the total radiated energy that is incident within the focal area (i.e., reflectarray aperture). As it relates to FSS-based sensing, when a high η_{ill} is achieved, the effect of nonuniform excitation on the sensor response will be reduced/minimized. Likewise, for a high η_s, the effect of adjacent sensor cells on the response from a given cell of interest will be reduced/minimized. Hence, in order to apply this analysis approach to FSS-based sensing, the sensor cell size/illumination footprint of the focused beam is considered as the aperture size. Here, the uniformity alone of the illuminating beam is quantified through η_{ill} (unlike that of [25] that included element effects). Hence, η_s and η_{ill} are used to quantify the effect of windowing on 1) the suppression level of $|\Gamma|$ beyond the focal area for different focal area sizes, and 2) the uniformity of $|\Gamma|$ on the focal area within the focal plane.

As shown in [24]-[25] for reflector antennas, when an illuminating source with a radiation intensity (pattern) represented by $\cos^q\theta$ (where θ is the elevation angle and the directivity of the beam is directly proportional to q) is considered as the illuminating source, η_{ill} and η_s are complementary (meaning an increase in one results in a decrease in the other). In other words, when η_s is large (meaning the radiated energy is focused/contained within the reflectarray aperture), η_{ill} will be low (resulting from the high

degree of non-uniformity of the field across the same aperture). Hence, the reflector antenna can be designed in such a way to achieve maximum total efficiency by proper selection of aperture size, and illumination source and its pattern. As such and relating this concept to FSS sensing with SBF, using a synthetic beam illumination, the uniformity of the SB across the focal area and hence the footprint is high and therefore η_{ill} is improved. In addition, the spillover efficiency is improved since a majority of the incident energy is focused within the focal area. Thus, to find the efficiency of the synthetic beam generated by the SBF approach, the simulated $|\Gamma|$ (i.e., the synthetic beam) on the focal plane (in terms of S_{11} and J, see (5)) is used. In this way, η_s and η_{ill} are defined as follows:

$$\eta_s = \frac{\sum_{i=1}^{m}\sum_{j=1}^{n}\left|S_{11}(x_i, y_j, z=0, f)\times J^*(x_i, y_j, z=0, f)\right|^2}{\sum_{i=1}^{M}\sum_{j=1}^{N}\left|S_{11}(x_i, y_j, z=0, f)\times J^*(x_i, y_j, z=0, f)\right|^2} \tag{6}$$

$$\eta_{ill} = \frac{\left|\sum_{i=1}^{m}\sum_{j=1}^{n} S_{11}(x_i, y_j, z=0, f)\times J^*(x_i, y_j, z=0, f)\right|^2}{mn\sum_{i=1}^{m}\sum_{j=1}^{n}\left|S_{11}(x_i, y_j, z=0, f)\times J^*(x_i, y_j, z=0, f)\right|^2} \tag{7}$$

where the synthetic aperture is considered as an array with $M\times N$ elements, and the number of focal points is $m\times n$. As mentioned before, the spacing between elements of the synthetic aperture is 5 mm in order to satisfy the Nyquist sampling criteria. However, to calculate efficiencies, a step size of 1 mm is used in order to increase the number of sampling points in order more accurately characterize the radiated energy within a desired focal area, the total radiated energy, and the uniformity of incident field within the focal area. To this end and by using (6), η_s is calculated in terms of the focal area as shown in Figure 5 for cases

without and with Hanning windows applied for $h = 1\lambda_0$ and $5\lambda_0$. As can be seen, η_s is very low for smaller focal areas, specifically for one focal point. This occurs because the illumination footprint is larger than the focal area, which results in an increase in spill-over energy (deposited outside the focal area). Also, as explained earlier, applying the Hanning window to the SB for higher h widens the illuminating footprint (specifically for SBs with a smaller focal area), meaning the illuminating footprint is larger than the focal area. Therefore, this causes more spill-over energy (and hence a lower η_s), as is seen in Figure 5 for $h = 5\lambda_0$ with a Hanning window for focal areas less than ~2 λ_0^2 (and is particularly evident for 1 λ_0^2 or less). As such, while the Hanning window does reduce SLLs, this reduction causes a marginal improvement in η_s on the order of 2% for all cases shown in Figure 5. In addition, for small focal areas such as one focal point (~0.03 λ_0^2), η_s is ~60% and <40% for $1\lambda_0$ and $5\lambda_0$, respectively, as is also evident in Figure 5. The results of Figure 5 also indicate that when the focal area exceeds one focal point, η_s increases to more than 80% and 70% for $h = 1\lambda_0$ and $5\lambda_0$, respectively. However, the rate of increase of η_s reduces as the focal area increases. This is attributed to the fact that as the focal area increases, it approaches the total dimensions of the focal plane. As such, for this case, a majority of the incident energy is located within the focal area and minimal energy is located outside this region. In other words, as the focal area approaches the dimensions of the focal plane, the rate of increase in energy confined within the focal area will reduce and hence so does the rate of increase of η_s.

Next, using (7), η_{ill} is calculated and shown in Figure 6. It can be seen that η_{ill} also increases as the focal area increases. This follows what is shown in Figure 3 and Figure 4, where improved uniformity of the illuminating beam occurs as the focal area increases.

However, it is seen that when the Hanning window is applied to the SB for $h = 5\lambda_0$, η_{ill} decreases by a maximum of 3%. This is attributed to the reduction in the discrete boundary of the SB within the focal area (i.e, more gradual boundary), as shown in Figure 4.

Lastly, the total efficiency (i.e., product of η_s and η_{ill} shown in Figure 5 and Figure 6) is shown in Figure 7 for completeness. Overall, the same trends of Figure. 5 and Figure 6 are evident and discussed above. Ultimately, unlike traditional reflectarray efficiency analysis where η_s and η_{ill} are complementary [25], both efficiencies can be improved individually, as has been discussed above with regards to Figure. 5 and Figure 6. In this way, η_{total} is also improved through the application of the SBF approach.

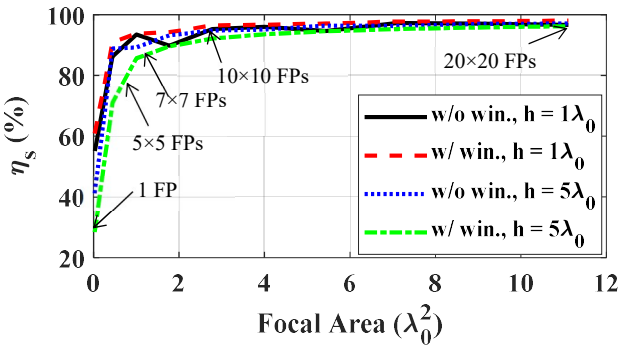

Figure 5. Spill-over efficiency comparison of synthetic beam with uniform and Hanning windows at h of $1\lambda_0$ and $5\lambda_0$ in terms of focal area size.

3.2. APPLICATION OF SBF FOR LOCALIZED FSS-BASED SENSING

In order to illustrate the application of the flexible SBF approach to FSS-based sensing, simulations were performed at X-band (8.2 – 12.4 GHz) considering a conductor backed square loop unit cell designed on an FR-4 substrate (relative permittivity of 4.2 and

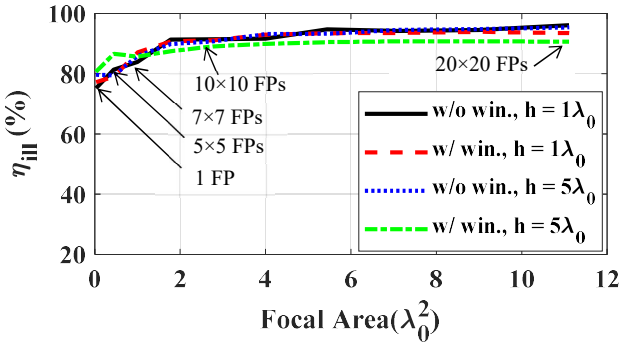

Figure 6. Illumination efficiency comparison of synthetic beam with uniform and Hanning windows at h of $1\lambda_0$ and $5\lambda_0$ in terms of focal area size.

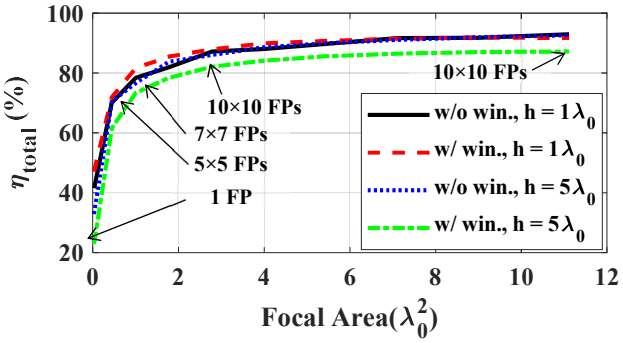

Figure 7. Total efficiency comparison of synthetic beam with uniform and Hanning windows at h of $1\lambda_0$ and $5\lambda_0$ in terms of focal area size.

loss tangent of 0.023), as shown in Figure 8, along with the simulated resonant response. The unit cell has a resonant frequency of 10 GHz. The dimensions of the unit cell, as illustrated in Figure 8a, are L = 10 mm, a = 4.95 mm, w = 0.4 mm and t = 32 mils.

A potential FSS-based sensing application is that of unidirectional strain sensing [7], [11], [12]. To this end, the frequency response of the sensor of Figure 8, with and without the presence of 5% unidirectional strain (assuming strain and polarization are parallel), is shown in Figure 8b. As seen, the unstrained sensor resonates at 10 GHz (as designed) with a resonant depth of approximately -20 dB. In addition, when under 5% unidirectional

strain, the resonant response reduces by 350 MHz (due to the increase in loop and unit cell dimensions).

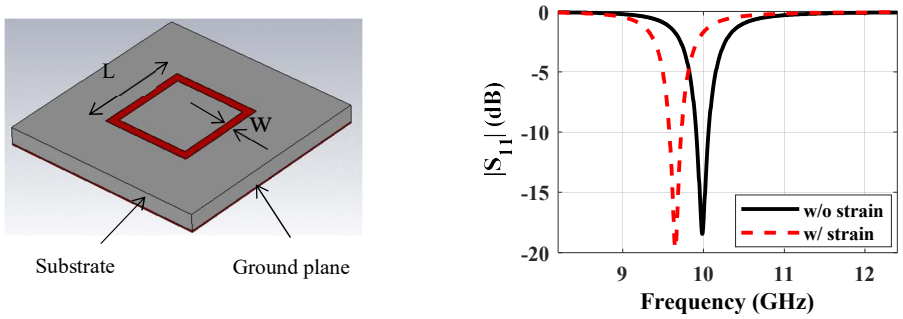

(a) (b)

Figure 8. (a) Square loop unit cell and (b) $|S_{11}|$ of ideal FSS sensor.

As it relates to the goals of this work (i.e., localized sensing via the SBF approach), the FSS sensor of Figure 8 with 15×20 unit cells (see Figure 9a) was fabricated and measured, with the results shown in Figure 10. In order to model localized strain, the dimensions of 5×5 elements within the sensor were altered in order to mimic a 5% strain in the *x*-direction (strained elements indicated within the red square in Figure 9). To compare the sensor response illuminated by a highly focused beam with a wider beam, two beams were generated (as shown in Figure 3a and b) using the SBF approach for $h = 1\lambda_0$.

The illumination footprint for this beam for one focal point is approximately 1×1 cm^2 (~ 1×1 unit cell) and the wider beam for 5×5 focal points has a illumination footprint of approximately 30×30 mm^2 (~ 3×3 unit cells). As discussed in Section 3.1, the efficiencies for a synthetic beam ($h = 1\lambda_0$), with or without the application of a window, are very similar. However, the calculated total efficiencies (Figure 7) for an illumination footprint with a single focal point and 5×5 focal points are significantly different with an

η_{total} of ~39% and ~78%, respectively. Thus, these two illumination footprints are selected in order to show that the sensor response is improved when it is illuminated by a wider focal area since it has a higher η_{total} (see Figure 7). Of course, a beam with a focal area wider than 5×5 focal points could be selected and will have a higher η_{total} (80% to 90%, as seen in Figure 7), but at the cost of reduced resolution.

To begin, measurements were made by measuring the reflection response of the sensor with a uniform focused illumination using the SBF approach. Specifically, the focused illumination beam was created by raster scanning an X-band open-ended waveguide (OEWG) with aperture dimensions of 10.16 × 22.86 mm^2 located a distance of $h = 1\lambda_0$ from the FSS sensor with a step size of 5 mm in the x- and y-directions. In this way, an overall synthetic aperture of 250 × 300 mm^2 is considered. The synthetic aperture size is considered 100 mm larger (in both directions) than the width and length of the sensor with dimensions of 150 × 200 mm^2 (centered with respect to the sensor). Additionally and as above, a Hanning window is applied to the measured S_{11} over the synthetic aperture (with a step size of 5 mm in the x and y directions) for all results presented in this Section.

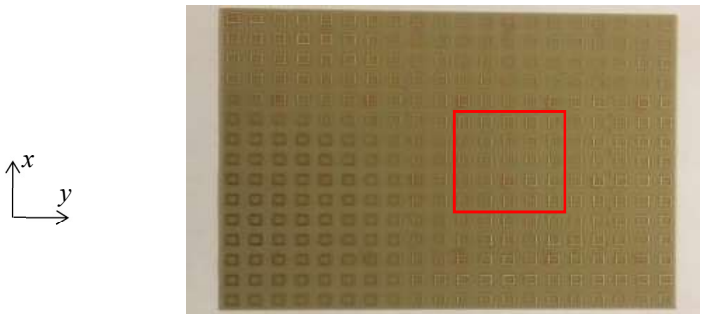

Figure 9. Photograph of FSS sensor with the localized strained area indicated in the red square.

The frequency response of the FSS sensor is calculated from the measured data when it is illuminated by synthetic beams at different locations over the FSS sensor. The 2D representation of the resonant frequency and depth (process of (5) applied for each measurement location) over the sensor (focal plane) is shown in Figure 10. As seen in Figure 10a and c, the resonant frequency of the sensor (shown in GHz) is shifted at the location of the strained elements for both illumination footprints. More specifically, the resonant frequency in the area without strain is ~9.62 GHz, and in the location of strain reduced to ~9.27 GHz (350 MHz frequency shift which is similar to the expected frequency shift of Figure 8b). As seen in Figure 10a, the area with frequency shift on the 2D representation of the resonant frequency is more similar to the exact area of strained (Figure 9) when the sensor is illuminated by the wider illumination (Figure 3b). However, the sensor response with a highly focused illumination (one focal point, see Figure 3a) shown in Figure 10c shows a larger strained area but a reduction in frequency shift (25 MHz less than the ideal sensor response of Fig 9b and the response of Figure 10a). This is because the wider illumination footprint will illuminate a larger area including more unit cells (~3×3 unit cells) and the frequency response will be more similar to the ideal FSS response.

In addition, as it relates to resonant depth, Figure 10b and d show a change in resonant depth that is indicated the figures as a lighter/white square ring. The location of this square ring (Figure 10b and 10d) indicates the boundary between the strained and unstrained areas on the sensor and hence indicates where the frequency shift occurs in the sensor response.

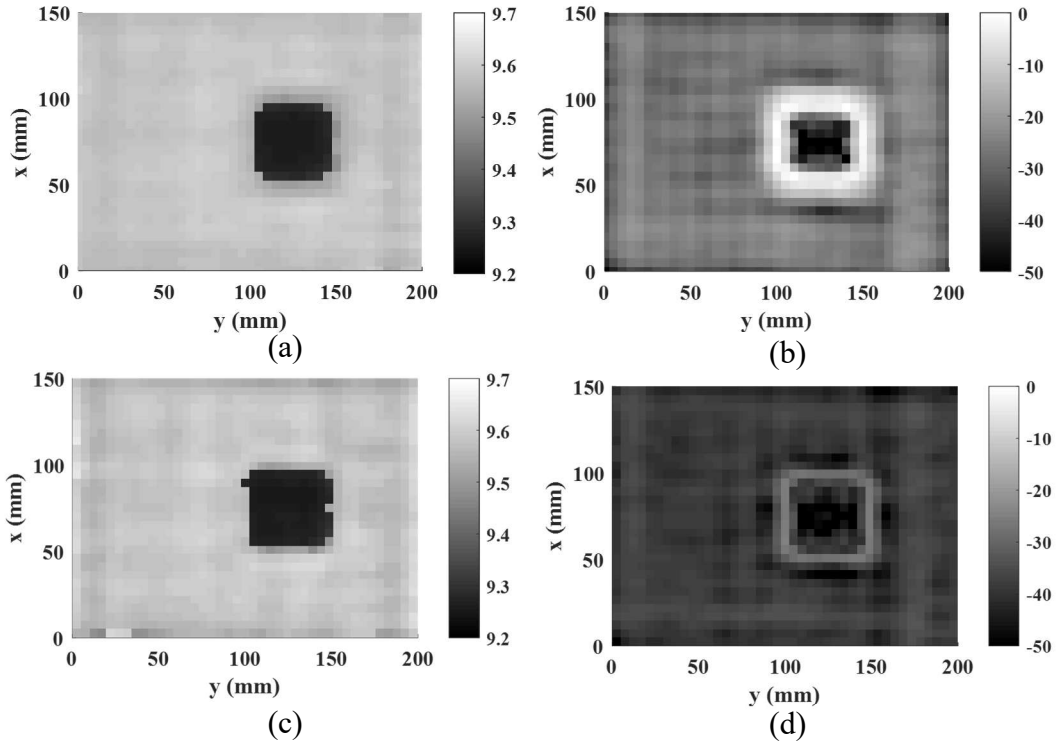

Figure 10. The resonant frequency (a) and depth (b) from sensor with synthetic illumination footprint of 5×5 number of focal points. The resonant frequency (c) and depth (d) from sensor with synthetic illumination footprint of a single focal point.

4. CONCLUSION

Frequency selective surface-based sensors have recently been considered as a structural health monitoring solution due to their sensitivity to geometry and local environment, in addition to their planar structure and wireless interrogation. In order to utilize such sensors for localized sensing, a focused beam is needed to illuminate the sensor and achieve a high resolution. Also, such sensors can effectively include an adaptable resolution, as the resolution can be adjusted by changing the illumination footprint. To this end, this paper investigated the synthetic beamforming approach as a solution for localized FSS sensing with a flexible uniform focused illumination beam. To quantify the

improvements offered by the addition of this approach, the definitions of illumination and spill-over efficiency were modified (from those used with reflectarray antennas). The results shown that for small focal areas, the spill-over efficiency reduces. In addition, the illumination efficiency is greater than 75% for all focal areas considered. Additionally, this approach was applied to an FSS sensor with 15×20 unit cells that included 5×5 strained elements. Measurement results indicate that localized sensing via the SBF approach was successfully applied, as evidenced by the detected area under localized strain.

REFERENCES

[1] B. A. Munk, Frequency Selective Surfaces Theory and Design, NewYork: Wiley, 2000.

[2] X. D. Hu, et al, "A miniaturized dual-band frequency selective surface (FSS) with closed loop and its complementary pattern," *IEEE Antennas and Wireless Propagation Letters* 8, pp 1374-1377, 2009.

[3] M. Li, A. Al-Joumayly Mudar, and Nader Behdad, "Broadband True-Time-Delay Microwave Lenses Based on Miniaturized Element Frequency Selective Surfaces," *IEEE Transactions on Antennas and Propagation* 61, No. 3, pp.1166-1179, 2013.

[4] M. Mahmoodi,and K. M. Donnell, "Wideband Multi-Loop FSS Absorber Design Based on Q-factor Approach," *2018 IEEE International Symposium on Antennas and Propagation & USNC/URSI National Radio Science Meeting*. IEEE, 2061-2062, 2018.

[5] F. Costa, and A. Monorchio, "A frequency Selective Radome with Wideband Absorbing Properties," *IEEE Transactions on Antennas and Propagation* 6, No. 6, pp. 2740-2747, 2012.

[6] H. Chen , X. Hou, and L. Deng, "Design of Frequency-Selective Surfaces Radome for a Planar Slotted Waveguide Antenna," *IEEE Antennas and Wireless Propagation Letters* 8, pp. 1231-1233, 2009.

[7] M. Mahmoodi and K. M. Donnell, “Performance Metrics for Frequency Selective Surface-Based Sensor,” *IEEE Sensor Letter*, Vol. 1, No. 6, Nov. 2017.

[8] E. Kinzel, “Design of a Frequency-Selective Surface Strain Sensor,” IEEE, Antennas and Propagation Society International Symposium (APSURSI), pp. 2074-2075, 2014.

[9] S. Jang, B. Kang, and J. Kim, “Frequency Selective Surface Based Passive Wireless Sensor for Structural Health Monitoring,” Smart Materials and Structures, Vol. 22, No. 2, 2013.

[10] D. F. Pieper, and K. M. Donnell, “Application of Frequency Selective Surfaces for Inspection of Layered Structures,” Instrumentation and Measurement Technology Conference (I2MTC), pp. 1204-1209, 2015.

[11] M. Mahmoodi, and K. M. Donnell, “Novel FSS-Based Sensor for Concurrent Temperature and Strain Sensing,” IEEE, Antennas and Propagation Society International Symposium (APSURSI), pp. 679-680, 2017.

[12] M. Mahmoodi, and K. M. Donnell, “Active Frequency Selective Surface for Strain Sensing,” IEEE Antennas and Propagation Society International Symposium (APSURSI), pp. 679-680, 2017.

[13] S. M Martin G, “Terahertz Multiparameter Sensor using Fiber-Interrogated Frequency Selective Surface," *arXiv* preprint arXiv:1311.6390, 2013 .

[14] R. Melik, et al. “Metamaterial Based Telemetric Strain Sensing in Different Materials,” *Optics express* 18.5, pp. 5000-5007, 2010.

[15] E. Ekmekci, et.al., “Multi-functional metamaterial sensor based on a broad-side coupled SRR topology with a multi-layer substrate,” *Applied Physics A,* Vol. 110. No. 1, pp. 189-197, 2013.

[16] J. Li, et al., “Flexible Terahertz Metamaterials for Dual-Axis Strain Sensing,” *Optics letters*, Vol. 38, No.12, pp. 2104-2106, 2013.

[17] B. A. Munk, Finite Antenna Arrays and FSS, John Wiley & Sons, 2003.

[18] M. Mahmoodi, and Kristen M. Donnell, “Effect of illumination pattern on FSS-based sensor resolution,” *2018 IEEE International Instrumentation and Measurement Technology Conference (I2MTC)*. IEEE, 2018.

[19] M. Mahmoodi, Mohammad Tayeb Ghasr, and Kristen M. Donnell. "Synthetic beamforming for localized FSS-based sensing." *2018 IEEE International Instrumentation and Measurement Technology Conference (I2MTC)*. IEEE, 2018.

[20] J. T. Case, M. T. Ghasr, and R. Zoughi, "Optimum Two-Dimensional Uniform Spatial Sampling for Microwave SAR-Based NDE imaging systems," IEEE Transactions on Instrumentation and Measurement, Vol. 60, issue 12, pp. 3806-3815, 2011.

[21] Y. F. Wu, Y. J. Cheng, and Z. X. Huang. "Ka-band near-field-focused 2-D steering antenna array with a focused Rotman lens," *IEEE Transactions on Antennas and Propagation*, Vol. 66., No. 10, pp. 5204-5213, 2018.

[22] F. Gumbmann, P. H. Tran, Jochen Weinzierl, and Lorenz-Peter Schmidt, "Advanced broadband millimetre-wave characterization techniques of dielectrics," *ECNDT Berlin,* 2006.

[23] Albert Nuttall, "Some windows with very good sidelobe behavior," *IEEE Transactions on Acoustics, Speech, and Signal Processing* Vol. 29. No. 1, pp. 84-91, 1981.

[24] C. A. Balanis, "Antenna Theory: Analysis & Design, John Willey & Sons," *Inc. Publication*, 1997.

[25] J. Huang, "Analysis of a microstrip reflectarray antenna for microspacecraft applications," 1995.

SECTION

2. CONCLUSIONS AND RECOMMENDATIONS

2.1. CONCLUSIONS

The work within this dissertation focuses on the fundamentals of frequency selective surfaces from a sensing point-of-view in order to advance the science behind FSS-based sensing. In last decade, FSSs have shown potential for wireless sensing including crack detection, strain sensing, inspection of layered structures, concurrent temperature and strain sensing, etc. FSSs are uniquely well-suited for many sensing applications due to their planar structure and ease of implementation, in addition to their sensitivity to FSS element geometry, inter-element spacing and substrate properties (permittivity, loss tangent and thickness).

FSSs are analyzed theoretically as a unit cell with periodic boundary conditions in order to mimic an infinite array of unit cells with a uniform illumination. However, in practice, an FSS is dimensionally finite and undergoes a non-uniform illumination pattern. As such, the differences between the theoretical and practical cases must be understood in order to utilize FSSs for sensing. To this end, the work presented within this dissertation focuses on 1) studying the effect of element geometry and substrate properties on the theoretical FSS response; 2) defining performance metrics for FSS-based sensing in order to evaluate and quantify the response of an FSS sensor; 3) determining the maximum achievable resolution of FSS-based sensors for a given illumination pattern; and 4)

achieving an adaptive resolution for localized FSS-based sensing using a synthetic beamforming approach.

In Paper I, the frequency response of a theoretical rectangular patch- and loop-based FSS with Floquet excitation is studied using a cavity model and quality factor approach. Specifically, a closed form solution for the reflection response of both FSSs based on the radiation, conductor, and dielectric quality factors is provided. A new model for the radiation quality factor of the loop unit cell is developed and the model for the rectangular patch is modified from [26]. In both, the effect of fringing fields and the frequency dependent effective permittivity are included. The closed form solution of both FSSs is compared with full-wave simulation for a wide range of substrate properties including permittivity, loss tangent, and thickness. Good agreement between the model and full wave simulation is achieved.

In Paper II, the quality factor analysis is used to analyze the effect of substrate properties on the response of two theoretical rectangular patch and loop-based FSS sensors. Specifically, the response is quantified via three performance metrics (resonant frequency, resonant depth and the quality factor). It is shown that by a proper selection of the substrate, the sensitivity of the theoretical FSS sensor can be improved. In addition, it is shown that a change in substrate permittivity (such as due to moisture ingress or cracking) does not affect the sensitivity of the resonant frequency to a different measurand (i.e. strain).

In Paper III, the resolution of an FSS-based sensor is improved through a localized sensing approach, achieved by utilizing a finite illumination pattern (i.e. from a horn antenna). In this approach, the footprint of the localized illumination pattern on the sensor determines the sensor cell size. However, as FSSs in general are assumed to have a uniform

excitation, differences in performance are introduced due to the localized illumination. In other words, the illumination footprint, intended for a given cell, may illuminate beyond the intended cell and hence the response may be affected. Additionally, the spatial deviation within the illumination footprint may also cause deviation in the response (from that of the "ideal" uniform case). Hence, an approach is presented similar to the aperture efficiency in reflectarray antennas to find the maximum efficiency for the illumination pattern where the effects of pattern non-uniformity and spill-over (into adjacent cells) energy are minimized. It is shown when the optimum sensor cell size is determined by this approach, the sensor cell response is very close to the ideal FSS response, with minimum contribution from adjacent sensor cells.

In Paper IV, as a solution for localized FSS sensing with a flexible, uniform, and focused illumination beam, an approach based on the synthetic beamforming is presented. To quantify the improvements offered by the addition of this approach, the definitions of illumination and spill-over efficiency were modified (from those used with reflectarray antennas). The results shown that for small focal areas, the spill-over efficiency reduces. In addition, the illumination efficiency is greater than 75% for all focal areas considered. Additionally, this approach was applied to an FSS sensor that included a strained area. Measurement results indicate that localized sensing via the synthetic beamforming approach was successfully applied, as the area under localized strain was successfully detected.

2.2. RECOMMENDATIONS

The following recommendations are proposed for further study in this area.

2.2.1. Sensitivity Analysis. Regarding Paper I, the primary goal of the modeling of the patch- and loop-based FSS sensors was to analyze the sensitivity of FSS response to the element design parameters in order to determine the most sensitive design. To this end, the following future work is suggested:

1) The analytical modeling of the frequency response of FSS unit cells was completed and verified for different substrate properties such as thickness (5 mils to 140 mils), relative permittivity (2-8), and loss tangent (0.02-0.09). However, a sensitivity analysis of the reflection response to each parameter remains. Also, fabrication limitations should be considered in the design process. For example, if there is a tolerance in the microstrip width line, the FSS design can be adjusted in a way to be less sensitive to the microstrip width line for very narrow widths (i.e. 1-4 mils).
2) The sensitivity of the sensor to a sensing parameter such as strain can be studied when there are other unwanted environmental variations such as moisture ingress. For example, moisture ingress can change the dielectric properties (both permittivity and loss factor). Then, it may cause a change in the frequency response of the FSS sensor. Therefore, the effect of external environmental factors on the sensitivity of FSS sensors can be studied.
3) In the modeling of the radiation quality factor, the loop is considered in such a way that the mutual coupling between adjacent elements and the coupling inside of the loop (amongst loop arms) must be minimal when a thick substrate is used. The model can be extended to include the effect of mutual coupling inside or outside of the loop.

4) The sensitivity to incident angle is reduced when FSS designs are miniaturized. Hence, the sensitivity of FSS to incident angle should be studied for two cases: 1) if an FSS is miniaturized in order to have a small spacing between the elements (meaning a large mutual coupling), 2) if an FSS is designed with a large spacing between adjacent elements (or small mutual coupling), and the element has a large electrical length to resonate in lower frequency and shrink the electrical dimension of the unit cell (i.e. fractal elements).
5) Finally, the sensitivity of FSS sensor to the phase response can be advantageous. This is because the phase response for the FSS with a large resonant depth has a sharp variation in phase which may be more sensitive to the measurand of interest than the magnitude response of the FSS (albeit more difficult to measure).

2.2.2. Finite FSS Normalization. In all finite FSS simulations and measurements that are done in this work, the complex frequency response from background of FSS is subtracted from the complex frequency response of the FSS. In cases that illumination footprint is larger than the size of the FSS, it is necessary to do this normalization. However, when illumination footprint is located within the FSS, the normalization has minimal effect on the response of FSS. In such cases that FSS is considered to consist of many sensor cells, the measurement of the frequency response of sensor cells can be done by raster scanning the illuminating antenna, and then the background (without the prsdence of the FSS) measured using the same antenna at the same locations may be challenging. Hence, to avoid the need of characterizing the background, use of the FSS cells can be limited to the sensor cells that are completely within the sensor and offset from the edges.

2.2.3. Sensor Cell Efficiency. In Paper III, the illumination and spill-over efficiencies are used to define the efficiency of the sensor cell. In this paper, the sensor cell efficiency is related only to the illumination pattern and the size of the sensor cell. It would be advantageous to include the effect of the number of unit cells within the sensor cell to the sensor cell efficiency. It is shown in [30] that by implementing the miniaturized FSS, the resolution of FSS sensor and the sensitivity of the sensor cell to small anomalies increases. This is due to the high density of the elements in the same size of the sensor cell using the miniaturized FSS design. Hence, the sensor cell efficiency might be improved by using the miniaturized unit cells, as this approach can be used to increase the element density within a given cell dimension.

2.2.4. Reflection Mode FSS Sensor. It is beneficial if the FSS sensor operates in reflection mode as a one-sided measurement is often desired for sensing. However, designing the FSS in reflection mode with a ground plane can be challenging, particularly as operating frequencies increase. Hence, multi-layer FSSs that incorporate an absorbing layer are an alternative to such designs. In other words, an FSS with the desired response can be designed without a ground plane and cascaded with a wideband absorbing FSS to remove the effect of substructures on the response.

BIBLIOGRAPHY

[1] B. A. Munk, Frequency Selective Surfaces Theory and Design. NewYork: Wiley, 2000.

[2] Hu, Xiao-Dong, et al, “A miniaturized Dual-Band Frequency Selective Surface (FSS) with Closed Loop and its Complementary Pattern," *IEEE Antennas and Wireless Propagation Letters*, Vol. 8, pp 1374-1377, 2009.

[3] Mahboobeh Mahmoodi, and Kristen M. Donnell, “Design of a new bi-state active frequency selective surface,” *2016 IEEE International Symposium on Antennas and Propagation (APSURSI)*. IEEE, 2016.

[4] M. Li, Mudar A. Al-Joumayly, and Nader Behdad, “Broadband True-Time-Delay Microwave Lenses Based on Miniaturized Element Frequency Selective Surfaces,” *IEEE Transactions on Antennas and Propagation*, Vol. 61, No. 3, pp. 1166-1179, 2013.

[5] F. Costa, et al, “A frequency Selective Radome with Wideband Absorbing Properties,” *IEEE Transactions on Antennas and Propagation* 6, No. 6, pp. 2740-2747, 2012.

[6] H. Chen, et al, “Design of Frequency-Selective Surfaces Radome for a Planar Slotted Waveguide Antenna,” *IEEE Antennas and Wireless Propagation Letters*, Vol. 8, pp. 1231-1233, 2009.

[7] A. Edalati, and Kamal Sarabandi, “Wideband, wide angle, polarization independent RCS reduction using nonabsorptive miniaturized-element frequency selective surfaces,” *IEEE Trans. on Ant. and Prop.*, Vol. 62, No. 2, pp. 747-754, 2014.

[8] Mei Li, et al., “An Ultrathin and broadband broadband Absorber Using Resistive FSS,” *IEEE Antenna and Wireless letters,* Vol. 11, pp. 748-751, 2012.

[9] Mahboobeh Mahmoodi, and Kristen M. Donnell, “Wideband Multi-Loop FSS Absorber Design Based on Q-factor Approach,” *2018 IEEE International Symposium on Antennas and Propagation & USNC/URSI National Radio Science Meeting*. IEEE, pp. 2061-2062, 2018.

[10] F. Costa, et al, “A circuit-based model for the interpretation of perfect metamaterial absorbers,” *IEEE Transactions on Antennas and Propagation*, Vol. 61, No. 3, pp. 1201-1209, 2012.

[11] Mahboobeh Mahmoodi, and Kristen M. Donnell, "Performance Metrics for FSS-Based Sensors," *IEEE Sensor Letters*, Vol. 1, No. 6, Nov. 2017.

[12] S. D. Jang, et al., "Frequency selective surface based passive wireless sensor for structural health monitoring," *Smart Materials and Structures*, Vol. 22, No. 2, 025002, 2012.

[13] S. H. Lee, and Ic-Pyo Hong, "Design of Frequency Selective Paper for Crack Detection of Concrete Building Structure," *2018 IEEE International Symposium on Antennas and Propagation & USNC/URSI National Radio Science Meeting*. IEEE, pp. 2019-2020, 2018.

[14] E. Kinzel, "Design of a Frequency-Selective Surface Strain Sensor," *2014 IEEE International Symposium on Antennas and Propagation & USNC/URSI National Radio Science Meeting*. IEEE, pp. 2074-2075, 2014.

[15] D. Pieper, et al., "Embedded FSS Sensing for Structural Health Monitoring of Bridge Columns," *Instrumentation and Measurement Technology Conference Proceedings (I2MTC), 2016 IEEE International*. IEEE, 2016.

[16] Mahboobeh Mahmoodi, and Kristen M. Donnell, "Active frequency selective surface for strain sensing," *2017 IEEE International Symposium on Antennas and Propagation & USNC/URSI National Radio Science Meeting*. IEEE, 2017.

[17] M. Mahmoodi, and K. M. Donnell, "Novel FSS-Based Sensor for Concurrent Temperature and Strain Sensing," *IEEE, Antennas and Propagation Society International Symposium (APSURSI)*, 2017.

[18] D. F. Pieper, and K. M. Donnell, "Application of Frequency Selective Surfaces for Inspection of Layered Structures," *Instrumentation and Measurement Technology Conference Proceedings (I2MTC)*, *2015 IEEE International*. IEEE, 2015.

[19] W. Zhang, et al., "High Sensitivity Refractive Index Sensor Based on Frequency Selective Surfaces Absorber," *IEEE Sensors Letters*, Vol. 2, No. 3, pp. 1-4, 2018.

[20] Girard, Martin, and Maksim Skorobogatiy., "Integrated terahertz multiparameter sensors using fiber/frequency selective surface couplers," *Journal of Optics* Vol. 16, No. 9, 094007, 2014.

[21] C. Debus, and Peter Haring Bolivar., "Frequency selective surfaces for high sensitivity terahertz sensing," *Applied Physics Letters*, Vol. 91, No. 18, 184102, 2007.

[22] R. Melik, et al., "Metamaterial Based Telemetric Strain Sensing in Different Materials," *Optics express* 18.5, pp. 5000-5007, 2010.

[23] E. Ekmekci, et al., "Multi-functional metamaterial sensor based on a broad-side coupled SRR topology with a multi-layer substrate," *Applied Physics A,* Vol. 110. No. 1, pp. 189-197, 2013.

[24] J. Li, et al., "Flexible Terahertz Metamaterials for Dual-Axis Strain Sensing," *Optics letters*, Vol. 38, No. 12, pp. 2104-2106, 2013.

[25] M. I. R. Shishir, et al., "Frequency-selective surface-based chipless passive RFID sensor for detecting damage location," *Structural Control and Health Monitoring,* Vol. 24, No. 12, e2028, 2017.

[26] Kalyan K. Karnati, et al., "Q-Factor Analysis of Reflectarray Elements Investigating the Effects From Angle of Incidence Using Floquet Modes," *IEEE Transactions on Antennas and Propagation*, Vol. 62, No. 10, pp. 5017-5028, 2014.

[27] Mahboobeh Mahmoodi, and Kristen M. Donnell, "Effect of illumination pattern on FSS-based sensor resolution," *2018 IEEE International Instrumentation and Measurement Technology Conference (I2MTC)*. IEEE, 2018.

[28] J. Huang, "Analysis of a microstrip reflectarray antenna for microspacecraft applications," 1995.

[29] Mahboobeh Mahmoodi, Mohammad Tayeb Ghasr, and Kristen M. Donnell, "Synthetic beamforming for localized FSS-based sensing," *2018 IEEE International Instrumentation and Measurement Technology Conference (I2MTC)*. IEEE, 2018.

[30] Mahboobeh Mahmoodi, and Kristen M. Donnell, "Improvement in FSS-Based Sensor Sensitivity by Miniaturization Technique," *2019 IEEE International Symposium on Antennas and Propagation and USNC-URSI Radio Science Meeting*. IEEE, 2019.

VITA

Mahboobeh Mahmoodi was born in Tehran, Iran. Mahboobeh received her B.Sc. (2010) and M.Sc. (2014) degrees in Electrical Engineering from Shahed University and Khaje Nasir Toosi University of Technology, Tehran, Iran, respectively. She joined the Applied Microwave Nondestructive Testing Laboratory (*amntl*) at the Missouri University of Science and Technology (S&T), Rolla, MO, in Fall 2015 to purse her Ph.D. degree. She worked as a graduate research assistant from Fall 2015 to Summer 2019. She then continued with Microwave Sensing (*μSense*) for Fall 2019. She received her Doctor of Philosophy in Electrical Engineering from Missouri S&T in May 2020. Her research intrests included antennas, microwave & mm-wave, electromagnetic filters & sensors, frequency selective surfaces, reflectarray antennas, phased array antennas, beamforming, and singnal & power integrity. She was an intern student at Cisco System, San Jose, CA, in Summer and Fall 2018. Mahboobeh was also awarded four student travel grants from the American Nondestructive Testing Society from 2016 to 2019, and one from the Office of Graduate Studies of Missouri S&T in 2018. She was a member of the IEEE Antennas and Propagation Society, IEEE Sensors Council, IEEE Young Professionals and American Society for Nondestructive Testing.